Ambient noise tomography at the Oseberg oil and gas field, North sea

Charlotte Bruland

Master's thesis in Geosciences
Geophysics
60 credits

Department of Geoscience
Faculty of mathematics and natural sciences

UNIVERSITY OF OSLO

Spring 2018

Ambient noise tomography at the Oseberg oil and gas field, North sea

Charlotte Bruland

Ambient noise tomography at the Oseberg oil and gas field, North sea

http://www.duo.uio.no/

Printed: Reprosentralen, University of Oslo

Abstract

Recent studies show that the noise recorded by seismic sensors can be used to characterize the seismic structure in the area where the sensors are located. This is called ambient noise tomography. In this thesis, data from ocean bottom cables at the Oseberg oil and gas field was used to characterize the near-surface in an area used for waste disposal. 32 days of data was made available to us from Equinor (Statoil). By using interferometry, we created virtual sources by taking the cross-correlation between ambient noise recordings made at different stations. Through slowness-frequency analysis, the dispersion curves of surface waves were retrieved from the noise correlations, and inverted to explore the shear wave velocity with depth. The platform is a major source of noise in the area. Below 2 Hz, we have noise coming from all directions. Above 2 Hz, the main source is the platform. Since the array of stations is made mostly of 4 lines in line with the platform, both the noise coming from all directions and the noise coming from the platform was used. The ambient noise with frequencies up to 4 Hz was used for Green's function retrieval, and we see that eight hours of data is sufficient for retrieving the Green's functions. No major change with time was observed, and the Green's functions along the 4 lines are very similar. The Love wave and the Scholte wave fundamental mode and overtone emerged from the cross-correlations of ambient noise. The Scholte wave fundamental mode was used for inversion, and a model of S-wave velocity with depth down to 3000 m was obtained. The velocity increases from 300 m/s at the sea bottom to about 1700 m/s at 3 km depth, similar to the results retrieved from other methods.

Acknowledgement

First, I would like to thank my supervisors, Valerie Maupin and Volker Oye, for inspiration and guidance. I want to thank Sascha Bussat for contributing with his expertise, and Equinor (Statoil) for giving me access to such an interesting dataset. To my family and friends, thank you for the motivation and support.

Contents

List of Tables

List of Figures

Chapter 1

Introduction

1.1 An introduction to ambient noise surface wave tomography

Surface wave tomography is a technique to study the Earth's superficial layers. Since surface waves are dispersive and sensitive to the shear wave velocity, they allow us to explore the shear wave velocity structure. Dispersion means that different frequencies of the wave travel at different velocities. Since different frequencies are sensitive to different depths, with lower frequencies being sensitive at greater depths, the dispersion curves of surface waves can be inverted to velocities at depth. Through a relation between surface wave velocity and shear wave velocity, the shear wave velocity can be estimated for different depths.

Traditionally, surface wave tomography is based on records from earthquakes. This results in two main shortcomings. Firstly most techniques are based on waves from earthquakes occurring only in geologically active areas, as plate boundaries, which results in limited resolution in all other areas where earthquakes are not present. When you have a station that is far away from the source, all high frequency signals are lost due to attenuation. The earthquakes' occurrence is also too low, which makes it difficult to study potential changes of active structures with time, for example at a volcano or at an injection site. For active seismic at smaller scales, the resolution is limited by the number and power of sources. It is therefore difficult to image large areas or deep structures. Controlled source seismic is difficult to carry out when the area is hard to access. For example at the ocean bottom, where passive seismic could be more convenient. When monitoring changes over time, we need reproducible sources, which is difficult to achieve over long time durations (Gouedard et al., 2008). Controlled sources are also expensive.

There is, however, an alternate way of probing the Earth by using noise records only. Noise is available everywhere, and it is also free. The use of ambient noise correlations to reconstruct the Green's functions between pairs of stations was a major development in surface wave tomography, and was shown by Lobkis and Weaver (2001) in the field of ultrasonics. Historically, ambient noise cross-correlations were first used in helioseismology

where cross-correlations were performed on recordings of the Sun's surface random motion to retrieve time-distance information on the solar surface (Duvall Jr et al., 1993). In seismology, Aki (1957) proposed that seismic noise could be used to retrieve the dispersion properties of surface waves in the subsoil, and Shapiro and Campillo (2004) reconstructed the surface wave part of the Green's function and measured dispersion curves. The dispersion curves for the surface waves extracted from noise correlations are similar to those of earthquakes. Consequently, one can use the same methods as for conventional surface wave tomography on ambient noise measurements. The method is called ambient noise tomography and has resulted in an explosion of new results on different scales.

The technique has been used widely for continental- or regional-scale studies of the crust and uppermost mantle, by Lin et al. (2007), Moschetti et al. (2007), Stehly et al. (2009) and more, and has also been applied on a small scale to volcanic edifices by Brenguier et al. (2007). Due to the limited availability of seismic networks on the ocean bottom, there are fewer studies from the oceanic environment. There are, however, studies from industrial seismic networks with a large number of stations. Mordret et al. (2013) and Bussat and Kugler (2011) showed the feasibility of offshore application on a reservoir scale, and that short recording duration of only a few hours can provide excellent Green's functions.

In this thesis ambient noise tomography will be used to characterize the near-surface at the Oseberg oil and gas field.

1.2 The Oseberg field and ocean bottom cables

The noise recordings used in this thesis are recorded by seismic sensors placed on the seafloor above the Oseberg oil and gas field, which is located in the North Sea. This part of the field is used for waste disposal, and the receivers are a part of a caprock monitoring system placed there to monitor the injection of waste. The layout of the array is illustrated in Figure 1.1. The system has a 'V'-shaped layout consisting of 172 sensors. Each sensor holds a hydrophone and three orthogonal geophones. This particular configuration was chosen so that the main lines of the array point towards the platform. In this way the noise coming from the platform is seen as linear events on the data, and is therefore more easily removed. Between the sensors on the outer leg, the distance is 50 m, while the distance on the inner legs is 25 m. The water depth is 108 m, while the cable is trenched 1-2 m into the seabed (Bussat et al., 2016). 32 days of data, from January and February 2014, was available to me from Equinor (Statoil) through Sascha Bussat. Data from selected stations was used, and recordings from the vertical, transversal, radial and hydrophone component were analyzed.

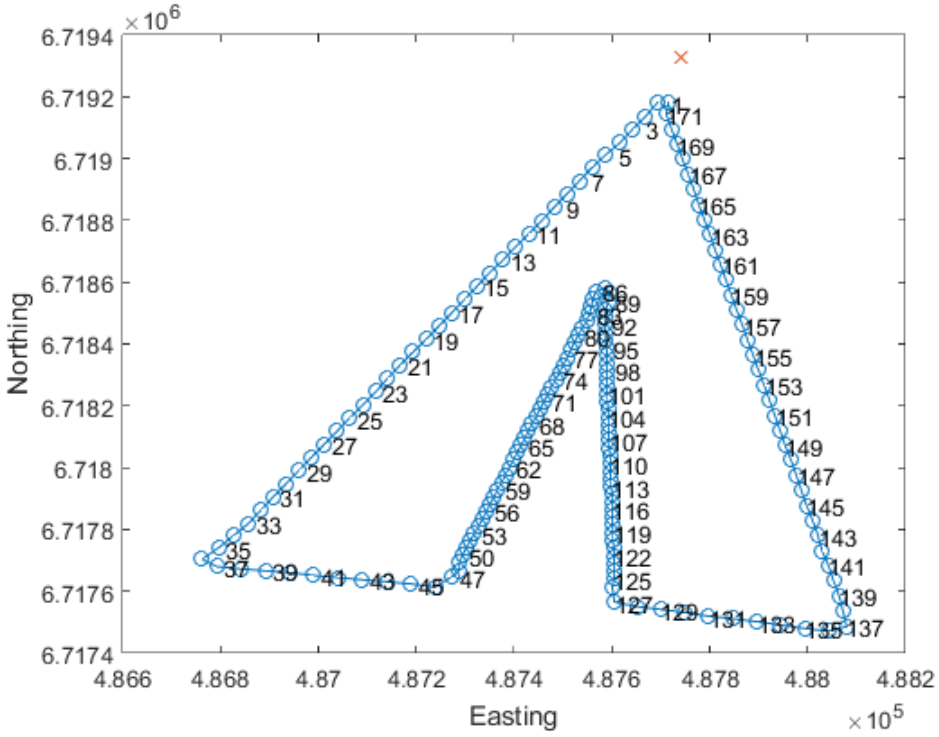

Figure 1.1: *Overview of system layout with receivers marked with circles and the platform with a red cross. Sensor spacing is 50 m on the outer legs and 25 m on the inner legs. The cable is trenched 1-2 m into the seabed at a water depth of 108 m.*

1.3 Objectives and motivation

Due to expensive onshore disposal and limited storage capacity offshore, most oil and gas fields have an injection well for disposal of slop and cuttings. Having access to a disposal well saves about $10 million per year for a single drilling rig, but several offshore hydrocarbon-bearing fields have experienced fractures in the overburden as a consequence of injection, which can result in leakage of waste to the surface. Therefore the Oseberg C caprock monitoring system was installed in 2013. The system aims for safer operation with avoidance of leakage to the sea and increased injection, and can record continuously. (Bussat et al., 2016)

This thesis aims to use ambient noise recorded by the Oseberg monitoring system to characterize the near surface, which could be used to look for changes in the overburden that could lead to leakage of waste. The motivation behind the thesis is to identify methods and systems to help shutting down the injection or to observe changes quickly, and hence stop injection.

1.4 Outline

The thesis is divided into three main parts which correspond to the three main data processing steps: interferometry, slowness-frequency analysis and inversion. Each part includes an introduction to the topic, methods, results, discussion and concluding remarks. In the interferometry chapter, virtual sources are created by taking the cross-correlation between ambient noise recordings made at two stations, while the slowness-frequency chapter focuses on retrieving and studying dispersion curves from the cross-correlations. The inversion uses the dispersion curves retrieved from the slowness-frequency analysis to explore the S-wave velocity with depth. Lastly a summary of key findings and conclusions is presented.

Chapter 2

Interferometry

Interferometry is taking the cross-correlation between recordings made at two stations to get information about what is between them. The most common form of interferometry is based on the assumption that noise is coming from all directions. When taking the cross-correlation between two stations with noise coming from all directions, we get the energy that is coherent between them. This energy corresponds to the energy that travels from one station and gets picked up at the other station. Effectively, this turns one of the stations into a virtual source (EAGE Channel, 2015). This is illustrated in Figure 2.1.

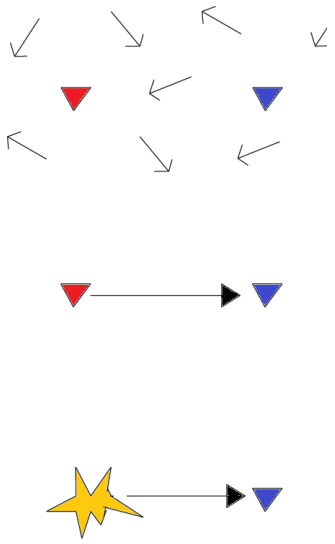

Figure 2.1: *Two stations with noise coming from all directions. When you take the cross-correlation between these two stations, you get the energy that travels from one station to the other station, turning one of the stations into a virtual source.*

The Green's function of a medium between two stations represents the record we would obtain at one station if an impulsive source is applied at the other. Therefore interferometry is also called Green's function retrieval. The resulting time lag of the cross-correlation corresponds to the time it takes for the wave to travel from the virtual source to the receiver.

Since seismic noise is mainly generated by atmospheric and oceanic forces at the Earth's surface, mainly surface waves emerge from the cross-correlations. This noise has low frequencies and can be applied to a large scale. It also comes from all directions. When noise is coming from all directions, the cross-correlation is symmetric around zero time lag. At smaller scales, the same principle can be applied to study local structures. In this case we use higher frequencies. The wavefield of the higher frequencies is assumed to be dominated by local sources, and is therefore unlikely to display the same symmetry as at the lower frequencies (Gouedard et al., 2008).

2.1 Ambient noise method

The theory of the ambient noise method is based on the superposition of plane waves coming from all directions. It assumes that the noise field consist of 2D uncorrelated surface waves that come from large distances. Let us look at the geometry of two stations with energy coming from a distant source, which is presented in Figure 2.2.

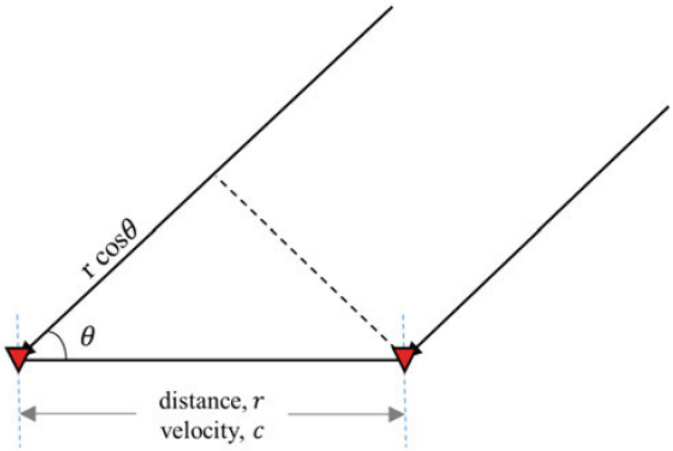

Figure 2.2: *Geometry for two stations and an incoming plane wave at an angle of θ from the interstation axis. The distance between the receivers is r, while the velocity is c. The difference between the path from the source to the different stations is $r\cos\theta$. (Sadeghisorkhani, 2017)*

Figure 2.2 displays two receivers with an incoming plane wave at an angle of θ. The distance between the receivers is denoted r, and the velocity c. The velocity is assumed constant. The difference between the paths from the source to the two stations is given by $r\cos\theta$. Hence, the difference in traveltime to the two stations is $\Delta t = r\cos\theta/c$.

If we have noise coming from multiple directions and assume that there is no correlation between the noise sources, the cross-correlation of the signals recorded at the two

stations is the sum of the cross-correlation function for each relevant direction. In the frequency domain the cross-correlation is given by integrating all plane waves over the angle 0 to 2π.

$$C(\omega) = \int_0^{2\pi} \exp\,(i\frac{\omega r}{c}\cos\theta)d\theta \tag{2.1.1}$$

where ω is the angular frequency. In the time domain the cross-correlation can be calculated by taking the inverse Fourier transform of equation 2.1.1, which gives

$$C(t) = \frac{1}{2\pi}\int_{-\infty}^{\infty}\int_0^{2\pi} \exp\,(-i\frac{\omega r}{c}\cos\theta)\exp\,(i\omega t)d\theta d\omega \tag{2.1.2}$$

The equation can be used to generate synthetic cross-correlations in the presence of uniformly distributed noise sources. Figure 2.3 is an example of this from Sadeghisorkhani (2017) where the cross-correlation is constructed from adding 360 plane waves coming from all angles.

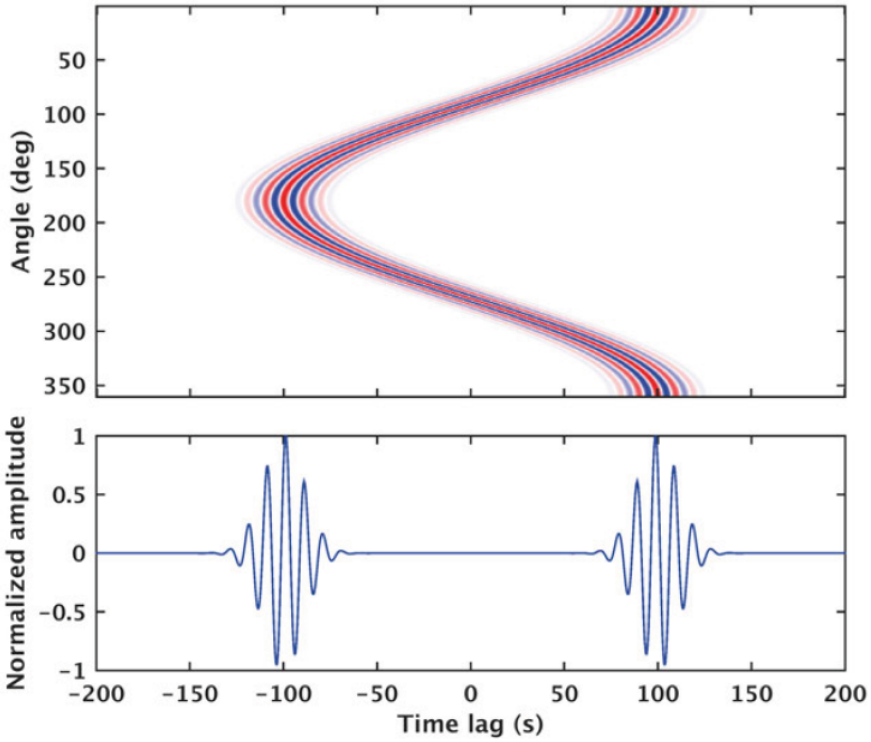

Figure 2.3: *Cross-correlation construction of adding 360 plane waves coming from all angles. At the top we have the individual cross-correlations at a given angle versus time lag. Each horizontal line represents the individual cross-correlation function for a localized source at the corresponding angle. Positive values are in red, negative in blue and small values are in white. The lower part is the summation of all the cross-correlations above. (Sadeghisorkhani, 2017)*

The top of Figure 2.3 shows the individual cross-correlations for a given angle in degrees on the y-axis versus the time lag in seconds on the x-axis. Each horizontal line represents the individual cross-correlation function for a localized source at the corresponding angle. Red represents positive values, blue negative values, while the small values are in white. By adding all the cross-correlations from the upper part of the figure you get the lower part of the Figure 2.3. The lower part shows the interference, with normalized amplitude on the y-axis and the time lag in seconds is on the x-axis.

By comparing the results we get for interferometry to the result we would get for a direct plane wave, we see that the result you get from interferometry is the same as an incoming direct plane wave at an angle of 0 degrees with an interstation travel time that corresponds to the velocity between the stations, but with a phase shift of $\frac{\pi}{4}$. The difference in phase arises because of the interference of waves from all directions, and is shown in Figure 2.4.

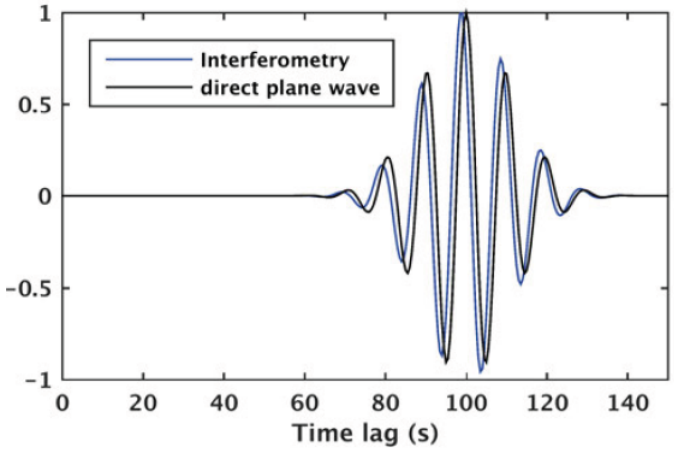

Figure 2.4: *Phase shift of the direct plane wave travelling along the interstation axis and the cross-correlation from interferometry. (Sadeghisorkhani, 2017)*

Figure 2.4 displays the causal part of the constructed cross-correlation from noise coming from all angles in blue, and the corresponding direct plane wave that travels along the interstation axis. There is a clear difference in phase on the figure, and it must be accounted for when measuring phase velocities. (Sadeghisorkhani, 2017).

If we have an uneven source distribution, it will affect the symmetry of the cross-correlations. This is shown in Figure 2.5. The parameters are the same as for Figure 2.3, but an energy anomaly centered at 15 degrees compared to the interstation axis is included. (Sadeghisorkhani, 2017)

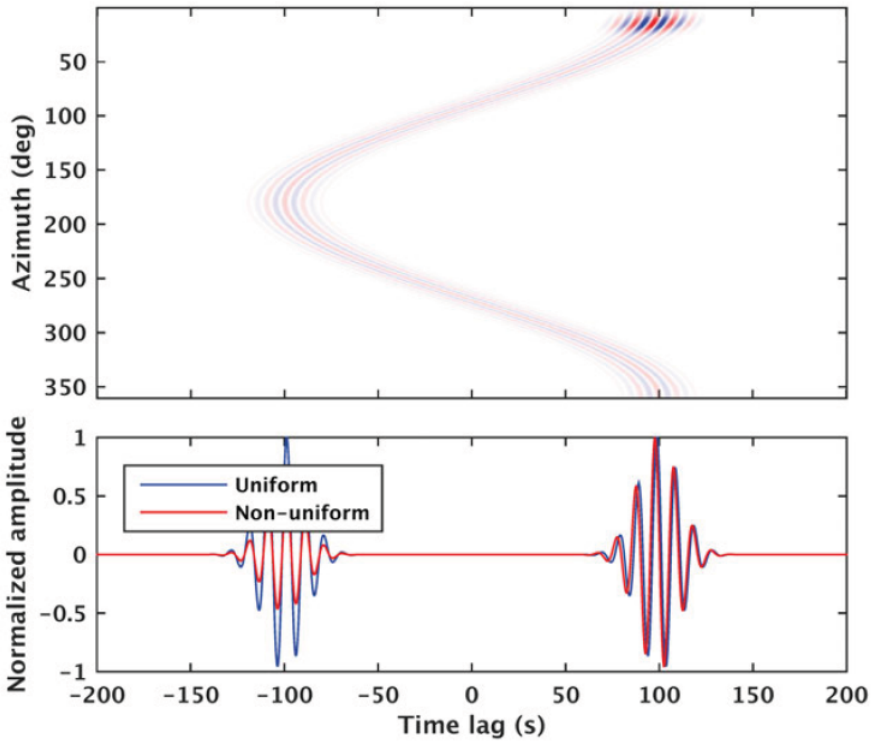

Figure 2.5: *Non-uniform noise distribution on the constructed correlation. (Sadeghisorkhani, 2017)*

If we know where the noise is coming from, interferometry can also be used for noise coming from one direction if the source is aligned with the direction of the station pair or array.

2.2 Noise correlations from the Oseberg field

Raw data

In this work 32 days of noise records from 152 4C seismic sensors, sampled at 0.002 seconds, was analyzed. One hour of noise records, recorded by the vertical component, from station 1 to 25 is presented in Figure 2.6.

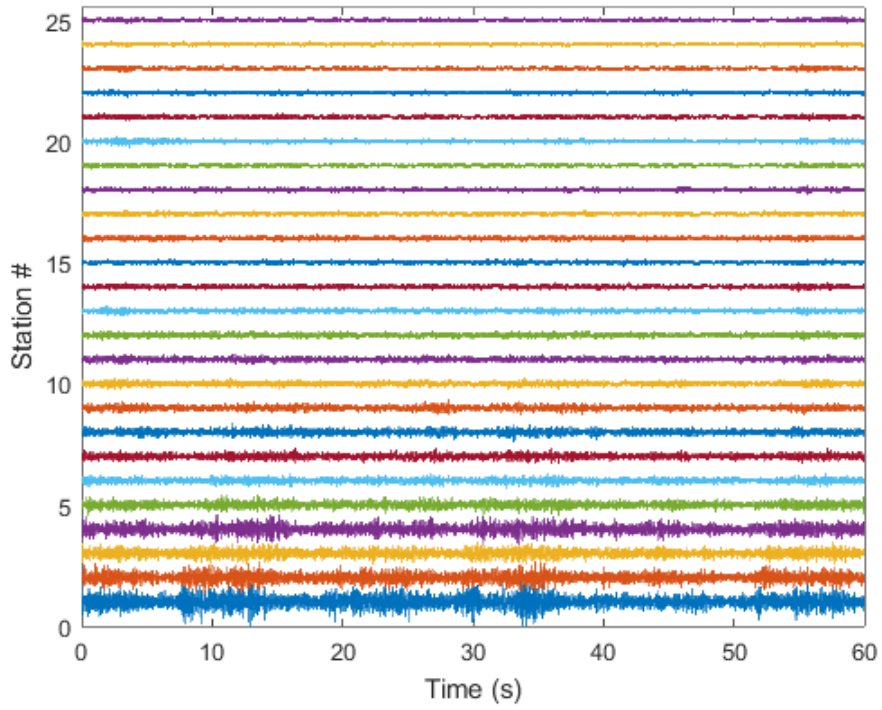

Figure 2.6: *One hour of noise records from station 1-25, from the vertical component. The distance from the platform increases with the station number, and the amplitude decreases as the distance from the platform increases from June 4th, 12 pm.*

Figure 2.6 shows the noise traces recorded at different stations with the station number on the y-axis and the time in seconds on the x-axis. The records are from June 4th, 12 pm. We see an increase in amplitude as one approaches the platform. If all 172 stations were plotted, the amplitudes would decrease, then increase, decrease and lastly increase again due to the layout of the monitoring system (Figure 1.1). This shows that the platform is a major source of noise. The stations closest to the platform were discarded to avoid complications due to the proximity of the platform. We also looked at the frequency content, which is displayed in Figure 2.7.

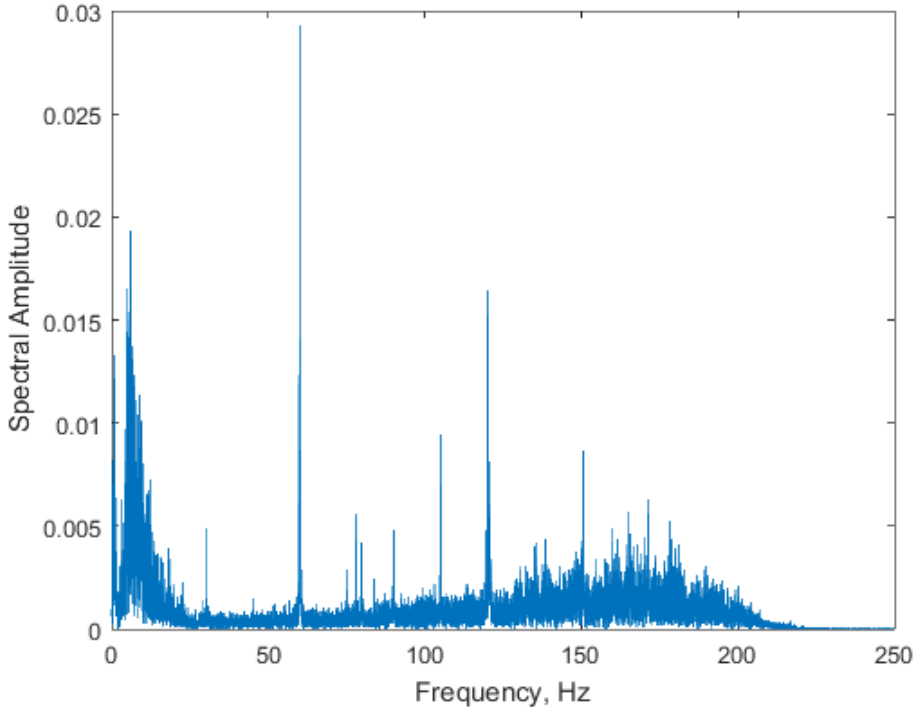

Figure 2.7: *Amplitude spectrum showing the frequency content for a one-hour trace from station 10 June 4th, 12 pm. There is a minimum at around 30 Hz. Below this frequency there are two pronounced spikes.*

Figure 2.7 shows the amplitude spectrum of a one-hour long trace from the same time as the time signal in Figure 2.6 for station 10. The amplitude spectrum (Figure 2.7) displays the frequency content, with frequency on the x-axis and the amplitude on the y-axis. There are two different maxima below 30 Hz, and something different above 30 Hz. At around 30 Hz we have a minimum. It was therefore decided to focus on the frequencies below 30 Hz, which have sufficient penetration depth.

Computing cross-correlations and configurations

The cross-correlations were computed by using the function xcorr in Matlab. The same components on each station were correlated with each other (ZZ, TT, RR, HH). Cross-correlations were carried out along the lines presented in Figure 2.8 and for interstation pairs across the system in Figure 2.9.

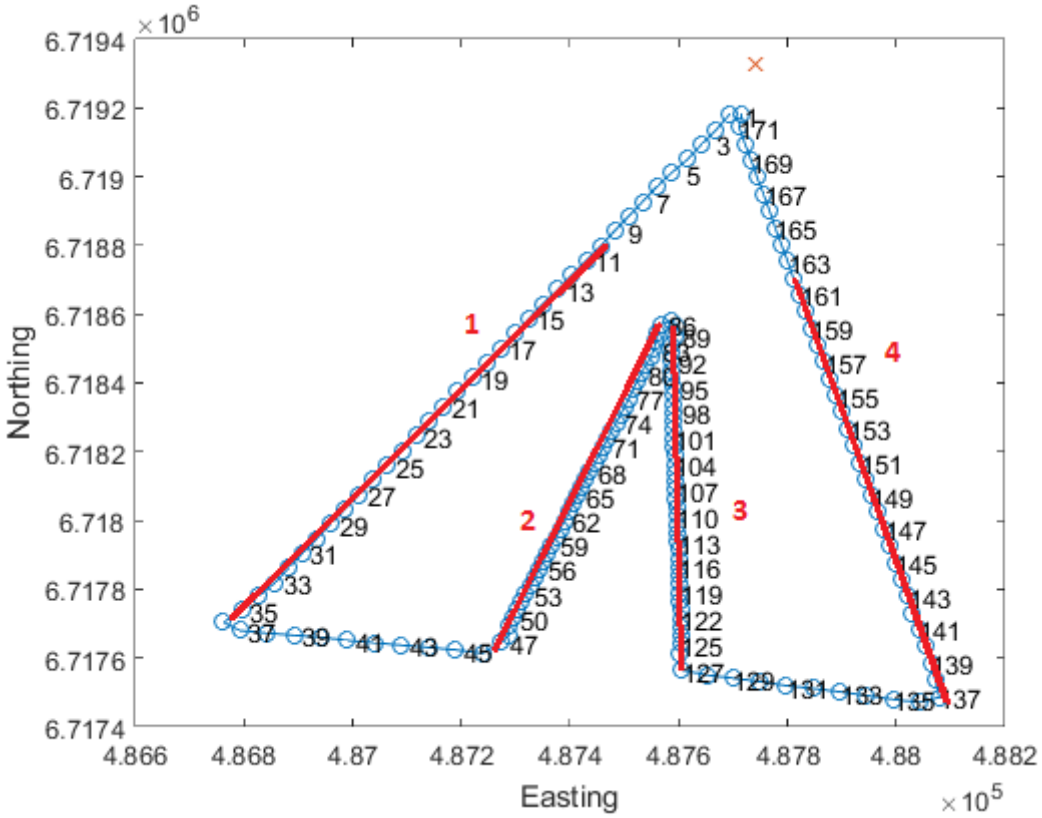

Figure 2.8: *Overview of stations used for cross-correlations for the lines pointing towards the platform. The location of the platform is marked with a red cross top right. Stations on the outer left leg are correlated with station 10, the stations on the inner left leg with station 86, stations on the inner right leg with station 88 and the stations on the outer left leg are correlated with station 162.*

Figure 2.8 shows an overview of stations used for cross correlations along the four lines of the array pointing towards the platform. Cross-correlations were performed between a fixed station and different stations along the same line, on all legs of the system. This produced different numbers of cross-correlations along each line with increasing offset. From the longer lines we got 25 correlations, and 39 correlations from the shorter lines. The last configuration used for cross-correlations is displayed in Figure 2.9.

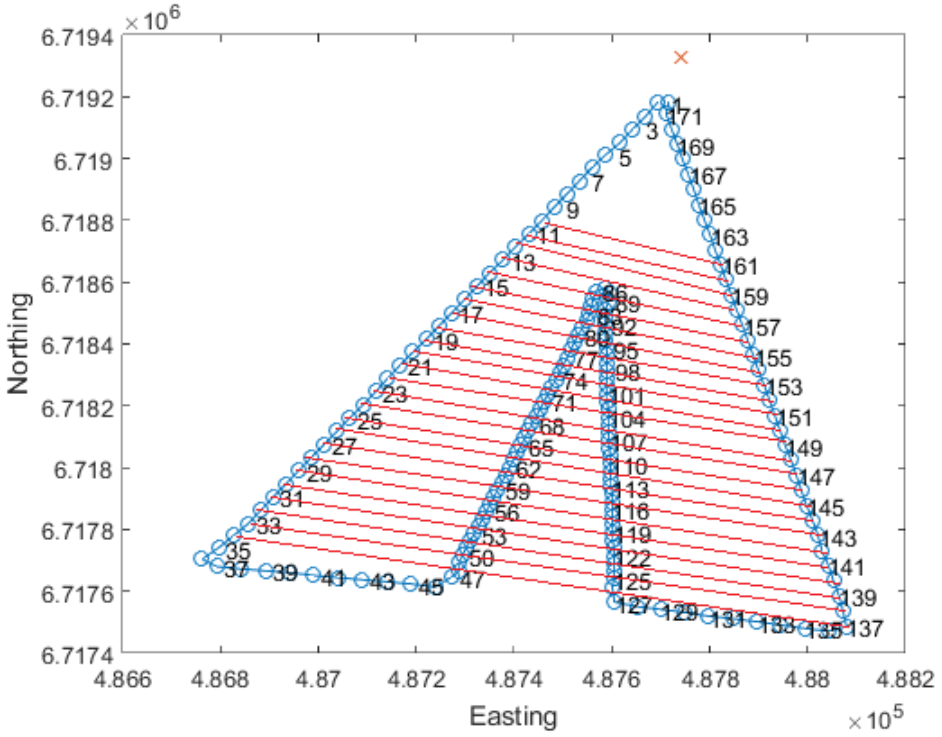

Figure 2.9: *Overview of stations used for cross-correlations across the system. The location of the platform is marked with a red cross. Stations on the outer left leg correlated with stations on the outer right leg.*

Figure 2.9 shows the configuration for the station pairs used for cross-correlations with pairs that are not in line with the platform. Stations on the left outer leg were correlated with stations on the right outer leg, for example station 11 was cross correlated with station 161, station 12 with station 160 and so on. We will call these interstation correlations across the system later in the thesis. To retrieve the Green's functions from the noise traces, some processing was needed.

2.3 Processing

All processing was done by myself in Matlab. Firstly, the data was organized into five-minute long segments. The pre-processing was done station by station and segment by segment, and included (1) removal of the mean and trend of the signal, (2) spectral whitening between -30 to 30 Hz and (3) 2 Hz/4 Hz/10 Hz/30 Hz low pass filter. Then the (4) cross-correlations were carried out, and the correlations were (5) normalized and (6) stacked.

To find out which order would work best in these specific cases, the performance of different processing schemes was tested before deciding upon the work flow presented. The steps, explaining why and when to carry them out, with examples are presented in

this section. For the testing one hour of data from the vertical component was used and a 30 Hz low-pass filter, unless stated otherwise. Testing was done for the correlations along line one in Figure 2.8 and for the interstations across the system in Figure 2.9.

Detrend
Detrending is usually the first thing to do when processing data, and was therefore applied first. It includes subtracting the mean and removing the linear trend from the data, and was done in Matlab by making use of the already existing detrend function. The function computes the least-squares fit to the data and subtracts the resulting function. Using detrend on the traces rather than the cross-correlations made very little difference on the results. Therefore it did not matter whether it was done before or after the cross-correlation.

Spectral whitening
Then the cross-correlations were whitened to get a better representation of all frequencies present. When whitening one wants to even out the amplitude spectrum and get all values close to or equal to 1. This was done by multiplying the amplitude spectrum of the cross-correlation, S(ω), with the amplitude spectrum of a filter F(ω) and setting the output equal to 1. Hence, the solution of the filter was found by:

$$|F(\omega)||S(\omega)| = 1 \rightarrow |F(\omega)| = 1/|S(\omega)| \tag{2.3.1}$$

When S(ω) approached zero, F(ω) got very large. To avoid putting too much emphasis on the frequencies with low frequency content, a water level(λ) was included in the filter. It was set equal to 0.1 percent of the absolute value of the maximum value of the cross-correlation. The new filter is given by:

$$|F(\omega)| = 1/(\lambda + |S(\omega)|) \tag{2.3.2}$$

In this way multiplying the amplitude spectrum of the cross-correlation with the amplitude spectrum of the filter reduces the differences in amplitude, while not spiking certain frequencies. The effect of the water level is illustrated in Figure 2.10

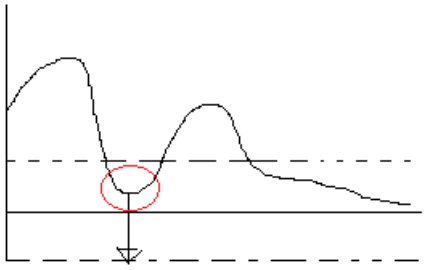

Figure 2.10: *Illustration of the effect of the water level. If the amplitude is smaller than the water level, the point will be forced down instead of amplified.*

By definition the whitening filter is working on the entire spectrum. To avoid putting too much work into the parts of the spectrum that will be removed by the low-pass filter, the whitening filter was modified so that it only worked in the frequency interval of interest. This was done by setting the values of the filter outside of the interval -30 to 30 Hz equal to 1. Spectral whitening only operates on the amplitude spectrum, and therefore the phase spectrum is unaffected. (Lee, 1986)

The effects of spectral whitening on cross-correlations
To see the effects of the spectral whitening, we began by performing the steps presented in the beginning of this section without a whitening filter, as a starting point. Firstly detrend and low-pass filtering was done on the traces, before carrying out the cross-correlations. After carrying out the cross-correlation, the correlations were stacked and normalized. The resulting cross-correlations for the interstations across the system are displayed in Figure 2.11.

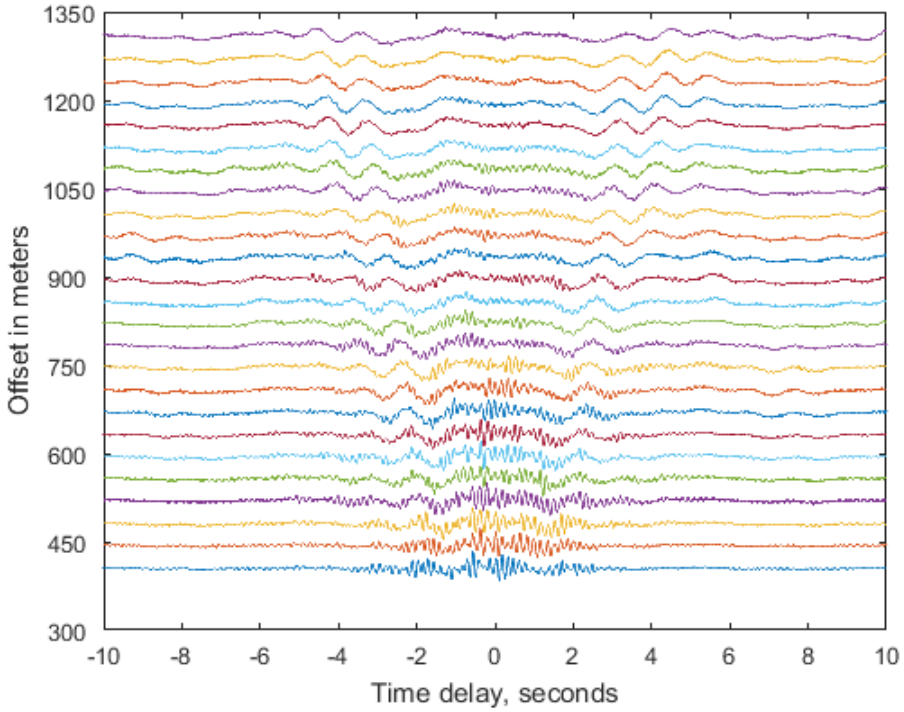

Figure 2.11: *Stacked cross-correlations across the system without spectral whitening. Detrend and filtering was done before the cross-correlations. The correlations were normalized. The figure displays symmetry, and there is a difference in phase and group velocity.*

Figure 2.11 shows the cross-correlations without spectral whitening from the interstations across the system. The correlations are plotted with increasing offset in meters on the y-axis and time delay in seconds on the x-axis. The figure displays a 'V'-shaped signal symmetric around zero, which can be used to calculate velocities. A difference in phase

velocity from group velocity was observed, so the wave is dispersive. It also appeared to be something going on in the center of the plot, which could be noise from the platform as the location of the platform not in line with the station pairs, but almost perpendicular, and the energy coming from the platform will therefore arrive at small time lags. The same results from line one are presented in Figure 2.12.

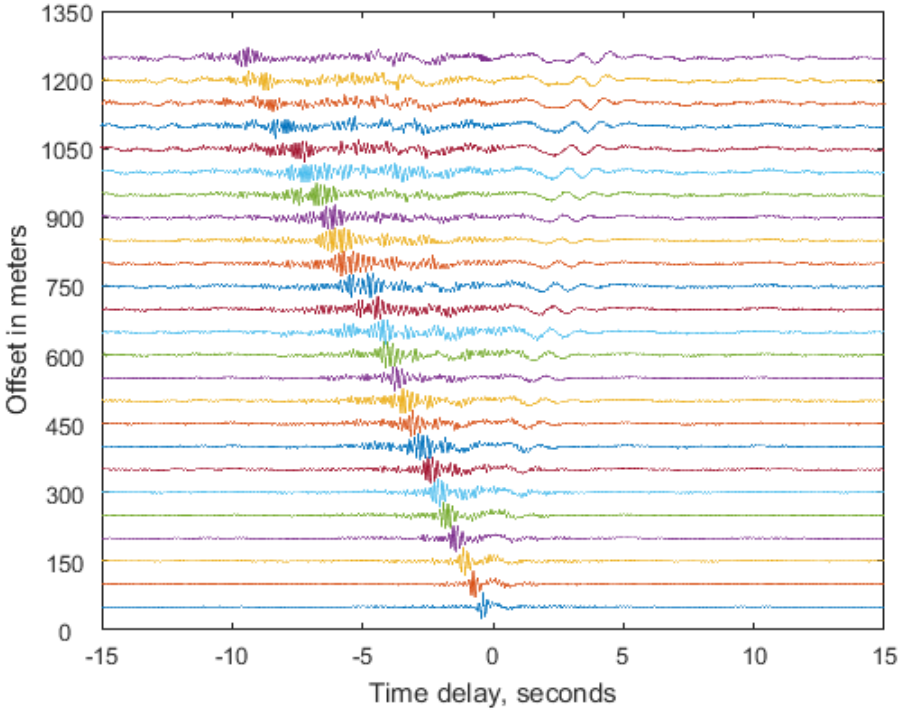

Figure 2.12: *Same as Figure 2.11 for line one. There is one noticeable wave for negative time lag, which is not symmetric. Another wave is observable for positive time lag, and is slightly visible for negative time lag.*

The cross-correlations from line one without spectral whitening are shown in Figure 2.12. For line one the correlations resulted in one very noticeable wave for negative time lag, and another prominent wave for positive time lag, but with different velocities. A difference in group and phase velocity is observed. It is also slightly visible for negative time lags. There appears to be something going on close to zero time lag. Both could be enhanced by whitening.

Moving on to the spectral whitening, the objective was to enhance and separate the different features. Detrend, spectral whitening and low-pass filtering was performed prior to the cross-correlations, then the correlations were stacked and normalized to the same amplitude for all station pairs. The results from the pairs across the system are shown in Figures 2.13 to 2.15.

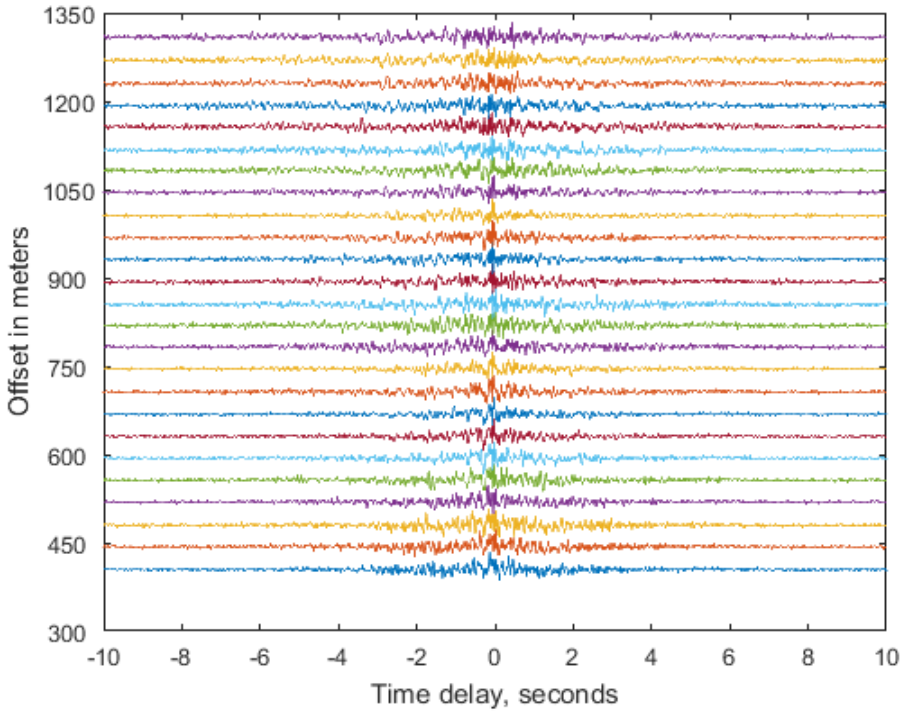

Figure 2.13: *Cross-correlations across the system with spectral whitening. Detrend, spectral whitening and filtering was done before the cross-correlation. The correlation was normalized.*

Figure 2.13 shows the cross-correlations from the interstations across the system with spectral whitening. The figure shows one prominent feature at about 0 s time lag. There appears to be something going on between -2 s and 2 s as well. The symmetric 'V'-shape for the long period signals is lost. To study what was going on in the center of the plot, we decided to look at smaller time lags, which is presented in Figure 2.14 and 2.15.

Figure 2.14 is the same as Figure 2.13, but for time lag between -2 s and 2 s. When looking at smaller time lags, three very steep features are revealed. Two of the features appear to be relatively symmetric, and are found at +-0.5 s. The last feature is very close to zero time lag. To see if this feature is symmetric, we look at even smaller time lags, which is shown in Figure 2.15.

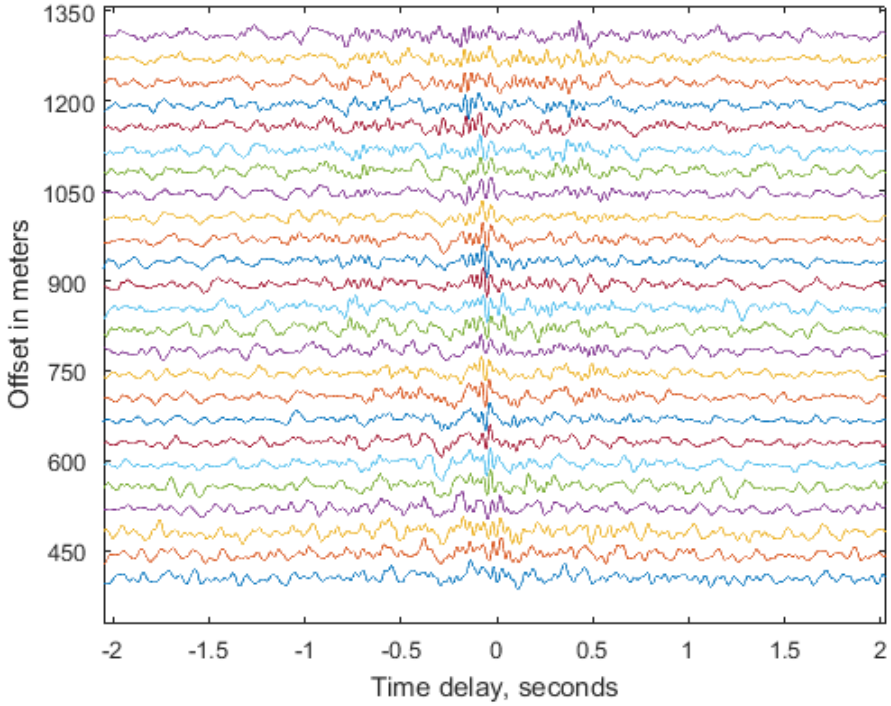

Figure 2.14: *Zoom of Figure 2.13 for [-2,2]s interval. Three steep features are observed.*

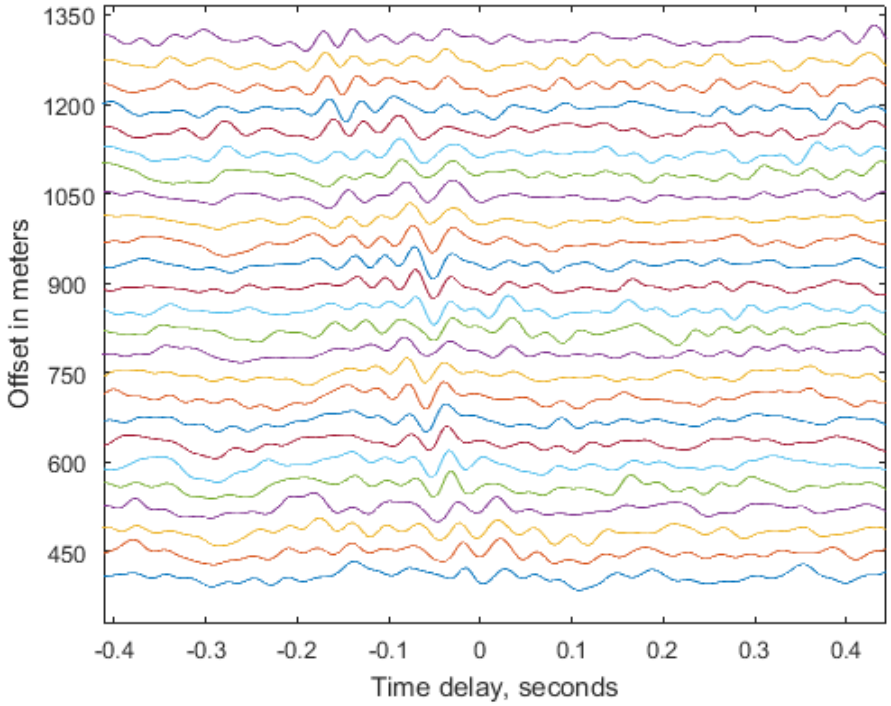

Figure 2.15: *Zoom of Figure 2.13 for [-0.4,0.4]s interval. The signal is not symmetric.*

Figure 2.15 is also the same as Figure 2.13, but for time lags between -0.4 and 0.4. The figure reveals that the feature in the center of the plot is not symmetric around zero time lag, but is only present for negative time lag. This could be noise from the platform. As the platform is not in line with the station pair direction, but almost perpendicular and the distance between each station and the platform is different, the correlation will come at small times, with apparent velocity close to infinite. In this case the noise sources are not homogeneously distributed or in line with the stations, which is a condition for interferometry, and can therefore not be used to find velocities. The results from line one with spectral whitening are presented in Figure 2.16.

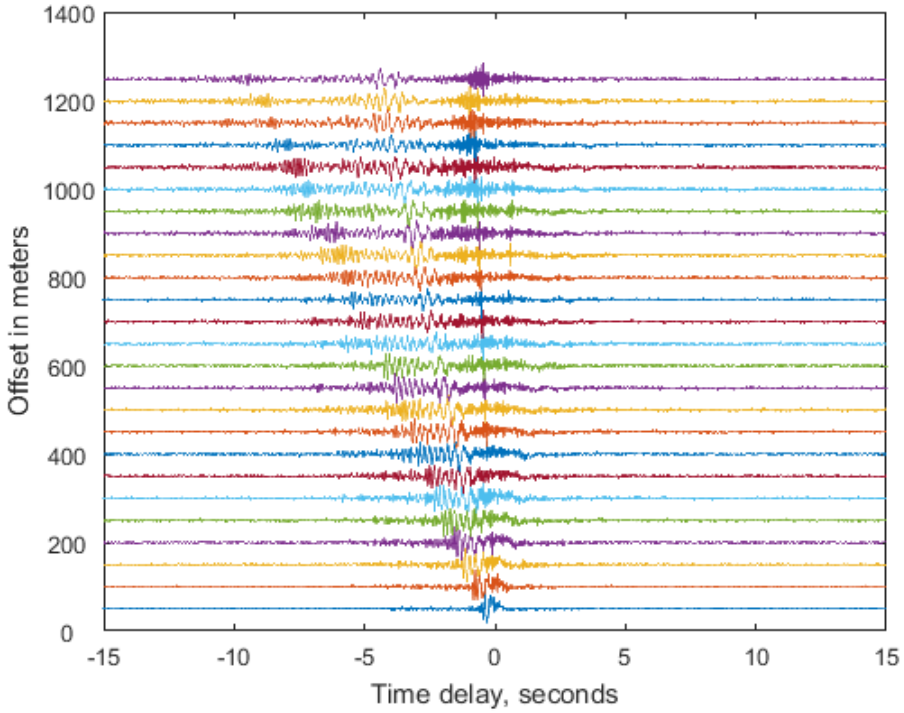

Figure 2.16: *Same as Figure 2.13 for line one. Three waves are revealed by spectral whitening.*

On the cross-correlations along line one moving away from the platform (Figure 2.16), the spectral whitening revealed three different waves with different velocities. Since line one is inline with the platform we can calculate velocities from the correlations. Closest to the middle we find the fastest wave, which was highlighted by the spectral whitening. The wave is symmetric around zero time lag, and the signal is stronger on the same side as the platform. The next feature has slightly slower velocities and is stronger for negative time lag. The last feature is also only visible for negative lag times and has very low velocity. The asymmetry could be due to an uneven distribution of noise sources, with a lot of noise coming from the platform. Comparing the results with spectral whitening to the results without spectral whitening (Figure 2.12) we see that the long period signal is not visible anymore.

Low-pass filter

In the amplitude spectrum (Figure 2.7) there is a minimum at about 30 Hz, with two spikes below and something different going on for the higher frequencies. It was therefore decided to study the frequencies up to 30 Hz. To remove the frequencies above this point, a Butterworth filter using the butter function in Matlab was used. To filter both ways, the function filtfilt in Matlab was also utilized. The order of the filter was chosen as 4 to filter out most of the higher frequencies and minimize Gibb's phenomenon. When using filtfilt, the order is 2N, so N was set equal to 2. Filtering has to be done after the spectral whitening so that what is removed by the filter does not get amplified by the spectral whitening. Figure 2.17 illustrates the frequency response of the filter with different orders.

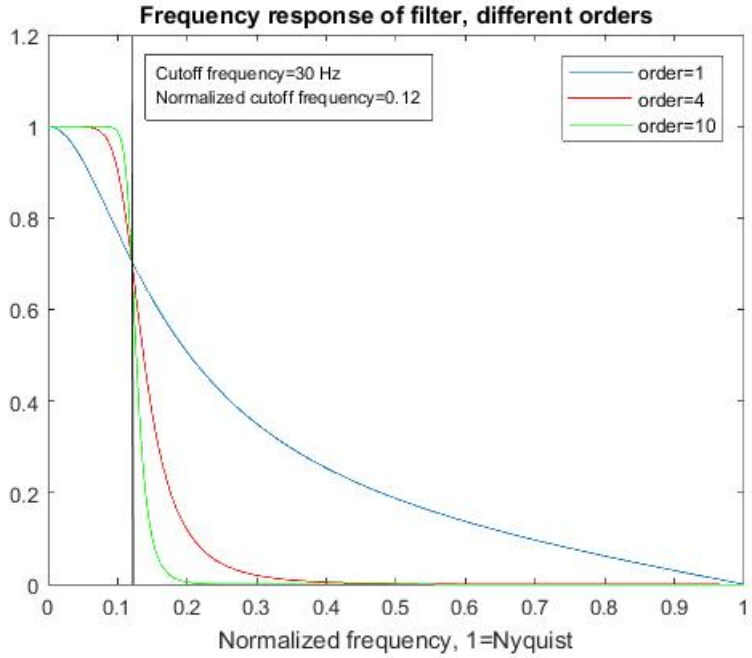

Figure 2.17: *Frequency response of the filter. When the order is 1, a lot of the higher frequencies still pass. When the order is 10, the filter is very box like. Since a smooth version of a box will lead to much less ripples in the time domain and we want to remove the higher frequencies, something in between these values was desired. With the order equal to 4 the filter is not as brutal as 10 and less forgiving than 1.*

In the previous figures detrend and low-pass filtering was done before carrying out the cross-correlation. Figure 2.18 shows stacked cross-correlation across the system without spectral whitening, but as opposed to Figure 2.11, detrend and low-pass filtering done after the cross-correlation. The correlation was then stacked and normalized. This gave similar results to the example where detrend and filtering was done before, but there was much more high frequency, leading to a thicker trace. When you filter after the correlation, you only filter once. When you filter before the correlation, you actually filter twice, since you filter each signal. This is equivalent to a higher order filter. It was

therefore preferable to do detrend, spectral whitening and low-pass filtering before the cross-correlations.

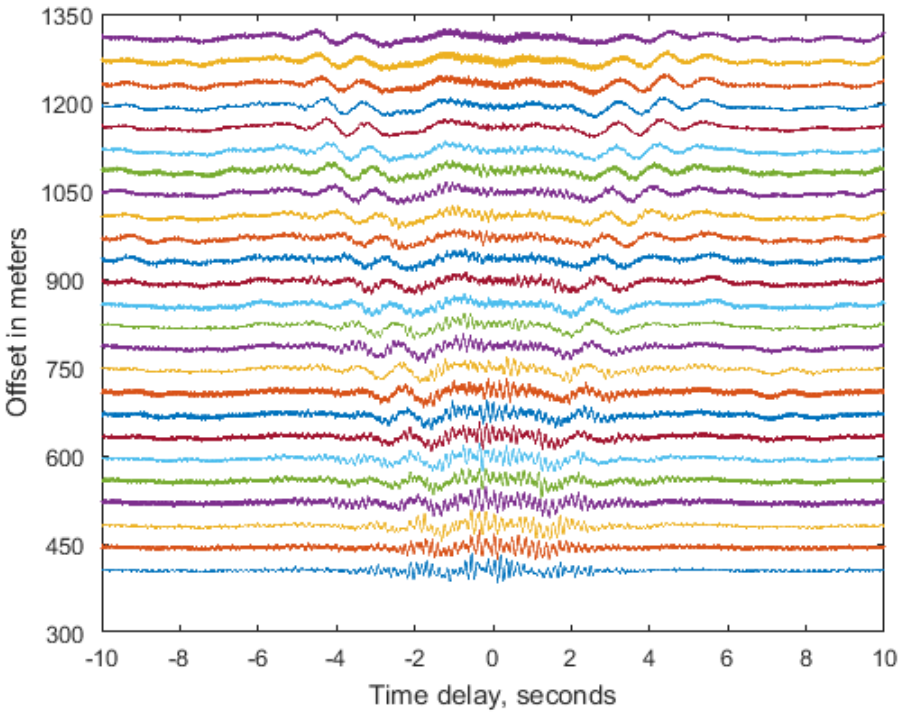

Figure 2.18: *Same as Figure 2.11 but with detrend and filtering carried out after the cross-correlation.*

Normalization

The data was normalized by dividing the cross-correlations with the maximum of the absolute value of each cross-correlation. This was done to help visualize the results, since the values were so small and we wanted to visualize them in an offset plot. When using spectral whitening, the normalization was not always necessary. This could be because spectral whitening is similar to normalization, just in the frequency domain.

An alternative is to multiply the correlations by a factor. This worked well when multiplying by 100 and 150, and was the case when spectral whitening was used. When not using spectral whitening, the values got very small and the correlations were multiplied by very large values. This is shown in Figure 2.19.

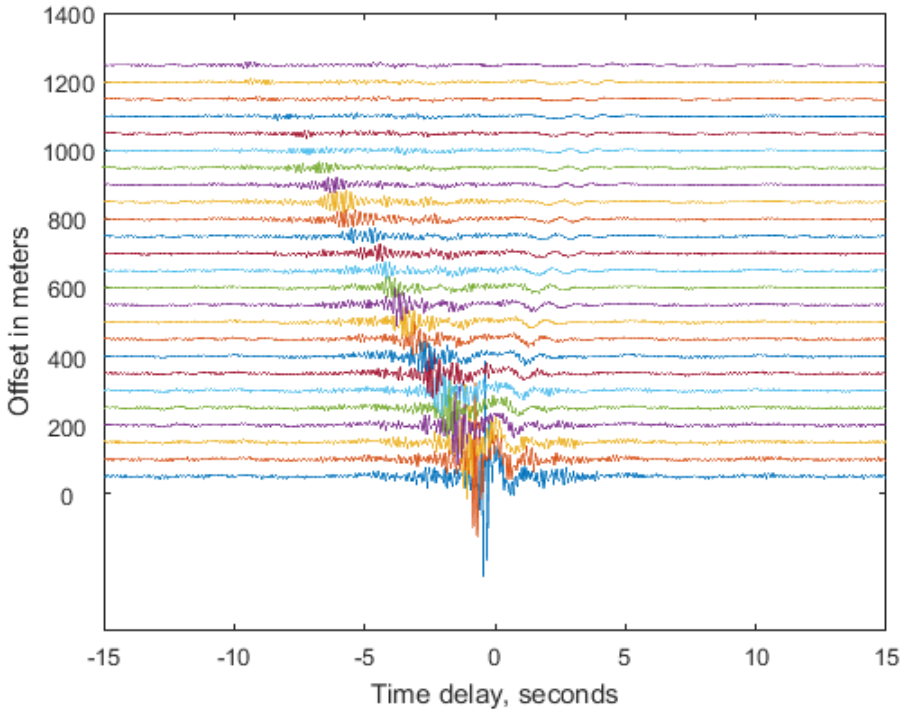

Figure 2.19: *Same as Figure 2.12 without normalization. The correlations were multiplied by a factor of* 10^6*. The small offset correlations dominate the plot.*

Figure 2.19 shows the stacked cross-correlations on line one without spectral whitening. Detrend and filtering was done before the cross-correlations, and the correlations were multiplied by a factor of 10^6. In this case the correlations from the stations close to the platform got very large amplitude compared to the ones further away. This is because there is more noise close to the platform. Since the maximum value from each correlation is used when normalizing, this problem can be avoided using normalization. Normalization was used consequently, since it worked in all cases.

Stack

In order to be useful, noise needs to be analyzed on a long enough period of time. This is usually achieved by cross-correlating a signal on several small time intervals and stack the resulting traces. We did the cross-correlations five-minute traces and the correlations were stacked together and divided by the number of traces used, to reduce noise and improve overall data quality.

To figure out how much time was needed to stack, the correlations were tested for one hour, eight hours and twelve hours. The stacked correlations presented are from line one with detrend, spectral whitening and a 2 Hz low pass filter performed before the cross-correlation. The correlations were normalized. The results from stacking different periods of time for the correlations along line one are presented in Figures 2.20 to 2.23.

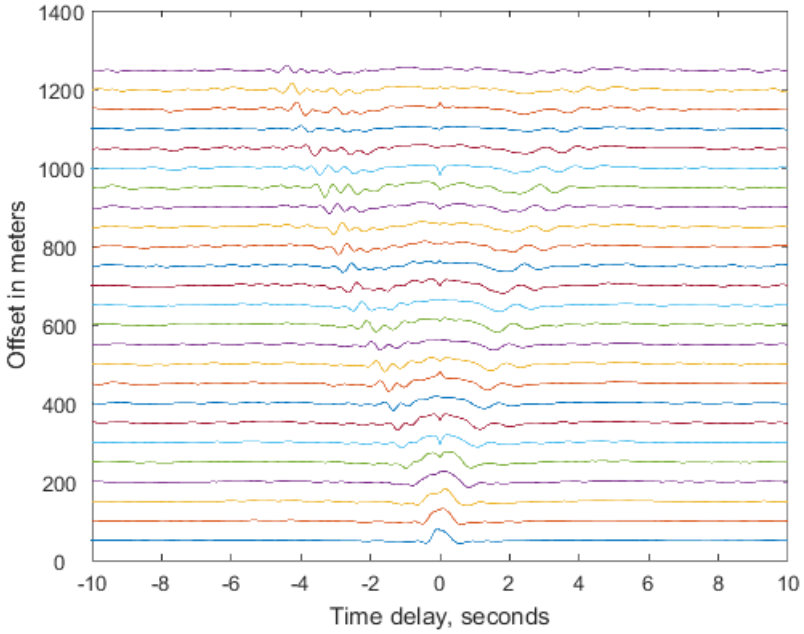

Figure 2.20: *One-hour stacked cross-correlations along line one. Detrend, spectral whitening and a 2 Hz low pass filter was applied before the cross-correlation. There are spikes around zero lag time, going up and down for different correlations.*

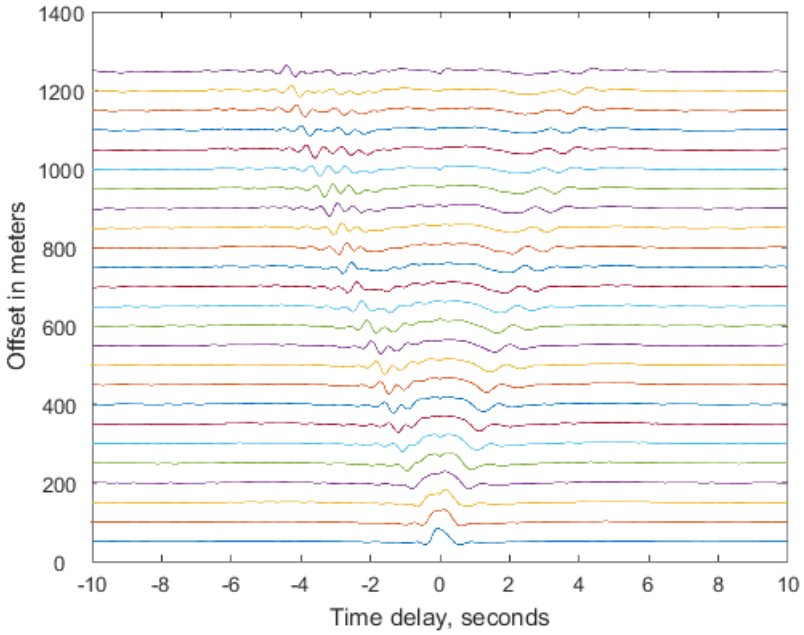

Figure 2.21: *Same as Figure 2.20 for eight-hour stack. Most of the spikes around zero lag time are no longer present.*

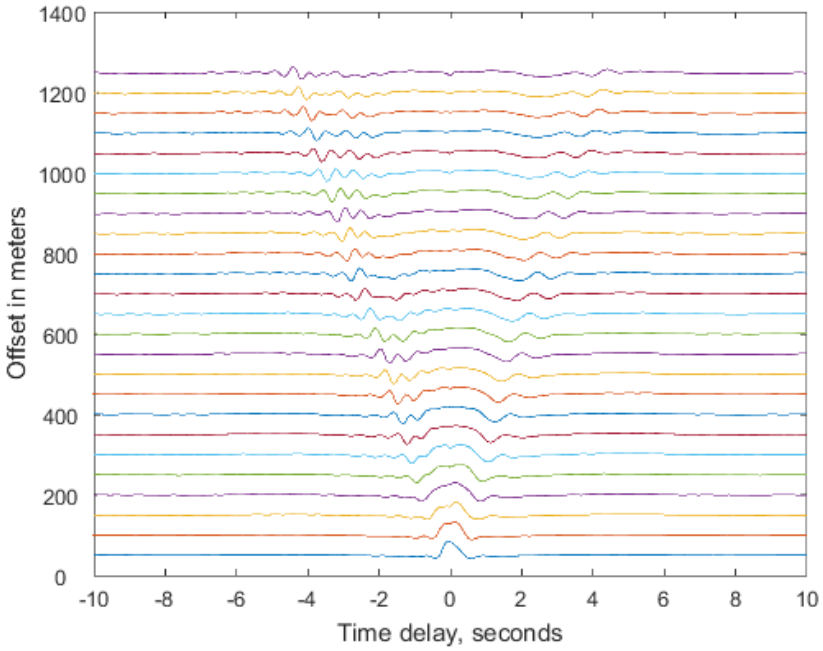

Figure 2.22: *Same as Figure 2.20 for twelve-hour stack. Not much change from stacking eight hours.*

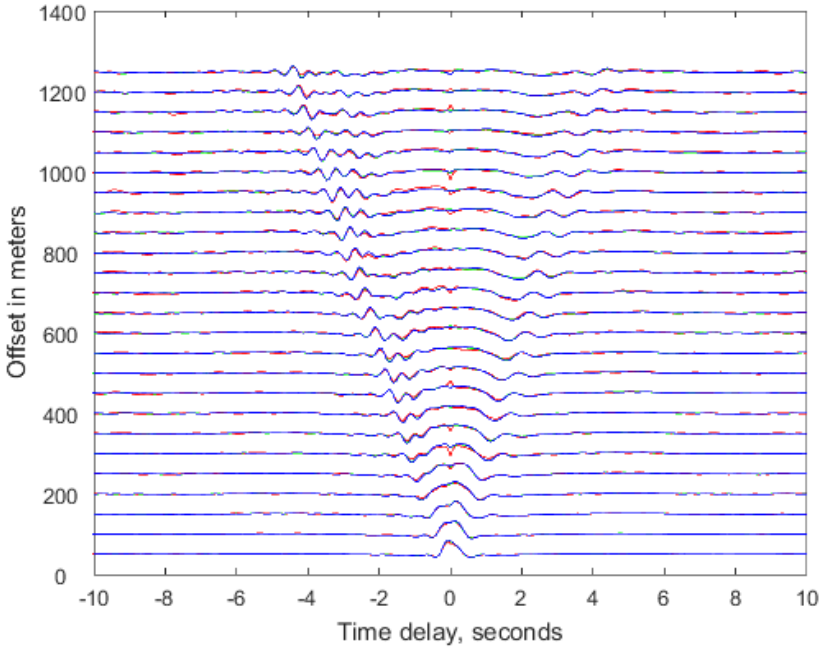

Figure 2.23: *Same as Figure 2.20 for one(red)-, eight(green)- and twelve-hour(blue) stacked cross-correlations along a line. The eight-hour cross-correlation in green is almost not visible when plotted before the twelve-hour correlations because they are so similar*

On Figure 2.20 we can see one-hour stacked cross-correlations from along line one. For stacking one hour, there are some spikes occuring in the middle of the plot going up and down for different correlations. This could imply that we need to stack more time. Stacking eight hours (Figure 2.21) and twelve hours (Figure 2.22) removed the spikes in most cases. There was no big difference between stacking eight hours and twelve hours, which is shown in Figure 2.23.

Figure 2.23 shows the one-, eight- and twelve hour stacked cross-correlations along line one. One hour is in red, eight hours in green and twelve hours in blue. When plotting the correlations together, the eight-hour cross-correlation is almost invisible because the twelve hour cross-correlation is so similar. This confirms that there is not much improvement from stacking eight to stacking twelve hours, and shows that eight hours is sufficient to get accurate Green's functions. To see if this was also the case for the correlations from interstations across the system, stacking different numbers of hours was also done for the correlations of station pairs across the system. The results are presented in Figure 2.24.

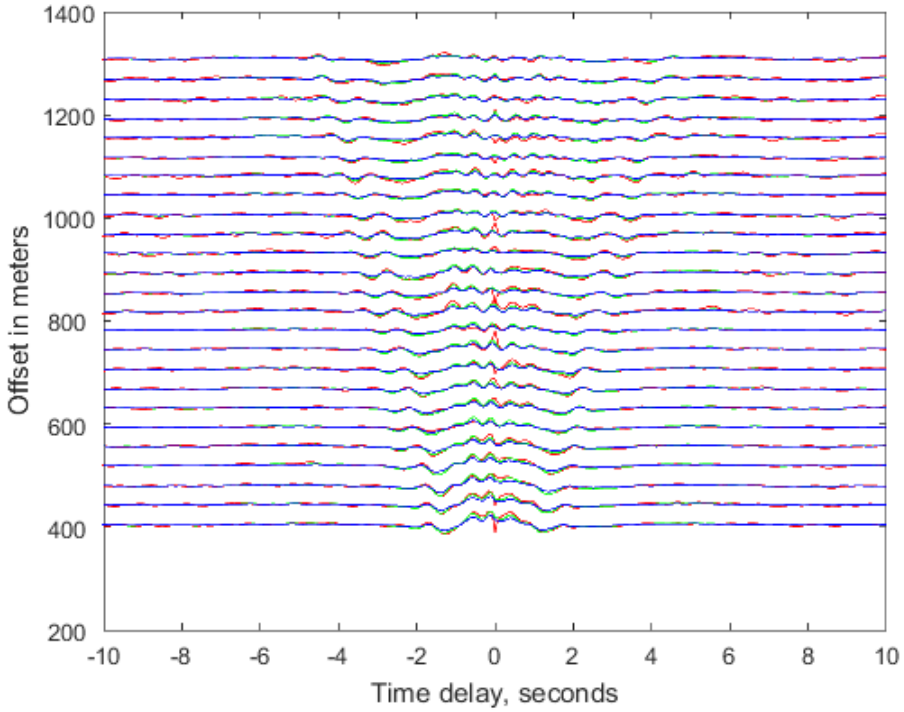

Figure 2.24: *Same as Figure 2.23 for the correlations across the system. There is a larger difference in stacking eight and twelve hours than for the case along the line.*

Figure 2.24 shows the stacked correlations for one-, eight- and twelve hours for interstations across the system, in red, green and blue respectively. The results from one hour of stacked data gave the same type of spike at about zero time lag as we observed from

the correlations from line one. These were mostly removed by stacking eight and twelve hours. However, there were some features in the center of the plot that did not disappear. Therefore one might have to stack more than twelve hours or add some more filtering to remove these features. There was a larger difference in stacking eight and twelve hours than for the case along the line. Because of this, twelve hours were stacked in the case of the correlations across the system.

2.4 Velocity and frequency estimation

Knowing the velocity is important to figure out what types of waves we are dealing with. Since the time lag corresponds to the traveltime and we have the interstation distance, we can calculate average velocites. To estimate velocities of different waves, a line was drawn through the feature and the difference in distance over the difference in time was calculated. You get the phase velocity from following some peaks, while you get the group velocity from following the maximum amplitude of the envelope. We start with the cross-correlations previously presented in Figure 2.11 and 2.16, which are shown side by side in Figure 2.25.

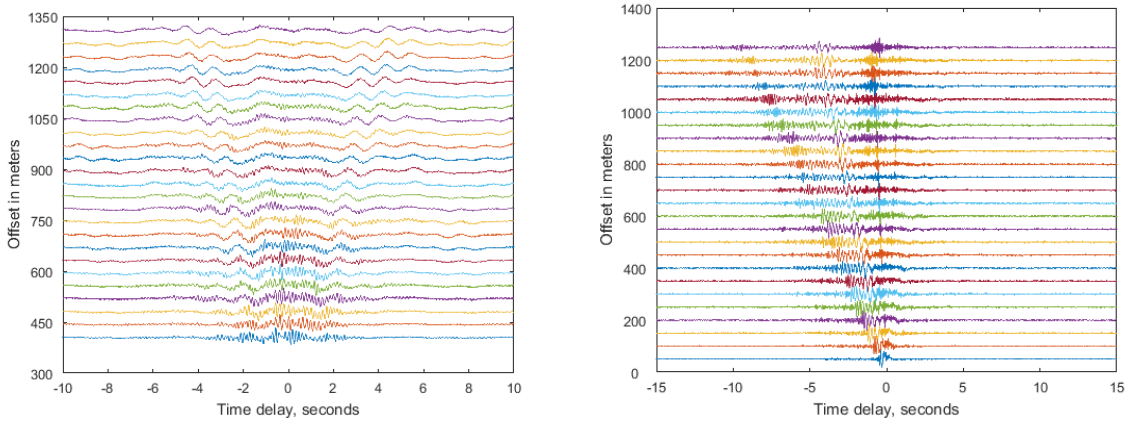

(a) *Same as Figure 2.11.* **(b)** *Same as Figure 2.16*

Figure 2.25: *Cross-correlations used for velocity estimation. Left side shows the correlations from interstations across the system. Right side is the correlations from line one.*

Figure 2.25a shows the cross-correlations from the station pairs across the system. Here we have noise coming from both directions. Figure 2.25b shows the correlations from line one. Here we have noise mainly coming from one direction. In the case of the correlations from the interstations across the system, the correlation is symmetric and we have noise coming from all directions. It can therefore be used to calculate velocities. In the case of the correlations from line one, the array is inline with the platform, which is a major source of noise, and can therefore also be used for velocity estimation. The group velocity and a phase velocity was estimated for the wave from Figure 2.25a and the group velocity

was found for the three waves from Figure 2.25b. The procedure and results are presented in Figure 2.26.

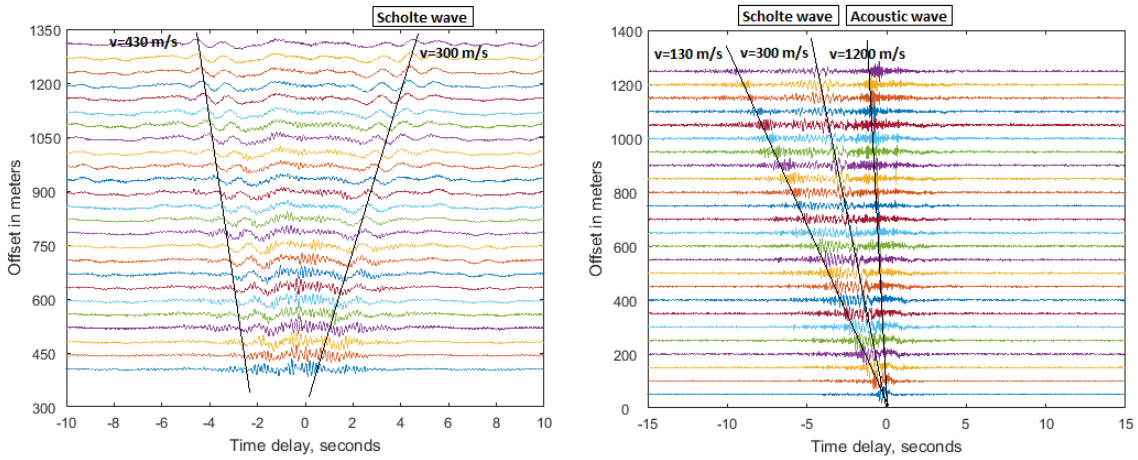

Figure 2.26: *Cross-correlations with velocities. Left side: Correlations from across the system. Scholte wave group velocity and phase velocity. Right side: Correlations from along line one. Acoustic wave, Scholte wave and an unknown wave with group velocities.*

Figure 2.26 shows the cross-correlations with velocities. On the left side we have one wave, which is symmetric around zero seconds. The group velocity was 300 m/s, while the phase velocity calculated was 430 m/s. Following some other peaks, would yield a different phase velocity. If the wave was not dispersive, the group and phase velocity would have been the same. On the right side of the figure we have three waves, which have different velocities. The fastest wave, which is found closest to zero, has a group velocity of 1200 m/s, the middle has a group velocity of 300 m/s and the last has a group velocity of 130 m/s, which is very slow. One of the waves from the correlations from line one had the same velocity as the one from correlations of stations across the system. This could be the same wave. To figure out what types of waves we are dealing with, further investigation is needed.

The frequency content can be explored to further determine the type of wave. A test was done by utilizing different band-pass filters on a specific stacked correlation from the correlations along line one to see at which frequency intervals the waves were present. The interval length was 1 Hz, starting with from 2 to 3 Hz, then 3 to 4 Hz, up to 29 to 30 Hz. The results were plotted and presented in Figure 2.27.

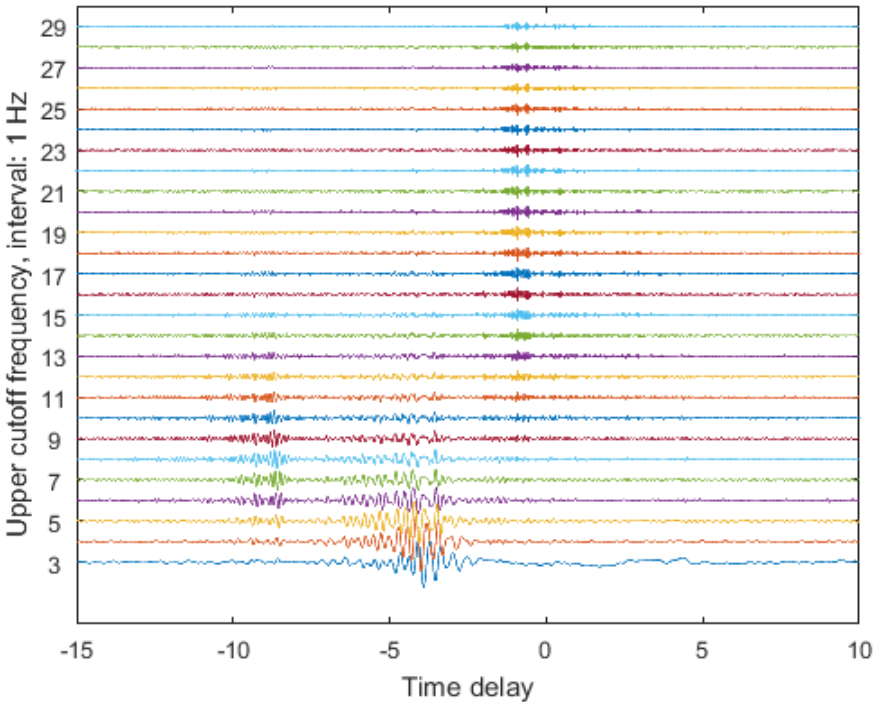

Figure 2.27: *The band-pass filters show that the fastest wave was present at the highest frequencies and the largest range. It was the strongest at around 20 Hz. The middle wave was present in the first frequency interval and was the strongest for the lowest frequencies. The slowest wave appeared at a little higher frequencies than the previous, and was the strongest around 8 Hz.*

Figure 2.27 shows the results from the band-pass test with time delay on the x-axis and the upper cutoff frequency of the filter on the y-axis. From the band-pass filters we observe that the fastest wave from Figure 2.26 has the highest frequencies, being strongest at around 20 Hz. The middle wave is present in the first frequency interval and is strongest for the lowest frequencies tested. The slowest wave appears at a little higher frequencies than the previous, and is strongest around 8 Hz.

Due to the high velocity, the fastest wave with the highest frequency could represent the acoustic wave. The wave with velocity of 300 m/s had low frequency, was symmetric and dispersive. It was therefore believed to be the Scholte wave. A Scholte wave is an interface wave, and is basically a Rayleigh wave under water. As for the last wave, it had very low velocities, and the type of wave is unknown.

Quality of the Green's function

The symmetry of the cross-correlation is a way of testing the quality of the Green's function. For the cross-correlations along line one, the noise from the platform was very dominating, affecting the symmetry of the cross-correlations. The noise from the platform also appeared to have higher frequencies than the other noise sources. So, to get accurate

velocities, we need to find out how low frequencies we have to go to in order to get a symmetric cross-correlation, where the platform noise is no longer present in the data. To do this, another band-pass test was performed, but for lower frequencies. In this case eight hours of data was used. Detrend, spectral whitening and a 10 Hz low pass filter was applied before carrying out the cross-correlation. Stacking 8 hours lead to Figure 2.28.

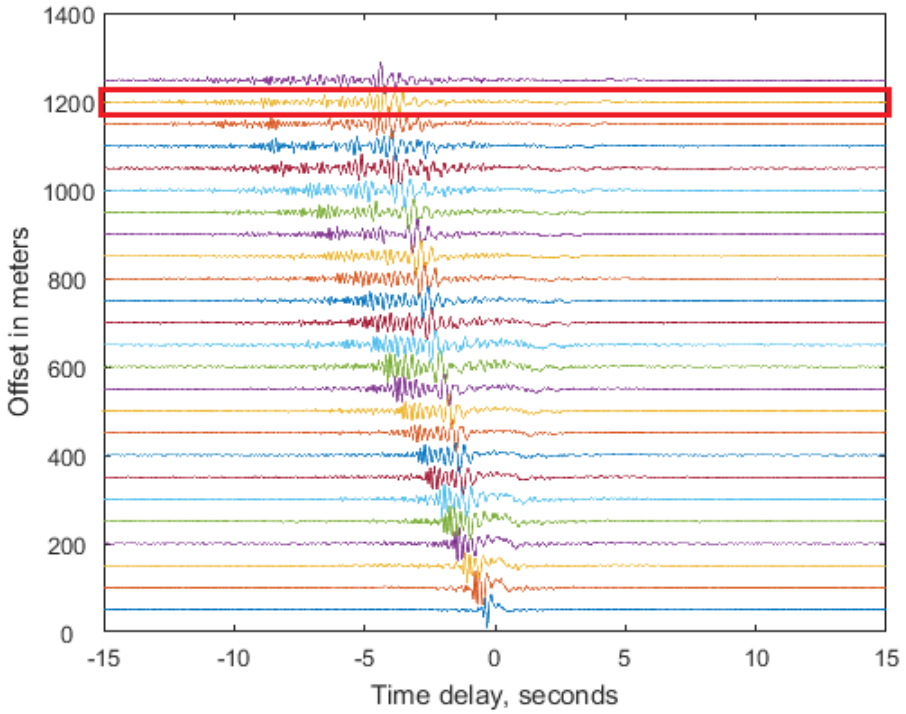

Figure 2.28: *Eight hours of stacked cross-correlations along line one using a 10 Hz low-pass filter. Correlation used for band-pass testing is indicated in red.*

One of the correlations from Figure 2.28 is chosen for the band-pass tests, as indicated on the figure. This correlation was picked because it was one of the correlations where it was easier to separate the features from each other. The correlation is presented with causal and acausal parts separately in Figure 2.29.

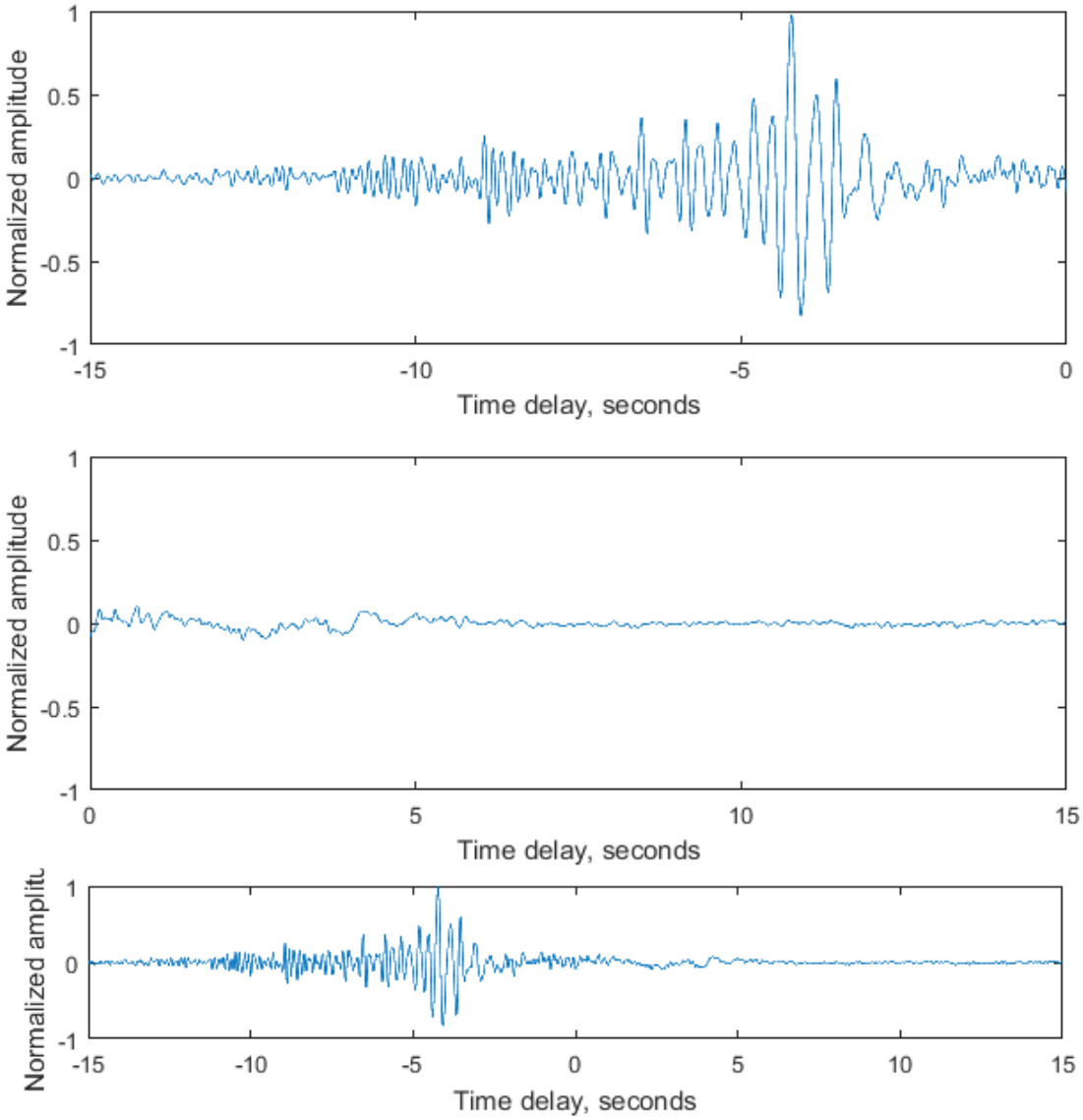

Figure 2.29: *Station 10 correlated with station 34. 8 hours of data was used, and detrend, spectral whitening and a 10 Hz low pass filter was applied before the cross-correlation. The correlation is normalized. The top figure represents the negative time lags up to -15 s, the middle the positive time lags up to 15 s. The last is the the previously described combined.*

Figure 2.29 shows the cross-correlation of station 10 and station 34 with normalized amplitude on the y-axis and time delay on the x-axis. The top figure represents the negative time lags up to -15 s and the middle the positive time lags up to 15 s, both provided to see the details of the trace. We see three events for the acausal part of the trace, while there is very little going on for the causal part. The lower part is the the previously described parts combined. A band-pass test was performed on the correlation for frequencies up to 10 Hz, and the results are presented in Figure 2.30.

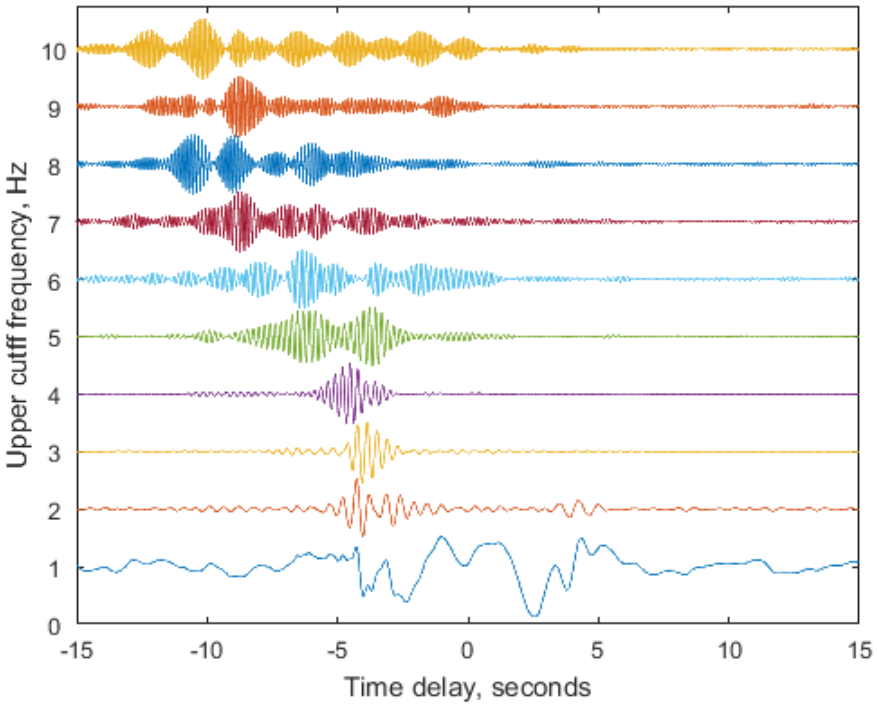

Figure 2.30: *Band-pass test with intervals going from 0.1-1 Hz, 1-2 Hz, 2-3 Hz up to 9-10 Hz applied to the correlation from Figure 2.29.*

Figure 2.30 shows the results from the band-pass test on the signal from Figure 2.29. The intervals of the band-pass filters are equal to 1 Hz, going from 1-2 Hz, 2-3 Hz up to 9-10 Hz, with the exception of the first interval, which goes from 0.1-1 Hz. The upper cut off frequency is indicated on the y-axis on the figure. The figure shows that there is not much to see for positive lag times before we go down to 2 Hz. Above 2 Hz the correlation is dominated by noise coming from the platform. When the frequencies above 2 Hz are filtered out, the only feature that is left is visible for both positive and negative time lag. Here we have noise coming from all directions. The response for negative time lag, however, has some irregularities, which indicates that we have two waves interfering and the correlation is still not very symmetric. This implies that the correlation is still affected by the platform noise.

Up to 4 Hz, the shape of the response for negative time lag still looks pretty nice. If we assume that the noise is coming from the platform, and the lines of stations point towards the platform, we can use the energy coming from the platform as well as the low frequency noise.

2.5 Comparison of different configurations

Along line one

To look for changes along line one comparison was done along the configuration shown in Figure 2.8 for line one, but with different fixed stations. The first reference station was station 10, which produced 25 cross-correlations and was the one presented in the previous sections (Figure 2.21). Then station 20 was used as a reference station and was correlated with station 21 to 35, resulting in 15 correlations. Lastly five correlations were produced by correlating station 30 with station 31 to 35. This is shown in Figure 2.31.

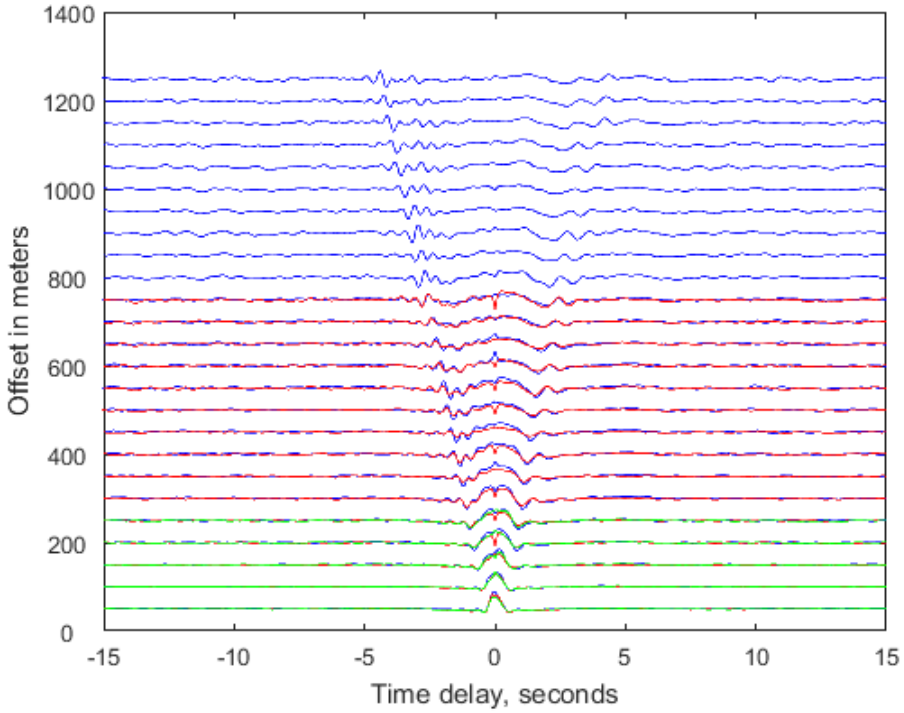

Figure 2.31: *Station 10(blue), 20(red) and 30(green) were used as fixed stations producing 25, 15 and 5 correlations respectively from line one. Eight hours were stacked and a 2 Hz low pass filter was applied. The velocities match well.*

In Figure 2.31 the correlations from the different fixed stations are plotted together as a function of distance to the reference station. The correlations with station 10 as a reference are plotted in blue, the correlations with station 20 as a reference in red and the ones with station 30 as a reference in green. Up to 300 m we have three superimposed traces that correspond to different sections along line one. The same goes for the two superimposed traces from 300 m up to 750 m. The velocity matches well for the different fixed stations, and it was not observed any phase change. However, there are some spikes at zero time lag, especially for the correlations where station 20 is used as the fixed station, which were ignored.

If there is no change in the subsurface along this line, one would not expect any difference in velocity or phase. Since the different parts along the line are so similar, with no phase shift, the subsurface along the line can be seen as rather homogeneous.

Different lines

To see if there was any differences between the different lines, cross-correlations were also carried out along all of the four lines shown in Figure 2.8. The results from different lines were presented together for comparison. In Figure 2.32, the results from line two and three are plotted together.

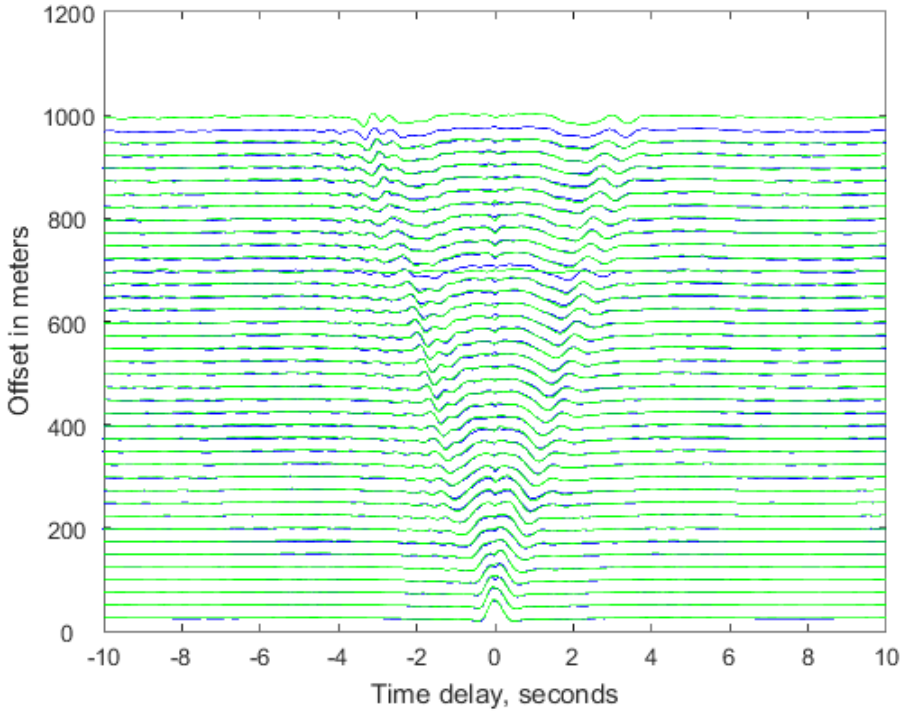

Figure 2.32: *Same as Figure 2.31 for line two and three.*

Figure 2.32 shows the cross-correlations from the two shorter lines of the array (2.8). Plotting the shorter lines together revealed that their results matched very well, both for the longer and the shorter periods. This is reasonable since the lines are so close. To see if the two long lines also yielded similar results, the correlations from line one and four were presented together in Figure 2.33. All of the four lines are presented together in Figure 2.34.

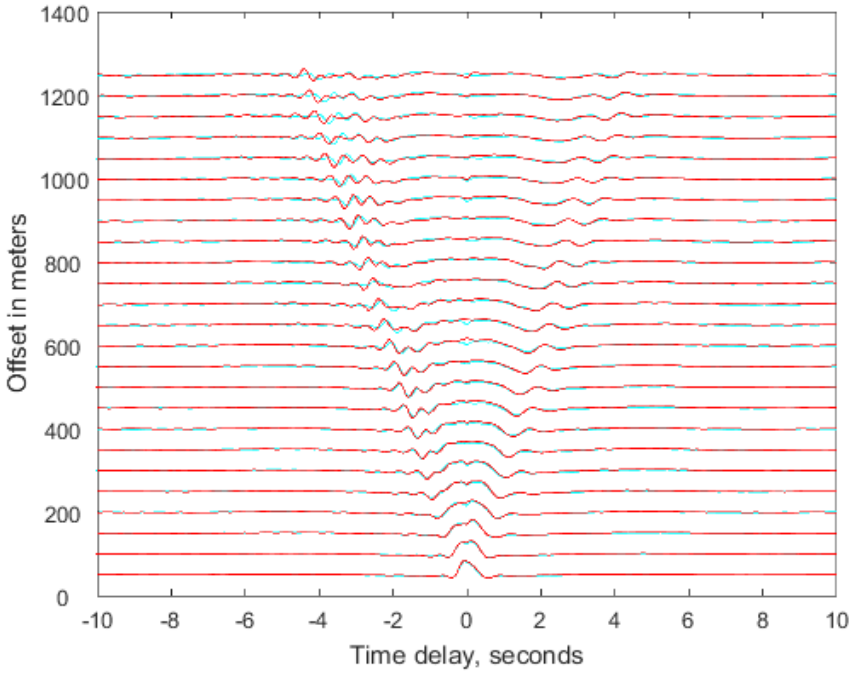

Figure 2.33: *Same as Figure 2.31 for line one and four.*

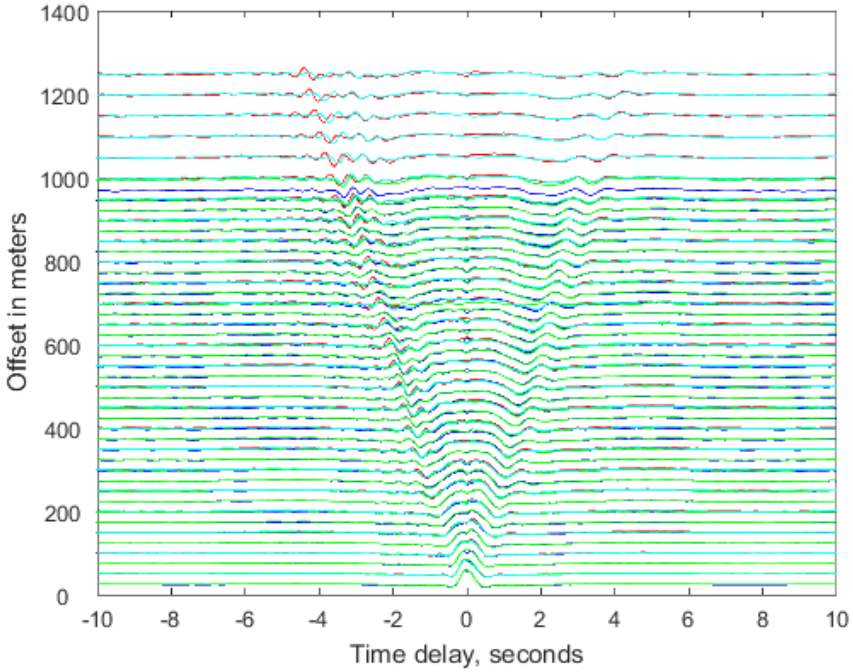

Figure 2.34: *Same as 2.32 for all lines plotted together. The shorter lines are in green and blue, while the longer are in red and cyan.*

Figure 2.33 shows the cross-correlations for the longer lines plotted together. For the longer lines, the results are very similar for positive time lag, where the long period waves match perfectly, but for negative time lag there is a slight difference in phase for the short period waves. This makes sense because they are further apart than the shorter lines.

The cross-correlations from all the lines in the array pointing towards the platform are plotted together in Figure 2.34. The shorter lines are in green and blue, while the longer are in red and cyan. Overall there is not much difference between the different lines. The same features appear, and the velocity is also very much the same. We see that the long period waves mach up well for all of the four lines.

Across vs. lines

To see if there was any changes between the four lines and the area between the lines, the correlations from the interstations across the system were plotted together with the correlations from line one for comparison. The results are shown in Figure 2.35.

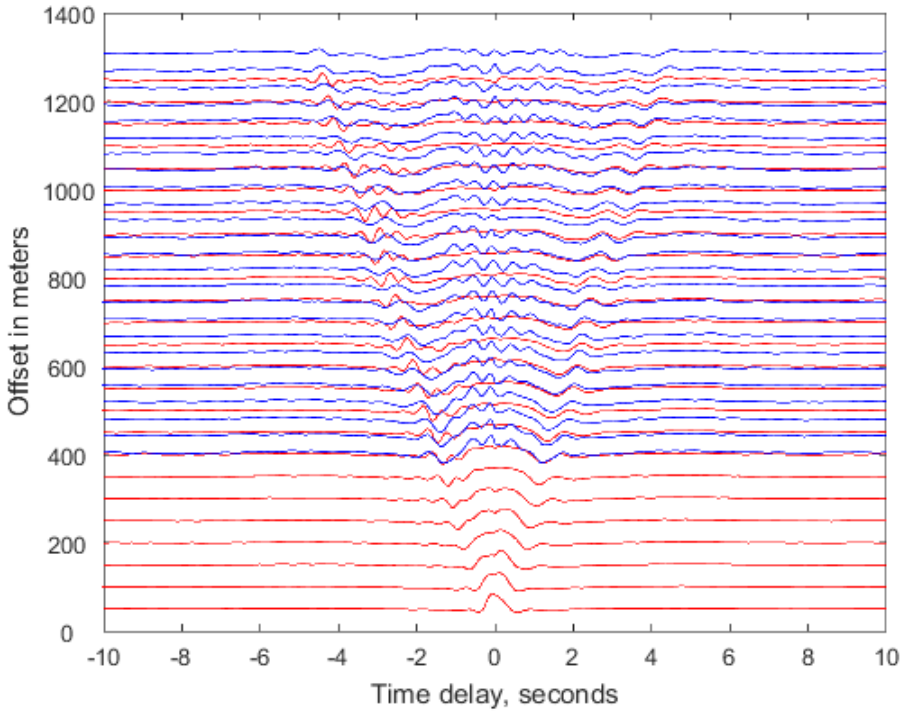

Figure 2.35: *Same as Figure 2.32 for line one with eight hours stacked and for the interstations across with twelve hours stacked. The correlations across the system represented with blue, while line one is presented in red. The correlations across the system were multiplied by 1.5.*

Figure 2.35 shows the twelve-hour stacked correlations from interstations across the system (blue) with the eight-hour stacked correlations from line one (red). Since the amplitudes for the cross-correlation across the system were smaller than the ones along the line, the

correlations were multiplied by 1.5. The long periods match up nicely, while the short periods do not. This makes sense, since the shorter periods come from the platform. The platform is almost perpendicular to the configuration across the system, and therefore we get the shorter periods at around zero time lag. Line one points towards the platform, and therefore the higher frequencies are seen on the negative time lag. The longer periods come from all directions. The results were the same when comparing the correlations from across the system with the other lines.

2.6 Comparison of different components

Different components of the receiver pick up different waves. Therefore it was carried out cross-correlations for all the different components available, which was the vertical-, radial-, transversal- and hydrophone component. The data is rotated towards the platform, so the radial is the direction of the lines of the array pointing towards the platform, while the transversal is perpendicular to the vertical and the radial. Recordings from the radial component were correlated with other radial component recordings, transversal with transversal and hydrophone with hydrophone. The results from the radial component line one are presented in Figure 2.36.

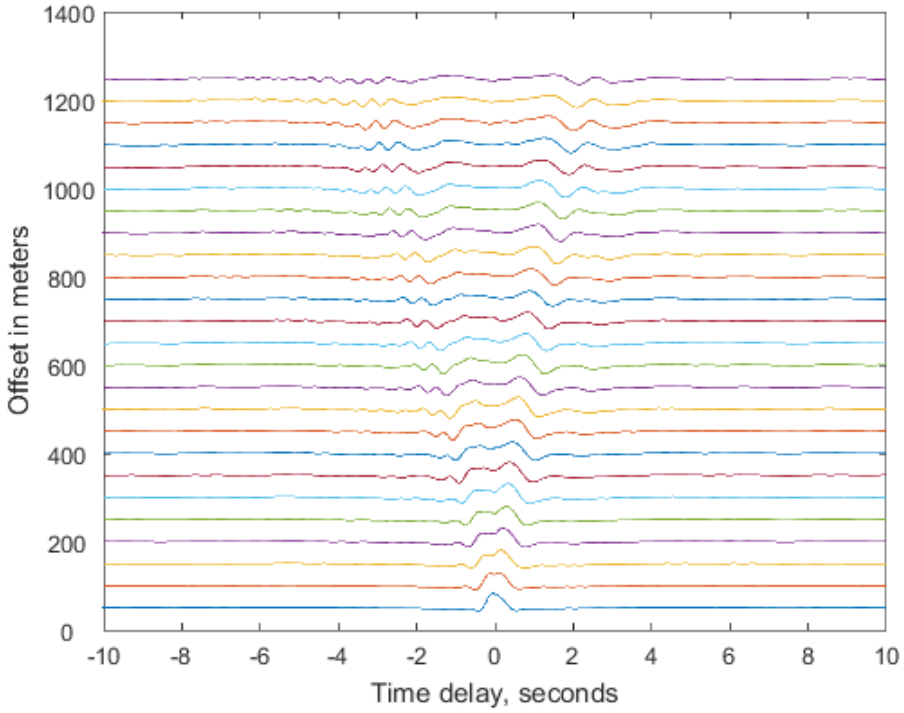

Figure 2.36: *Stacked R-R cross-correlations for line one. Detrend, spectral whitening and a 2 Hz low pass filter was applied before carrying out the cross-correlations. Then the correlations were stacked and normalized. The same 'V'-shape appears as for the vertical component. The amplitude is higher and the period longer for negative time delay.*

Figure 2.36 shows the stacked cross-correlations for the radial component line one. A 2 Hz low pass filter was applied to the data after detrend and spectral whitening. Then the cross-correlations were carried out and normalized. Eight hours of data was stacked. The stacked radial correlations display the same characteristic 'V'-shape as for the vertical component. The amplitude is higher and the period longer for positive time delay compared to negative time delay. The arrival time is the same as for the vertical. Figure 2.37 shows the results for the transversal component.

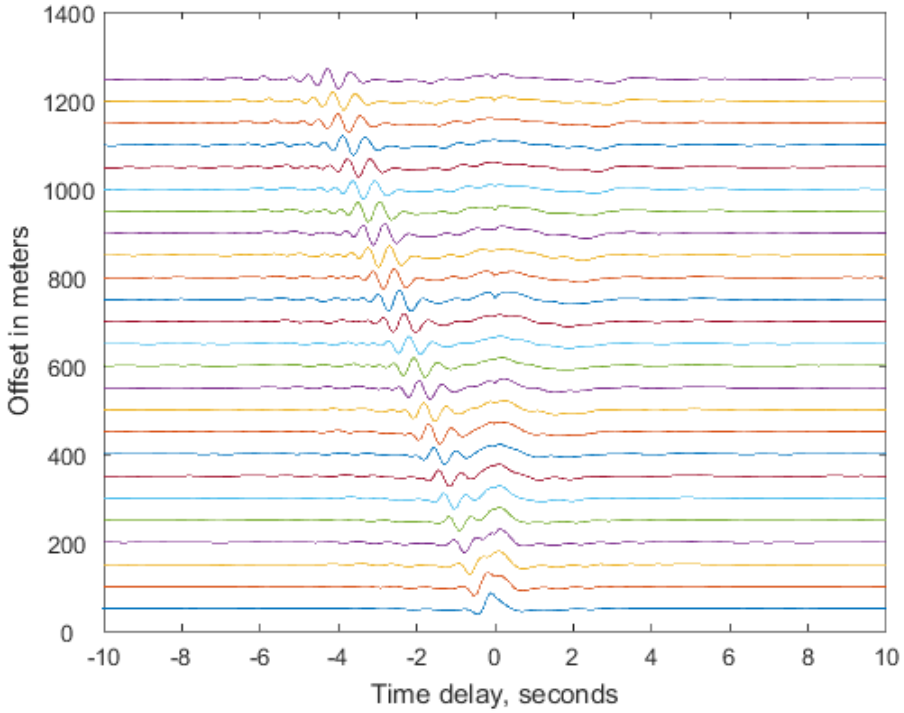

Figure 2.37: *The same as Figure 2.36 for the transversal component line one. The negative response has a very high amplitude, whereas the positive is almost invisible.*

For the transversal component (Figure 2.37), the correlations do not display the characteristic 'V'-shape observed for the radial and vertical component. There is mostly an acausal response with high amplitude and only very long periods in the causal part. The correlations from the hydrophone are presented in Figure 2.38.

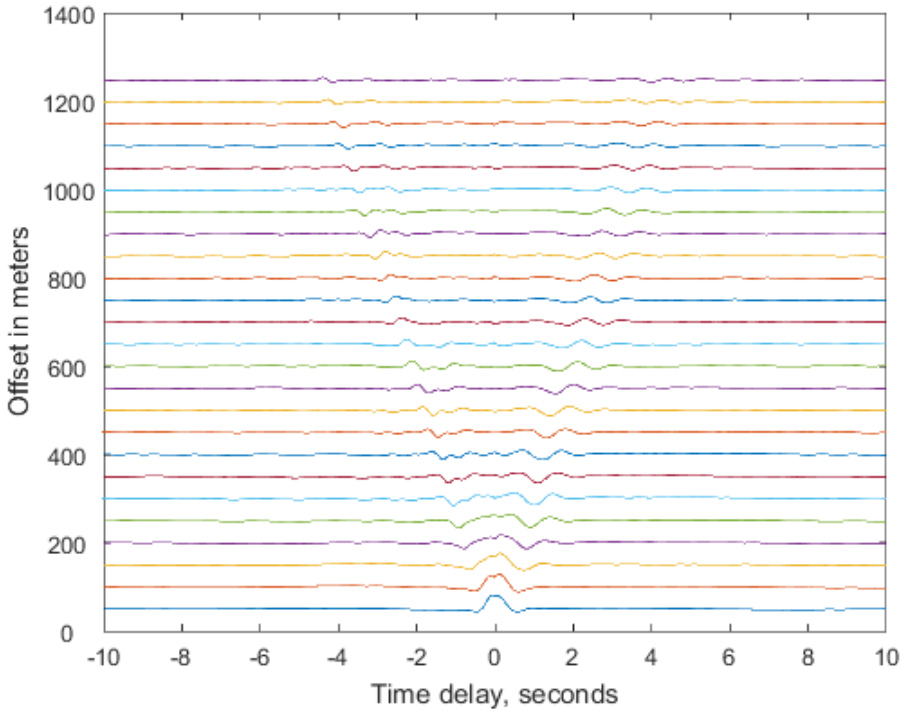

Figure 2.38: *Same as Figure 2.36 for the hydrophone component line one. The correlations display the symmetric V-shape, with the amplitude and period larger for positive time lag than negative.*

The correlations from the hydrophone component (Figure 2.38) display a symmetric V-shape, like the vertical, radial and hydrophone components. The causal response has a larger amplitude and period than the acausal part. To further investigate the differences between the different components, the results from all components were plotted together in Figure 2.39.

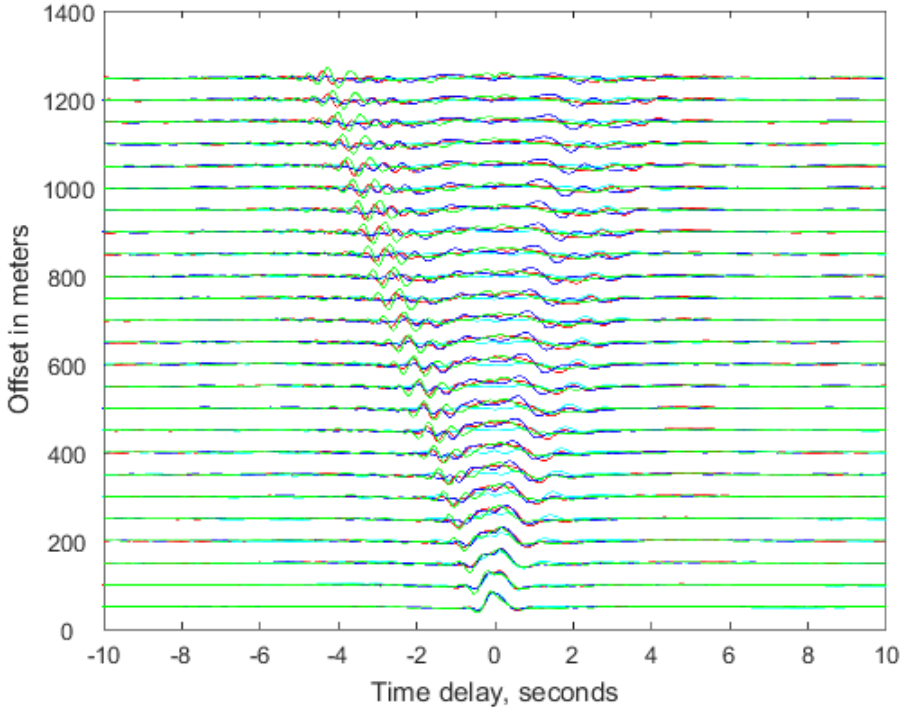

Figure 2.39: *Stacked Z-Z, H-H, R-R and T-T cross-correlations for line one. The correlations from the hydrophone is presented in cyan and the vertical, transversal and radial in red, green and blue respectively.*

Figure 2.39 shows the correlations for the hydrophone-, vertical-, transversal- and radial component in cyan, red, green and blue respectively. Looking at the cross-correlations from all components together, we see that the radial component has a higher amplitude than the hydrophone. The transversal component has the highest amplitude for short periods and the radial the largest amplitude for longer periods. The transversal component is the only component that mostly has an acausal response.

2.7 Changes over time

To look for changes in the overburden over time, 8 hours of data was extracted from each day for a period of 32 days available. There was some time missing throughout the data, however the data was treated as if it was not. This resulted in the eight hours not being from the exact same time of the day, and the eight hours were sometimes from larger time periods. The data from each day was processed as presented in the previous sections, and the results are presented in Figures 2.40 to 2.42.

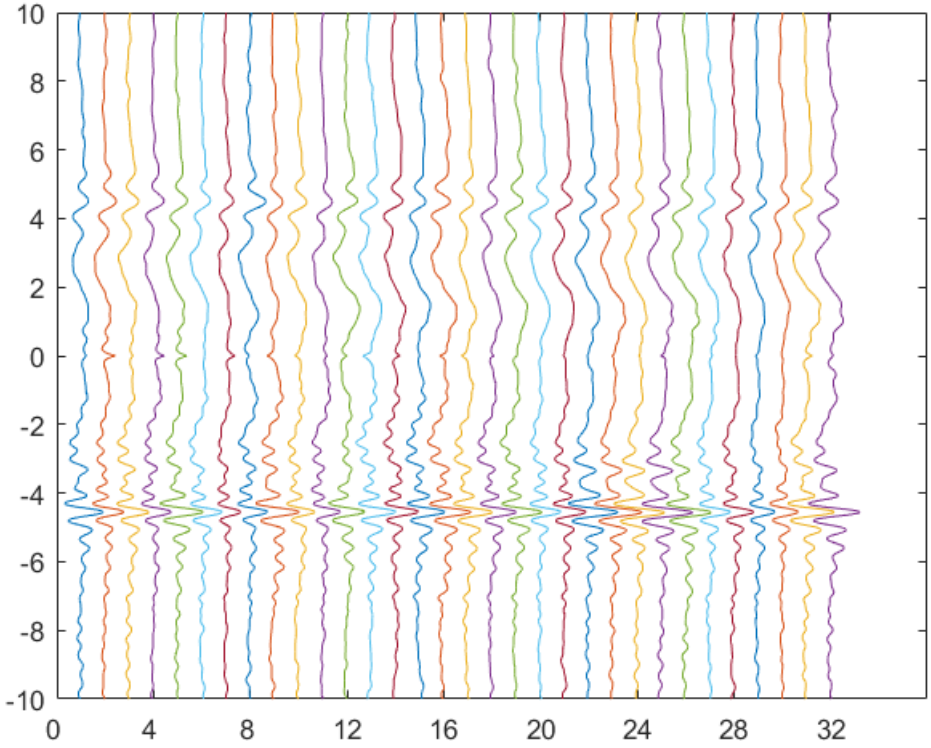

Figure 2.40: *Looking for changes with time along line one. Station 10 correlated with station 36. We have day on the x-axis and time lag in seconds on the y-axis. Except for the difference in amplitude, the correlations look very similar, peaks match up nicely*

In Figure 2.40 the traces from day 1 to 32 are plotted next to each other with the day on the x-axis and the time lag on the y-axis, and they match up nicely. Except for the difference in amplitude, it was not spotted any phase change, as the peaks match up nicely. If the changes are small, it might be difficult to see the changes from trace to trace. Therefore the two extreme cases are displayed in Figure 2.41.

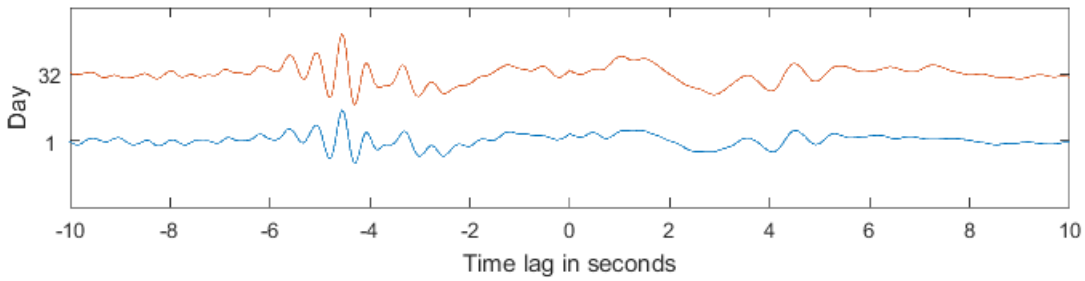

Figure 2.41: *Cross-correlation from day 1 and day 32.*

Figure 2.41 shows the correlation from day one plotted with the correlation from day 32, with time lag on the x-axis and the day on the y-axis. Also in the two extreme cases we

cannot observe any phase change, and it can therefore be assumed that there is no change in the traces from the days between day 1 and 32. To support this, the traces were also displayed with scaled colors in Figure 2.42.

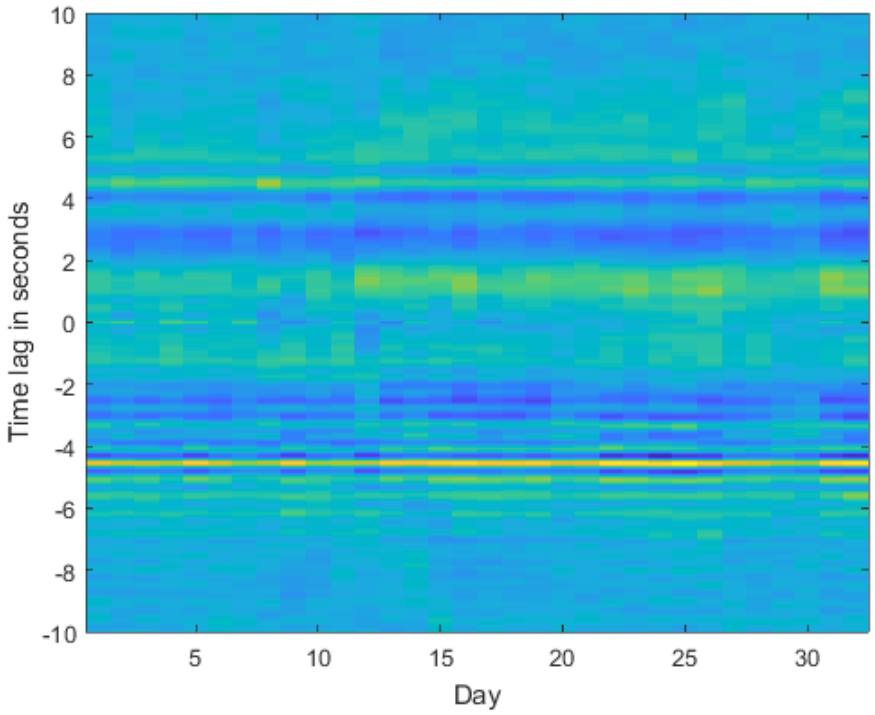

Figure 2.42: *Changes in time*

From the scaled image (Figure 2.42), it was observed a change in amplitude, but no change in phase. The same was the case for the other lines of the array. It was therefore not detected any changes in the overburden during this time period.

2.8 Resolution

From the cross-correlations we see no lateral variations. There are two possible reasons for seeing no variations: lateral homogeneity, or that the wave cannot see the heterogeneity. Therefore we calculate the Fresnel zones to check the last point.

The Fresnel zone is an area which depends on frequency and range, from which most of the energy of a reflection is returned and arrival times differ by less than one fourth a period from the first break. Waves with these arrival times interfere constructively and are detected as a single arrival. If a feature is smaller than the Fresnel zone, it can usually not be detected. Figure 2.43 shows how the Fresnel zone was found for a source and receiver on the same surface.

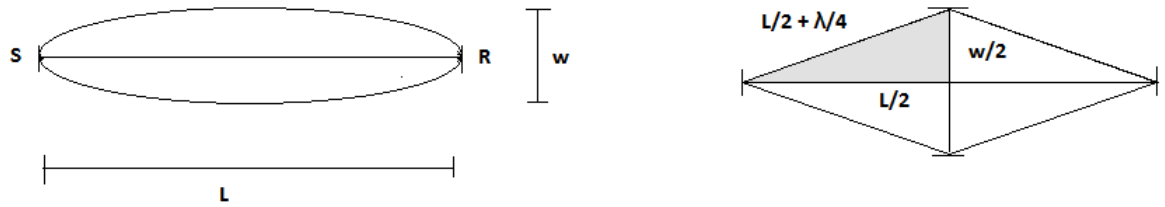

Figure 2.43: *Fresnel zone.*

Looking at Figure 2.43, L is equal to the distance between the source and receiver and w is the width of the Fresnel zone. The maximum width of the Fresnel zone will be at half the length of the source receiver distance. To find the width, the pythagorean theorem was applied, and the Fresnel zone was defined as $\lambda/4$. λ is the wavelength. Then we have

$$(w/2)^2 + (L/2)^2 = (L/2 + \lambda/4)^2 \tag{2.8.1}$$

Solving for w gives

$$w = \sqrt{(L\lambda + \lambda^2/4)} \tag{2.8.2}$$

The width of the Fresnel zone was calculated for three different frequencies, the maximum and minimum retrieved from the slowness frequency analysis, and one intermediate frequency. The respective velocities were used to find wavelength with the formula:

$$\lambda = v/f \tag{2.8.3}$$

Since the distance between the receivers varied, the width was calculated for the minimum and maximum distance between receivers, and a value between. The results are presented in Table 2.1.

f in Hz	c	λ in m	L=100 m	L=497 m	L=969 m
0.2	300	1500	844	1146	1420
2	300	150	144	284	389
4	300	75	94	197	272

Table 2.1: *The width (w) of the Fresnel zone calculated for different frequencies (f) and distances between receivers (L). The width increases as the length between receivers increases and with increasing wavelength (λ).*

Table 2.1 shows the width (w) of the Fresnel zone calculated for different frequencies (f) and distances between receivers (L). The width increases as the length between receivers increases and with increasing wavelength (λ). If a feature is smaller than the Fresnel zone, it may not be detected, so to be able to see a difference between the lines the distance

between the lines has to be larger than the width of the Fresnel zone, so that their zones do not interfere. The distance between the lines ranges from 32.47 m to 328,74 m.

For an interstation to be useful, we need at least 100 m offset. At 0.2 Hz, the Fresnel zones are from 844 to 1420 m. This is almost as large as the whole array. At 2 Hz, the zones range from 144 to 389 m, and for 4 Hz the Fresnel zones are from 94 to 272 m. We could therefore be able to see lateral variations for higher frequencies.

2.9 Discussion and concluding remarks on interferometry

From the interferometry we see that waves emerge from our cross-correlations, and stacking 8 hours is enough to get good results. We have high frequency noise (2-4 Hz) from the platform that can be used for interferometry along the lines since we know where the noise is coming from and the lines point in the direction of the platform. The lower frequency noise (below 2 Hz) is coming from all directions and can be seen on the correlation from the lines as well as the correlations from interstations across the system. There are no major changes with location or time. We get a signal on all components.

Chapter 3

Slowness-frequency spectra

Mainly surface waves emerge from cross correlations of ambient noise. Surface waves are dispersive, meaning that different frequencies travel at different velocities. The dispersive waves can be transformed into images of dispersion curves, called slowness-frequency spectra or dispersion images. A dispersion image shows which velocity the wave travels at different frequencies. It also shows us where we have energy.

3.1 Frequency-wavenumber analysis

To go from surface waves to dispersion images, frequency-wavenumber (f-k) analysis was used. f-k analysis transforms the data from the space-time domain into the slowness-frequency domain where the dispersion curve can be picked directly. This assumes that the wave at a given period travels with the same velocity along the whole array of stations considered. If not, the f-k image will not give a sharp dispersion. It is not a problem in this case, as we do not see large lateral variations. The process involves two linear transformations: a slant stack followed by a one-dimensional Fourier transform over τ (McMechan and Yedlin, 1981). The function used was written by Sascha Bussat in Matlab.

We have a signal with time on the y-axis and distance on the x-axis and we want to go from the (t,x)-domain to the (f,k)-domain. To do this we use the Fourier transform. The Fourier transform decomposes your signal in time into the different frequency components that make up your signal. This is the same that happens when light passes through a glass prism and exposes its color spectrum. The Fourier transform from time to frequency gives us

$$f(t) \xrightarrow{FT} F(\omega) = \int f(t) exp(i\omega t) dt \tag{3.1.1}$$

where ω is the angular frequency. The Fourier transform from space to wavenumber gives us

$$f(x) \xrightarrow{FT} F(k) = \int f(x) exp(-ikx) dx \tag{3.1.2}$$

where k is the wavenumber. Combining these two equations, we get:

$$f(t,x) \xrightarrow{FT} F(\omega,k) = \int\int f(x,t)exp(i\omega t - ikx)dtdx \tag{3.1.3}$$

We go from wavenumber (k) to slowness (s) and from angular frequency (ω) to frequency (f) by using the equations

$$k = s\omega \tag{3.1.4}$$

$$\omega = 2\pi f \tag{3.1.5}$$

Then we get

$$f(t,x) \xrightarrow{FT} F(\omega,s) = \int\int f(x,t)exp(i\omega t - i\omega sx)dtdx \tag{3.1.6}$$

$$f(t,x) \xrightarrow{FT} F(f,s) = \int\int f(x,t)exp((i2\pi f)(t - sx))dtdx \tag{3.1.7}$$

When we take the Fourier transform in time of all the signals and keep only one frequency, all the traces become cosine functions, which is shown in Figure 3.1. Then we stack the cosine functions with different angles(slowness). The resulting stack is also a cosine function, but the amplitude will vary depending on what slowness you use. One column from a slowness-frequency spectrum represents the amplitude of the cosine function you get when stacking at different slowness. If the angle hits so that we get positive interference of all cosine functions, we get the maximum amplitude.

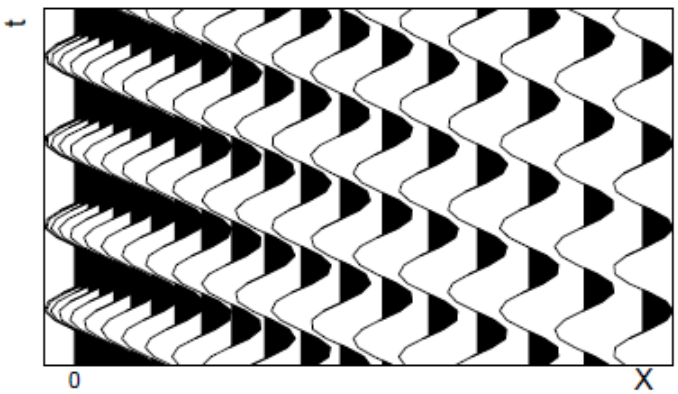

Figure 3.1: *Cosine functions with the same frequency modified from Schonewille and Duijndam (1997)*

3.2 Is there enough energy for an inversion?

Slowness-frequency spectra were produced to see if there was enough energy for an inversion. For this section eight or twelve hours of stacked cross correlations were used. Detrend, spectral whitening and a 10 Hz low pass filter was applied before carrying out the cross correlation. This was done for the all components and for different configurations.

Vertical component
For the vertical component slowness-frequency spectres are presented for the 4 lines shown in Figure 2.8 and for interstations across the system. When working with the lines, eight hours of data was used. For the interstations across the system, twelve hours of data was used. The results for line one is presented in Figure 3.2.

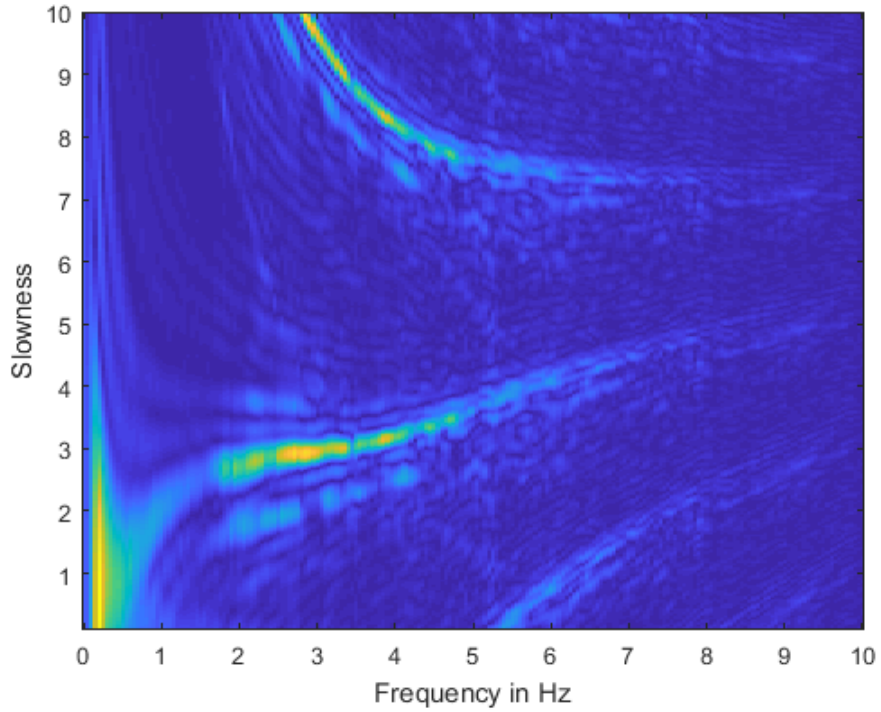

Figure 3.2: *Slowness-frequency spectrum for eight-hour stacked vertical component cross correlations along line one. The slowness is in s/km.*

Figure 3.2 shows the slowness-frequency spectrum for the vertical component line one. On the y-axis we have the slowness in s/km and on the x-axis we have the frequency in Hz. The image shows at what velocity the different frequencies of the wave travel and where we have energy. There is a relatively coherent curve found at slowness equal to 3 s/km and frequency equal to 3 Hz. You can follow the curve from just below 2 Hz to approximately 5 Hz. Just below this feature, at 2 s/km and 2 Hz, you can find another somewhat coherent line, with less energy than the previous. This could be an overtone.

There are two other features at higher slowness, which resemble the two previously described, and they could therefore be aliasing. Figure 3.2 also displays a strong vertical feature with a lot of energy at frequency equal to 0.15 Hz. Most of the energy seems to be below 5 Hz.

The curve dominating the image is the Scholte wave, which is an interface wave. A Scholte wave is basically a Rayleigh wave under water. The particle motion of a Rayleigh wave is an elliptical motion in the vertical plane with respect to the surface, and is therefore visible on the vertical component. The dispersion images from all 4 lines were very similar. The results are displayed in Figures 3.3, 3.4 and 3.5.

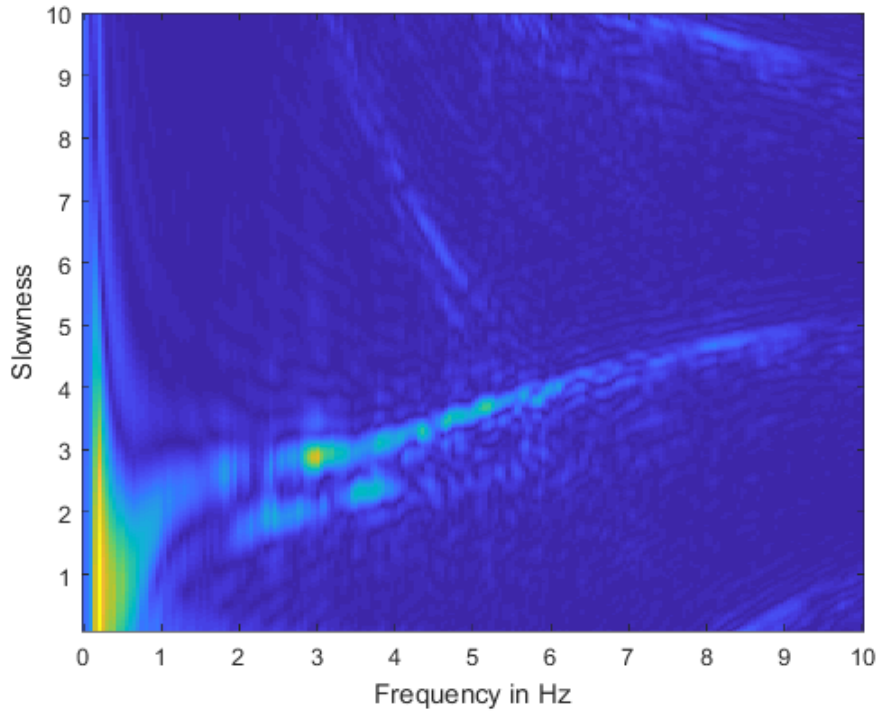

Figure 3.3: *The same as Figure 3.2 for line two. Line two yields very similar results to line one. The slowness is in s/km.*

Figure 3.3 and 3.4 are the dispersion images for line 2 and 3. The images for both lines are dominated by the Scholte wave dispersion curve at 3 s/km and 3 Hz, with a curve below, at 2 s/km and 2 Hz. This could be an overtone. The positions are almost the same as for line one (Figure 3.2). Both images also display a strong vertical feature at low frequency, and appear to have energy mainly up to 5 Hz. The results for line four are presented in Figure 3.5.

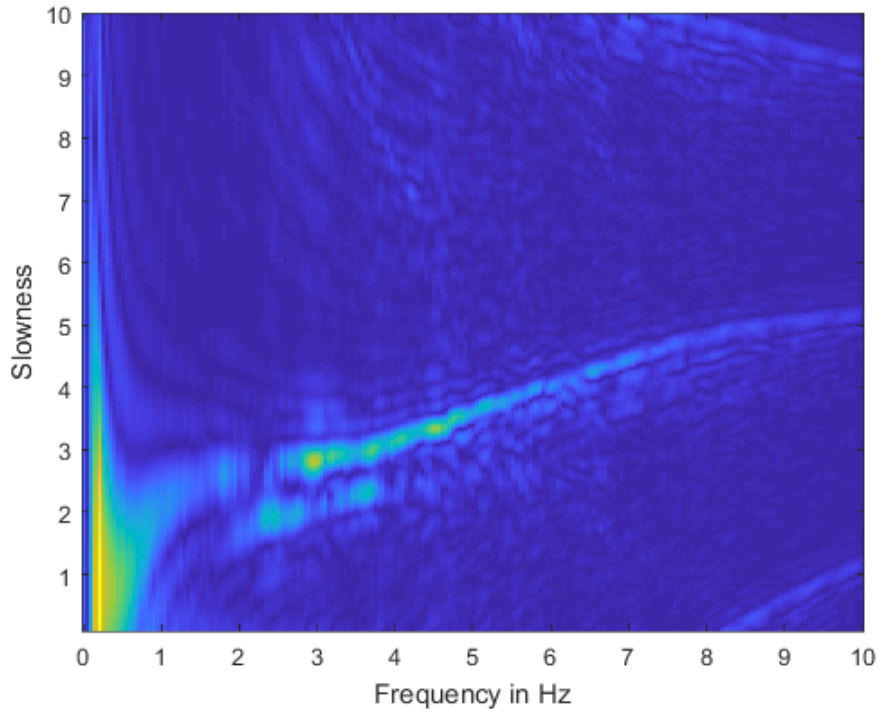

Figure 3.4: *Same as Figure 3.2 for line three. The slowness is in s/km.*

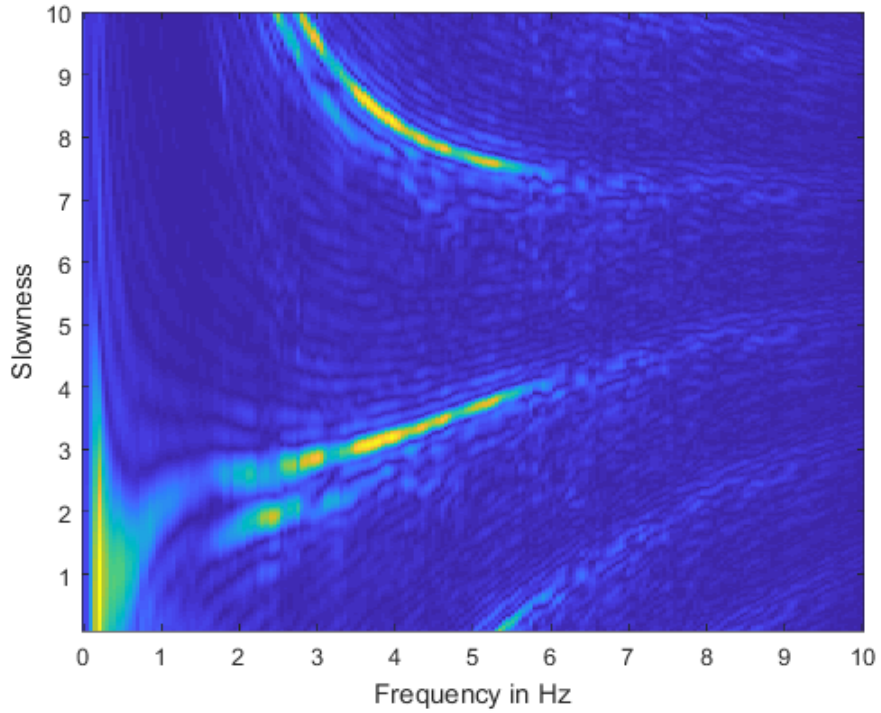

Figure 3.5: *Same as Figure 3.2 for line four. The slowness is in s/km.*

Figure 3.5 displays the slowness-frequency spectrum for the vertical component line four. Line four is similar to the other three lines, as it displays the same vertical low frequency feature at the same position as previously described. The dispersion image is dominated by the Scholte wave, and the curve below this prominent feature is also present for line four, and it actually more visible, has more energy, in this case than in the previous cases. As for line one, it also displays signs of aliasing.

All the lines display very similar results. For all lines we have a lot of energy at low frequencies, especially at around 0.15 Hz. The energy present at low frequencies corresponds well with the frequency range where we have natural noise (0.03-1 Hz). Here we have oceanic microseisms generated interaction between oceans and the solid Earth. Their noise sources are homogeneously distributed over the globe, which makes it suitable for interferometry. At higher frequencies, the seismic noise sources are often related to human activity. (Mordret et al., 2013) This could be the platform. To investigate this further, a slowness-frequency spectrum was also created for the interstations across the system, which is displayed in Figure 3.6.

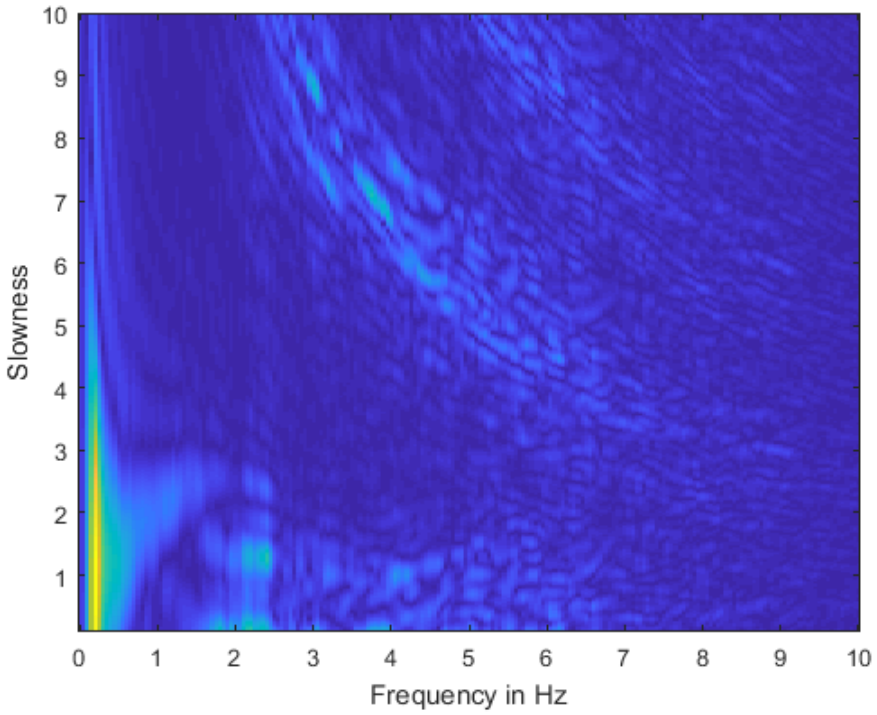

Figure 3.6: *Same as Figure 3.2 but for interstations from across the system and twelve hours are stacked. The slowness is in s/km.*

Figure 3.6 shows the dispersion image for the vertical component for interstations across the system. There is mainly energy up to about 2 Hz. At 0.15 Hz, there is a vertical high amplitude feature that dominates the image. There is also a vague curve that is found at 2 s/km and 1 Hz. Up to about 2 Hz, the dispersion image from the interstations

across the system similar to the ones that arise from the four lines. The image from the lines and across the system have the same strong vertical feature at low frequencies, and a curve at the same position, which could be the Scholte wave dispersion curve, though it is not very distinguished and is therefore difficult to use. Since the station pairs used across the system are not in line with the platform, noise coming from the platform would cancel out as it is not in the right azimuth. Because the noise above approximately 2 Hz is not visible for the interstations across the system, it supports that the noise above approximately 2 Hz originates from the platform.

Radial component

In the case of the radial component, the cross correlations along the the four lines were produced. Since the results from the lines were similar, only the results from line one are shown. The same processing as for the vertical component line one was carried out, and the results are displayed in Figure 3.7.

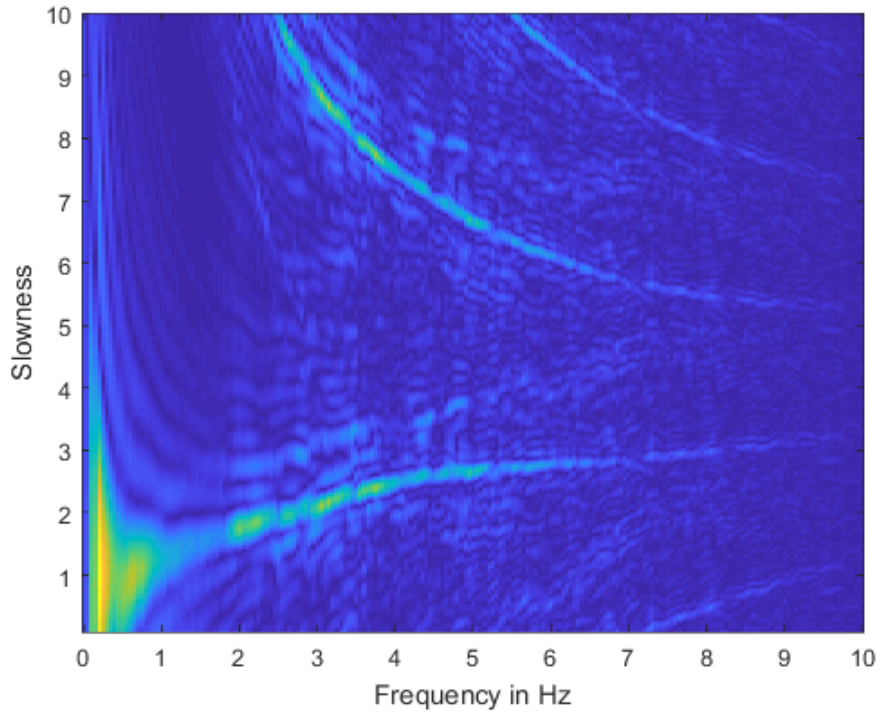

Figure 3.7: *Same as Figure 3.2 but for the radial component line one. The slowness is in s/km.*

The slowness-frequency spectrum for the radial component line one is shown in Figure 3.7. There is the most energy from about 0.15 Hz up to approximately 1 Hz. At 0.15 Hz there is also a strong vertical feature. The figure displays one prominent curve. The curve can be found at slowness 2 s/km and 2 Hz, and is strong up to about 5 Hz. There appears to be something going on above the curve as well.

Comparing the main curve found in Figure 3.7 to the results from the vertical component (Figure 3.2), the position is not the same as the main curve from the vertical component. It does, however, match well with the position of the lower curve. This curve was assumed to be an overtone. The upper, barely visible feature could be the main curve from the vertical component. This shows that the overtone is stronger than the fundamental mode on the radial component.

Transversal component
When producing slowness-frequency plots for the transverse component, the same procedure as for Figure 3.2 was utilized. The slowness-frequency spectra were created for all of the four lines, but only the results from configuration line one are shown, as the results were very similar. The results from the transversal component are shown in Figure 3.8.

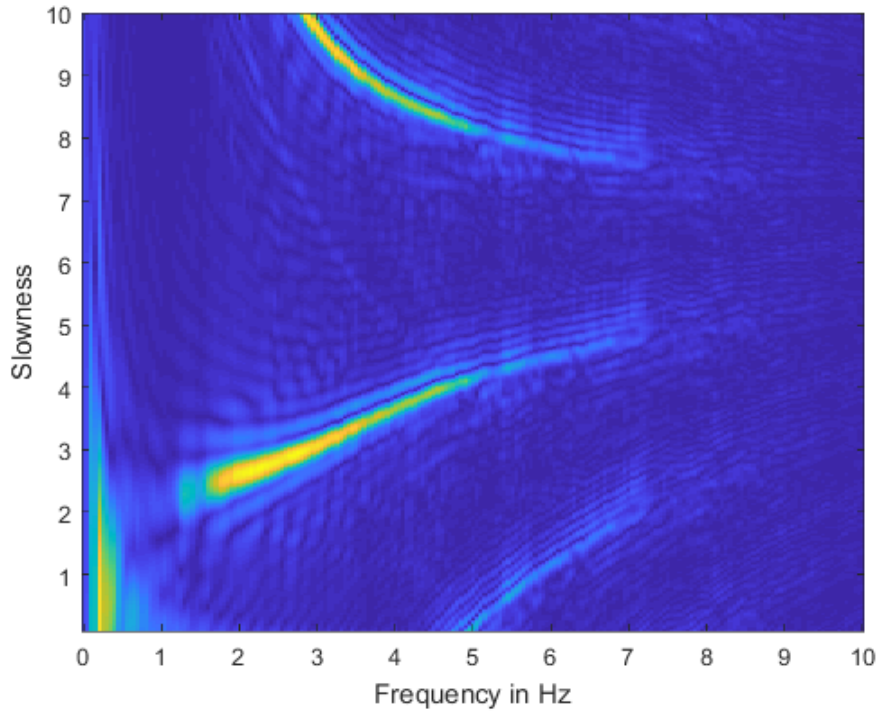

Figure 3.8: *Same as Figure 3.2 for the transversal component line one. The slowness is in s/km.*

Figure 3.8 shows the dispersion image for the transversal component line one. It is dominated by a sharp, coherent curve. The curve is strong from about 2 Hz up to 5 Hz. The dispersion curve was assumed to be the Love wave. The Love wave has particle movement perpendicular to the direction of propagation and parallel to the surface, and is therefore picked up by the transversal component. The feature is repeated for higher slowness, which could be aliasing. At low frequencies, about 0.15 Hz, there is a strong vertical feature.

From the transversal component, a different surface wave emerges than on the vertical and radial component. The curve is more sharp than the curves on the vertical and radial components, and it is also coherent. This makes it suitable for picking the dispersion curve. As all the previously described components it has a strong vertical feature at low frequency at approximately the same position.

Hydrophone component
The hydrophone data was also used to create slowness-frequency spectra. This was done the same way as for Figure 3.2. Only the results from line one are shown, as the lines yielded very similar results. The results are presented in Figure 3.9.

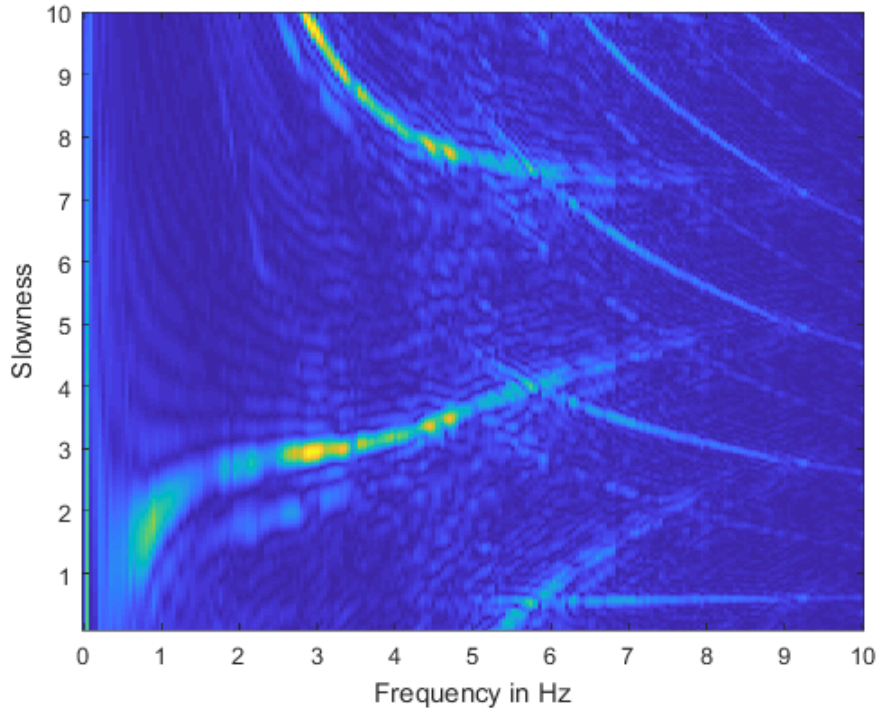

Figure 3.9: *The same as Figure 3.2 for the hydrophone component line one. The slowness is in s/km.*

The slowness-frequency spectrum from the hydrophone component line one is shown in Figure 3.9. Here we have one curve that is dominating the plot, which is found at 3 s/km and 3 Hz. This is again the Scholte wave. Below the dispersion curve for the Scholte wave there appears to be another curve. This can be found at 2 s/km and 2 Hz. This could be an overtone for the Scholte wave. The two features are repeated at 7-10 s/km, which could be aliasing. The hydrophones correspond to changes in water pressure.

A horizontal feature is present for higher frequencies, about 5-10 Hz and slowness about 0.5 s/km. This is possibly the wave travelling in water, since the slowness is constant, but the velocity seems a bit too high. There are eight other features that appear to mimic this feature, which could also be aliasing.

The hydrophone component does not have as much energy in the lower frequencies as the previous components. It displays a very similar dispersion curve and the same wave as the vertical component, and the also displays the less visible curve with the lower slowness as previously detected (Figure 3.2).

3.3 Causal and acausal part of the cross correlation

The transversal data (Figure 3.8) gives the most distinct dispersion curve. In this case the cross correlations only had an acausal part. When producing slowness-frequency spectrum, the acausal and causal part was added. Since we are using noise coming from the platform, the causal and acausal part of the correlation might give rise to different dispersion curves. This could affect the results when adding them together. The vertical component and the hydrophone displayed two different dispersion curves. To check if these curves arose from the different parts of the correlation, separate dispersion images were produced for the acausal and causal part. In this case a 4 Hz low pass filter was used, otherwise the same procedure was carried out as for Figure 3.2. The results presented are from the vertical component line one. Firstly the added slowness-frequency spectrum for the causal and acausal part is presented for comparison in Figure 3.10.

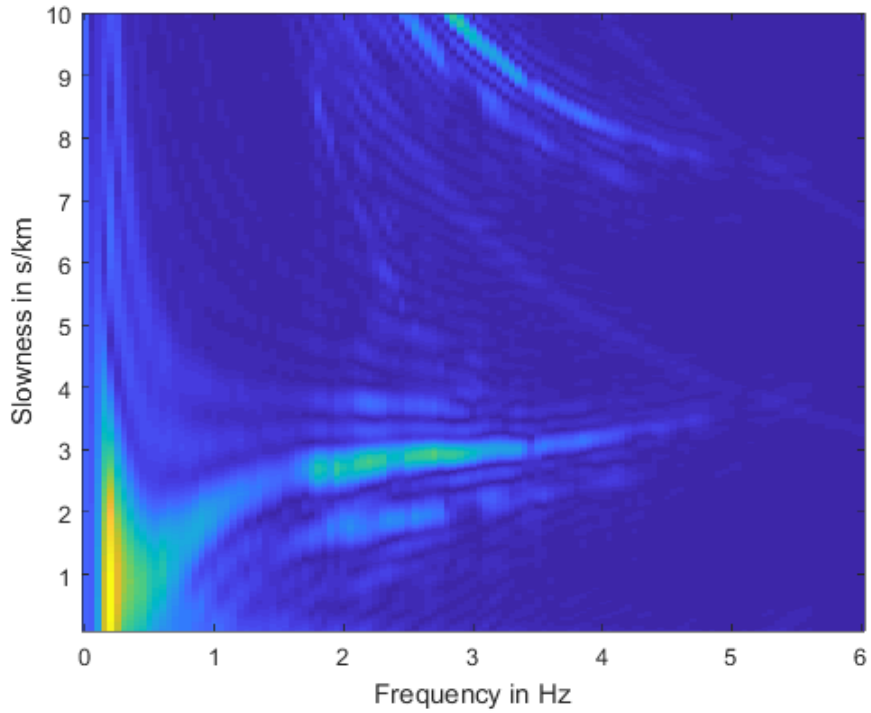

Figure 3.10: *Same as Figure 3.2 with a 4 Hz low pass filter vertical component line one. The causal and acausal part is added.*

In Figure 3.10 we see the dispersion image resulting from adding the acausal and causal part of the cross correlation. Here we have two distinct curves at 3 s/km and 3 Hz, while the other can be found at 2 s/km and 2 Hz. To see what curve or curves the causal part and the acausal part result in, the results for the causal part and the acausal part are presented separately in Figures 3.11 and 3.12 respectively.

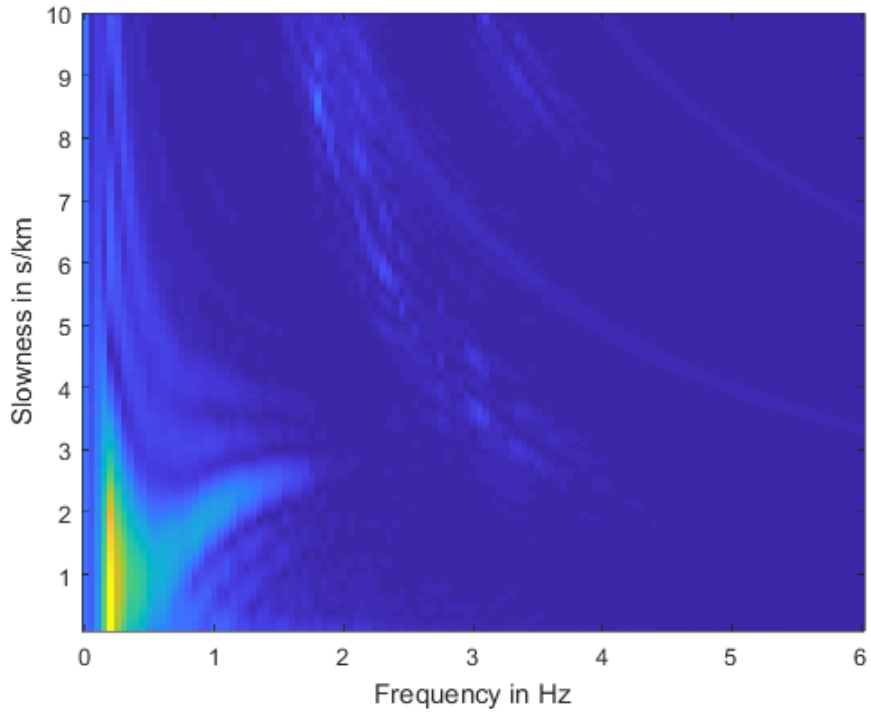

Figure 3.11: *The same as Figure 3.10 for the causal part.*

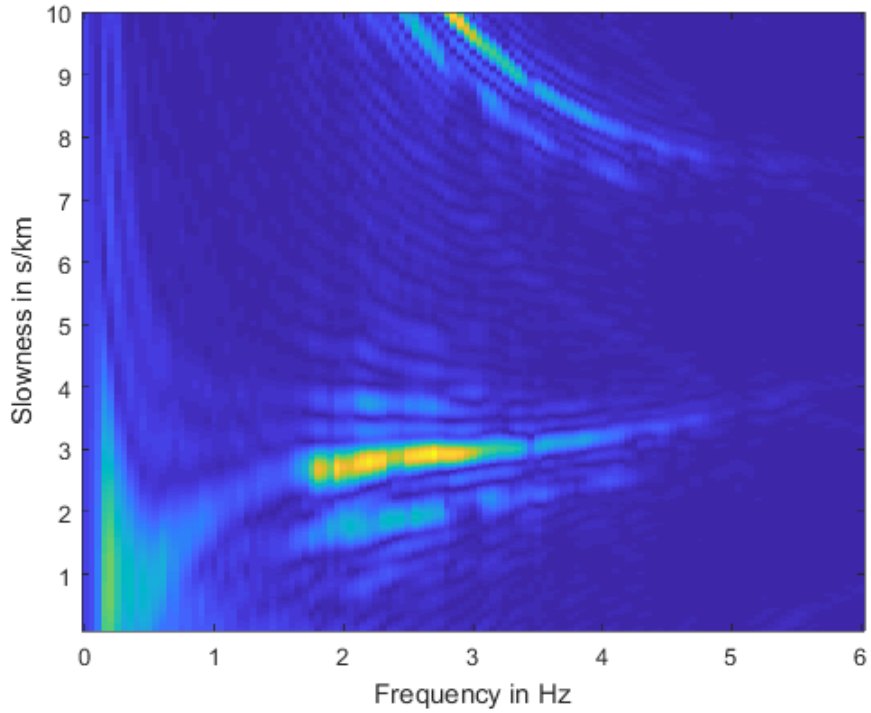

Figure 3.12: *Same as Figure 3.10 for the acausal part.*

Figure 3.11 shows the dispersion image from the causal part of the cross correlations from the vertical component line one. The causal part only has energy up to about 2 Hz. There is one dispersion curve, which can be found at 2 s/km and 1 Hz. This is the same curve as the upper dispersion curve from the added dispersion image shown in Figure 3.10. In Figure 3.12, which is the dispersion image for the acausal part of the same correlation, there are two dispersion curves. One is found at 2 s/km and 1 Hz, while the other is found at 2 s/km and 2 Hz. They also have the same positions as the curves observed in Figure 3.10.

Since the upper curve from the acausal dispersion image has the same position as the curve observed on the causal dispersion image, it means that the causal and acausal part do not give rise to different dispersion curves. This was also the case for the hydrophone component. Adding the causal and acausal part together should therefore not affect the results. This also supports the lower dispersion curve can be an overtone. The fact that the causal part only has energy up to 2 Hz and the acausal part has energy up to about 5 Hz, confirms that the higher frequencies are coming from the platform, and that the energy up to 2 Hz is coming from all directions.

3.4 Dispersion curve selection

Measuring the phase velocity dispersion curves is a fundamental requirement for surface wave methods. Phase velocity is the speed of each harmonic, while the group velocity is the speed of the wave packet. To retrieve the dispersion curves, slowness-frequency spectra where the energy was renormalized to its maximum per frequency were used. The normalization was used to make it easier to see where the maximum is located for different frequencies, and to see the dispersion curve. It was initially not used because we wanted to see where we had energy. When normalizing the maximum energy per frequency, the maximum energy per frequency is equal to one, and we lose the relationship between the energy content for each frequency.

Each column in the slowness-frequency spectrum at a given frequency shows the amplitude we get by stacking different slowness. Since the amplitude of the stack which corresponds to the correct slowness is enhanced, and the other slownesses are suppressed as they do not stack coherently, the dispersion curve can be picked by selecting the amplitude peaks that align along the dispersion curve. Therefore the maximum value was picked for different columns(frequencies) from the normalized slowness-frequency data, and the corresponding slowness was found. This was done in Matlab with the max-function.The maximum was found from 15 up to 20 frequency values. The minimum and maximum frequency used was 0.2 and 4 Hz. To make sure the correct dispersion curve was chosen, a reference line was made.

Dispersion curves for all components and all lines were found. Line two and three were processed together, since they displayed very similar results. The dispersion curve for the vertical component line one is displayed in Figure 3.13 and is plotted on top of the slowness-frequency spectrum with a trace normalization regarding frequency.

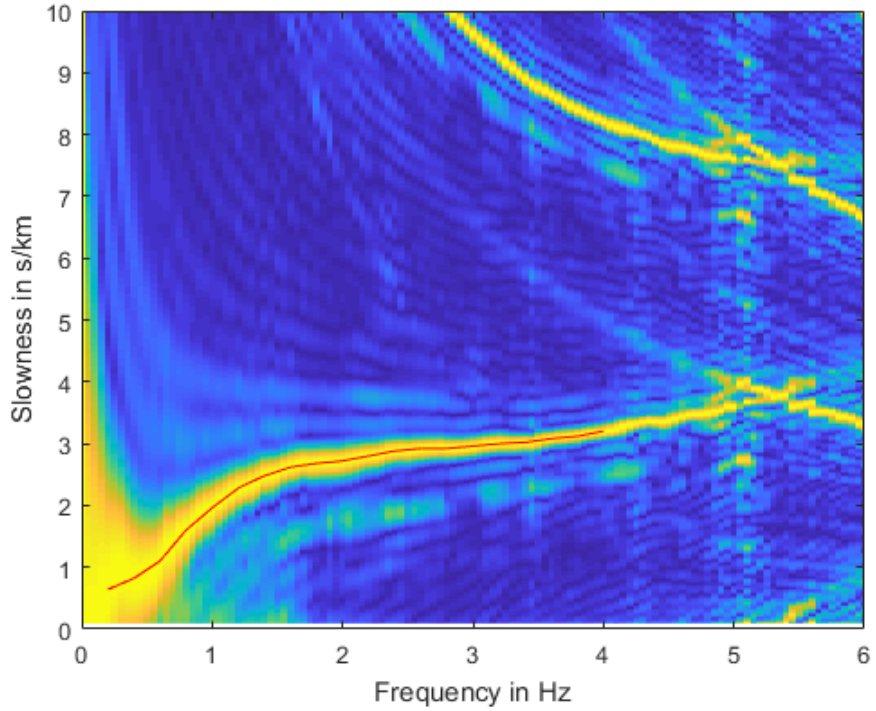

Figure 3.13: *The picked dispersion curve for the vertical component line one is plotted in red on top of the slowness-frequency spectrum. The spectrum has a trace-normalization regarding frequency.*

Figure 3.13 displays a coherent and continuous dispersion curve, which can be found at slowness equal to 3 s/km and frequency equal to 3 Hz. Below another feature is visible, but it is not as prominent. The picked dispersion curve for the vertical component line one is plotted in red on top of the slowness-frequency spectrum. The maximum always followed the same dispersion curve. It was difficult to decide whether to use the lower frequencies. It was therefore decided to exclude the frequencies where the dispersion curve had a drastic increase or decrease. This was also followed for the other components. It was also decided to pick from frequencies up to 4 Hz, as a 4 Hz low pass filter was used and the results from the band-pass test (Figure 2.30).

Picking the velocity for line one was very straight forward for all components, as the maximum value followed the same curve. This was not always the case. For example, when looking at the vertical component for lines two and three (Figure 3.14) we see two disjoint curves, and the maximum jumps between them. This resulted in gaps along the Scholte wave dispersion curve. A maximum was not chosen for the frequencies with gaps.

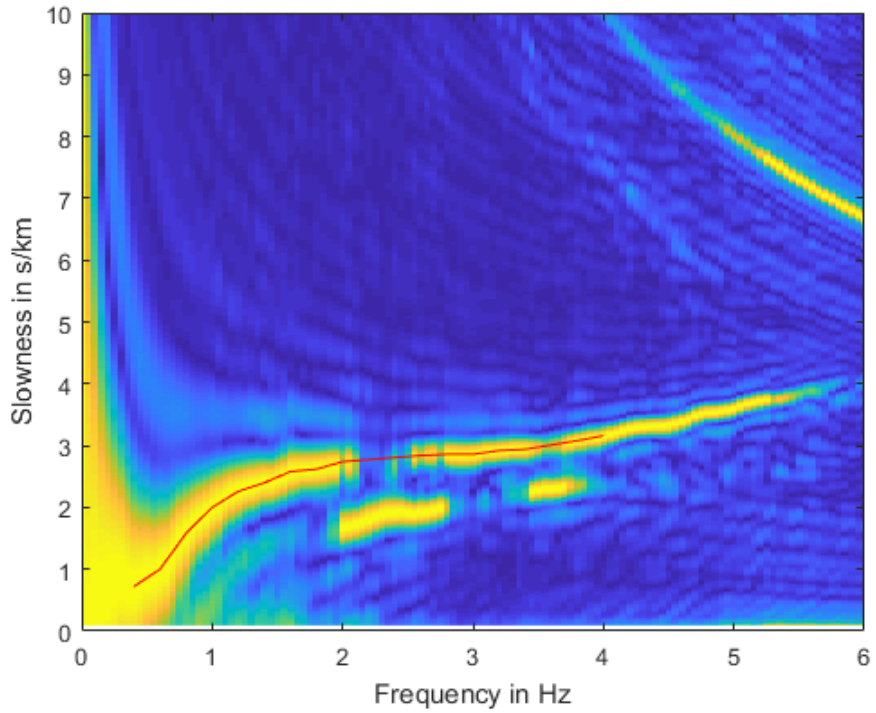

Figure 3.14: *Same as Figure 3.13 but for the vertical component line two and three.*

Examples of picked dispersion curves for the transversal, radial and hydrophone component line one are presented in Figures 3.15, 3.16 and 3.17 respectively.

The selection of the dispersion curve for the transversal component was straight forward, as it only had one dispersion curve. Looking at the results from the transversal component line one (Figure 3.15) the dispersion curve begins at a higher frequency than the other components. The picking started at 1.2 Hz.

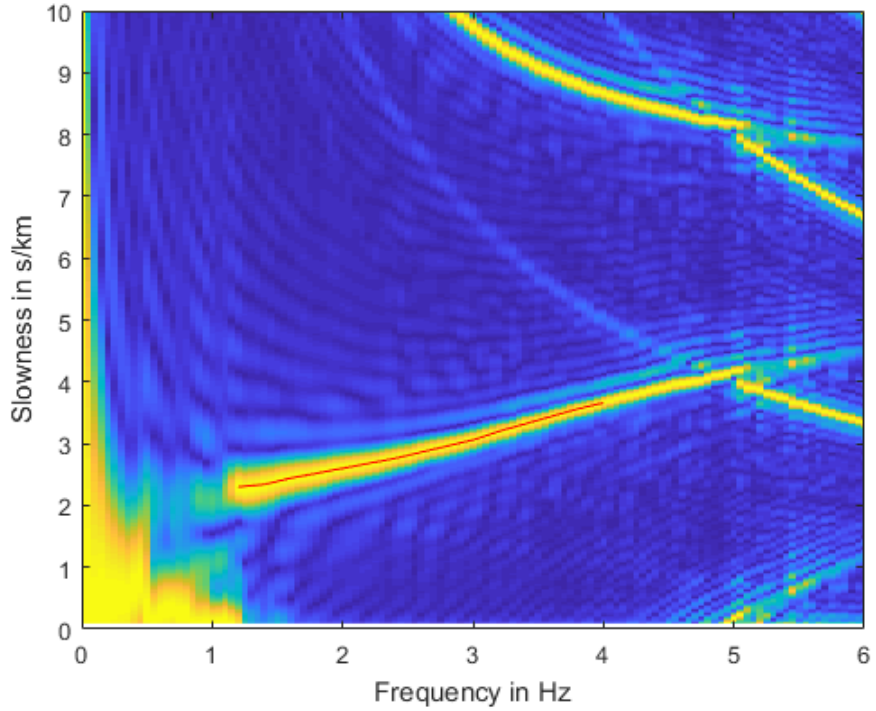

Figure 3.15: *Same as Figure 3.13 for the transversal component line one.*

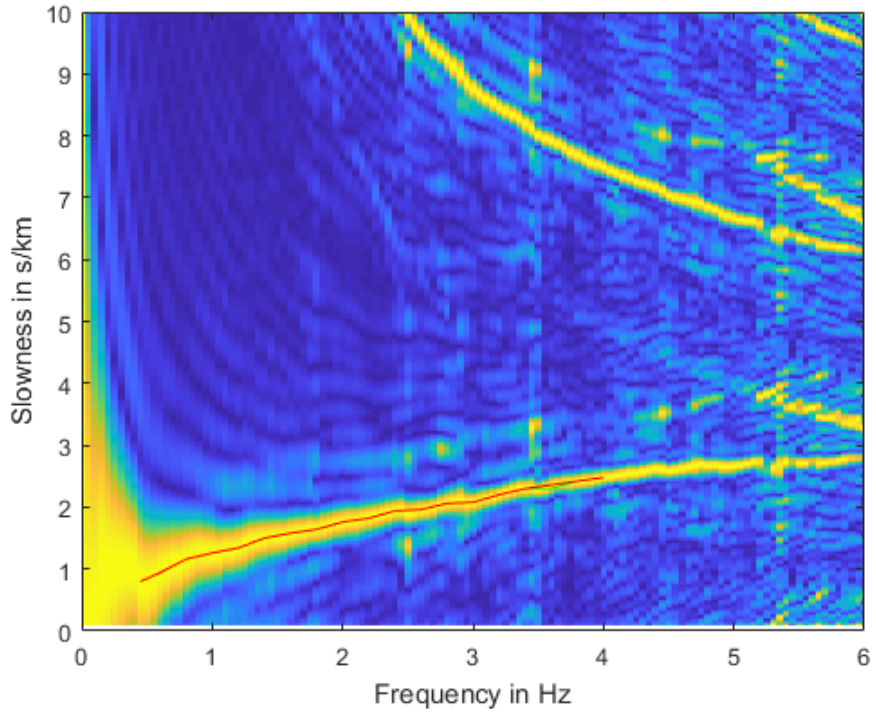

Figure 3.16: *Same as Figure 3.13 for the radial component line one.*

The results from the radial component with a normalized frequency (Figure 3.16) displays one strong and coherent curve, which can be found at slowness 2 s/km and frequency 2 Hz. This is the same location as the lower curve from the vertical component. This was suspected in both cases suspected to be an overtone. It is difficult to pick the overtone from the vertical component (Figure 3.13, Figure 3.14) since it could be contaminated by the other curve. On the radial component, however, there is only one curve. If this is an overtone, it can be picked more accurately from the radial component.

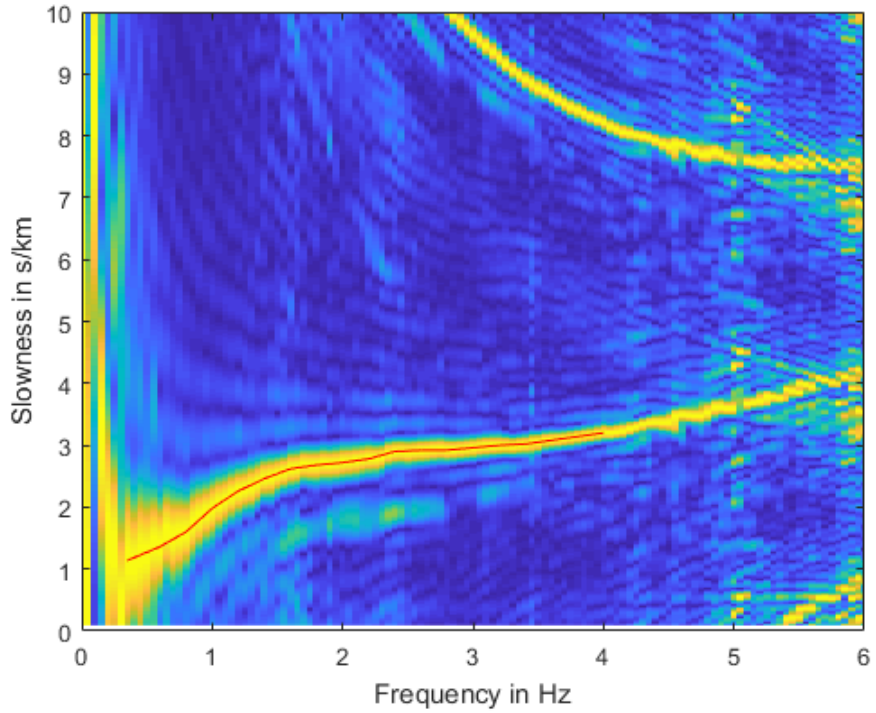

Figure 3.17: *Same as Figure 3.13 for the hydrophone component line one.*

The picked dispersion curve from the hydrophone component line one is shown in Figure 3.17. The picked dispersion curve appears to be very similar to the one from the vertical component line one (Figure 3.13). To compare the picked dispersion curves for all components and lines, all components and lines are presented in Figure 3.18.

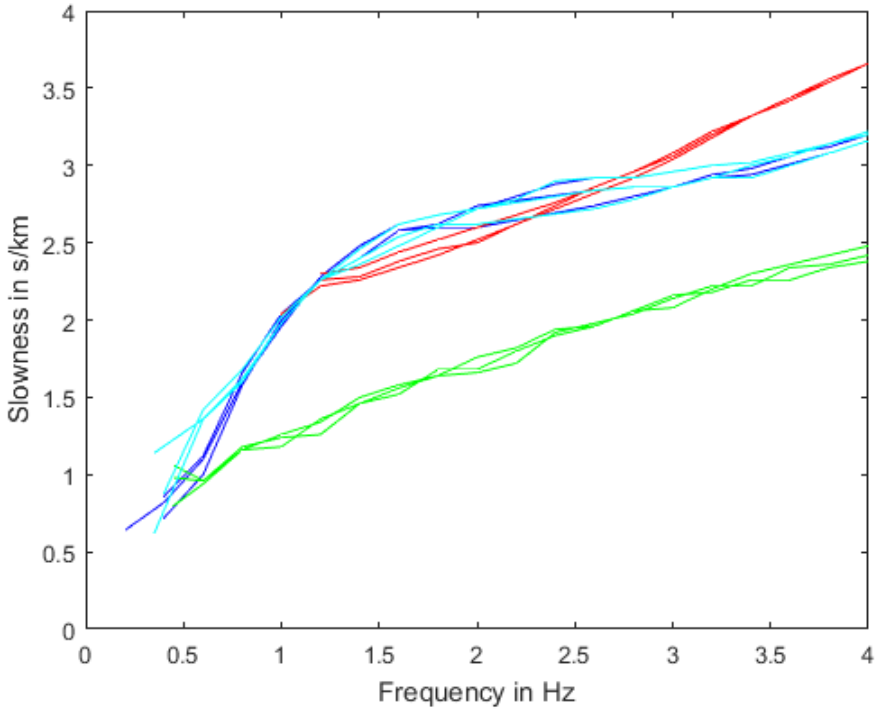

Figure 3.18: *The selected dispersion curves for all components and all lines are plotted together. The lines from the vertical component are plotted in blue, the transversal in red, radial in green and hydrophone in cyan.*

Figure 3.18 shows the selected dispersion curves from one component in the same color. The results from the vertical component are plotted in blue, the transversal component in red, the radial component in green and the hydrophone in cyan. The Scholte wave is retrieved from the vertical and the hydrophone component. The Scholte waves from different lines and different components match up nicely. From the transversal component we get the Love wave, and the dispersion curves from the different lines are very similar. We can also see that the Love wave crosses the Scholte wave. The dispersion curves from the radial component also match very well, and could be a higher mode.

3.5 Discussion and concluding remarks on slowness-frequency analysis

From the dispersion images we find that there is enough energy to do an inversion for frequencies at least up to 4 Hz in the case of the four lines pointing towards the platform. There is no major change with position. Adding the causal and acausal part of the cross correlations when producing the slowness-frequency spectrum did not affect the results even though the correlations are asymmetric. It is confirmed that up to 2 Hz we have natural noise, coming from all directions, and the higher frequency noise is coming from the platform. The Love wave and the Scholte wave emerge from the cross correlations of

ambient noise. The dispersion curve for the Scholte wave was picked from the vertical and the hydrophone component data, and the dispersion curve of the possible overtone picked on the radial component. The Love wave dispersion curve was retrieved from the transversal component.

Chapter 4

Depth inversion

Once the dispersion curves have been retrieved, they have to be interpreted with regards to the structure of the subsurface. This technique is called depth inversion. Tomography is a class of inversion. The only difference between surface wave tomography and ambient noise tomography is that the dispersion curves are measured from the noise correlations. Surface wave velocities are mostly sensitive to the shear wave velocity structure in the structure, and a depth inversion will therefore mainly give us a profile with depth of the shear wave velocity.

To do the inversion, two Fortran programs were used. One program was used to calculate the theoretical dispersion and eigenfunctions, written by Saito at the University of Tokyo. The theory is based on Takeuchi and Saito (1972) and Saito (1988). The other program was used to perform the inversion by Jean-Jacques Lévêque and Valerie Maupin at the University of Strasbourg. The theory behind the inversion is based on Tarantola and Valette (1982), and the program is used in Lévěque et al. (1991) and Maupin and Cara (1992).

4.1 Relation between velocity and subsurface properties

The simplest structure in which a surface wave can propagate is a homogeneous half-space, which supports only Rayleigh wave fundamental mode. In the half-space, there is no vertical variation in the structure. Therefore there is no dispersion, and consequently the phase and group velocities are the same, and can be calculated analytically. The velocity mainly depends on the shear wave structure, and only partly on the P-wave velocity and density. For standard Poisson's ratio, the phase and group velocities are equal to about 0.92 times the shear wave velocity in the half-space. For structures varying with depth, the phase velocity follows a similar relation, but using the shear wave velocity at a depth equal to about one third of the wavelength of the Rayleigh wave. Turning this relation around, this assumption is a good starting point for an inversion.

Theoretical phase velocities can be calculated for any kind of layering, a series of homogeneous layers or for structures with continuous variation with depth. A numerical integration of the elastic wave equation is what is used for structures with continuous changes with depth. It can also be used for Love waves and overtones. (Takeuchi and Saito, 1972)

4.2 The inverse problem

To perform the inversion, a linear approach was used to invert for the structure with depth. Linear inversion is suitable when you have little variation in S-wave velocity, and continuous variation with depth. The principle of linear inversion is to start with an initial model, with information you have from before the inversion. Then calculate theoretical phase velocity and the derivatives of the velocities with respect to different parameters, essentially the shear velocity with depth, and use the difference between the velocities in the initial model and the data, and the theoretical dispersion curves and derivatives to improve the model.

To go from the data to model parameters. We do this by assuming we know the physics behind a process which, for a set of model parameters described by a vector (m), gives rise to a set of observed data described by a vector (d). The data can then be looked as as a result of an operator (G) acting on the model parameters. Therefore, to do inversion, we have to solve an inverse problem where the observed data is related to the velocity structure or the model with the relation

$$d = Gm \tag{4.2.1}$$

To find out what gave rise to the specific set of observed data, we assume that some physical model describes the process, and then use the data to estimate a set of model parameters that are consistent with the data. The inverse problem can be solved either by finding m directly from d through mathematical inverse techniques, or through trial-and-error techniques, where the forward problem is solved multiple times and we look for the best solution. Inverse problems do often not have a unique or exact solutions. There is no model that can fully satisfy the data. This is because the data is inconsistent due to errors and because the models are a simplification. (Stein and Wysession, 2003) Therefore we find m_f such that

$$d_f = Gm_f \tag{4.2.2}$$

for making $\sum(d_f - d)^2$ as small as possible. This is equivalent to

$$G^T d = G^T G m_f \tag{4.2.3}$$

$$(G^T G)^{-1} G^T d = m_f \tag{4.2.4}$$

If we want to weight the data such that $\sum(\frac{d_f-d}{\sigma_d})^2$ is minimized, we introduce a matrix C_d

$$C_d = \begin{bmatrix} \sigma_1^2 & & \\ & \ddots & \\ & & \sigma_n^2 \end{bmatrix} \tag{4.2.5}$$

where σ is the standard deviation of the data. Including this in the equation yields

$$(G^T C_d^{-1} G)^{-1} G^T C_d^{-1} d = m_f \tag{4.2.6}$$

We introduce a damping function C_{m0}.

$$(G^T C_d^{-1} G + C_{m0}^{-1})^{-1} G^T C_d^{-1} d = m_f \tag{4.2.7}$$

for when $\sum(\frac{d_f-d}{\sigma_d})^2 + \sum(\frac{m_f-m_i}{\sigma_{mi}})^2$ and C_{m0} is

$$C_{m0} = \begin{bmatrix} \sigma_{m_1}^2 & \ddots & \ddots \\ \ddots & \ddots & \ddots \\ \ddots & \ddots & \sigma_{m_n}^2 \end{bmatrix} \tag{4.2.8}$$

When the data has a small standard deviation, the inversion relies on the data. If the data has a large standard deviation, the inversion relies on the information from before, which is called an a priori model.

4.3 A priori model

There are many different ways to do inversion, ranging to very simple to computationally demanding ones. Which one you choose depends on the precision of the measurements, the precision needed for the model and type of structure. In this case we assume that we have a smooth model with good a priori information.

The a priori model is the starting point for the inversion. The model included estimates of shear wave velocity, pressure wave velocity, density and depth, and was created from the values obtained in the slowness frequency chapter for the vertical data, line one. The shear wave velocity was estimated from the Rayleigh wave phase velocity by using the relation between the velocity in the half-space in case of standard Poisson ratio. When using this assumption, the velocity of the shear wave (v_s) is approximately the Rayleigh wave phase velocity ($v_{Rayleigh}$) divided by 0.92. (Maupin, 2016)

$$v_S = v_{Rayleigh}/0.92 \tag{4.3.1}$$

and the velocity was affected to a depth(Z) given by one-third of the Rayleigh wavelength($\lambda_{Rayleigh}$):

$$Z = \frac{1}{3}\lambda_{Rayleigh} \tag{4.3.2}$$

The pressure wave velocity (v_P) was found from the shear wave velocity through a relation between shear wave and pressure wave velocity from Castagna et al. (1985).

$$v_P = 1.16v_S + 1.36 \tag{4.3.3}$$

which makes up the mudrock line.

Gardner's rule (Brocher, 2005), which is derived for sedimentary rocks and is valid for $1.5 < v_P < 6.1$ km/sec was used to find the density (ρ) using the P-wave velocity:

$$\rho(g/cm^3) = 1.74 \times v_P^{0.25} \tag{4.3.4}$$

Figure 4.1 shows the resulting initial model.

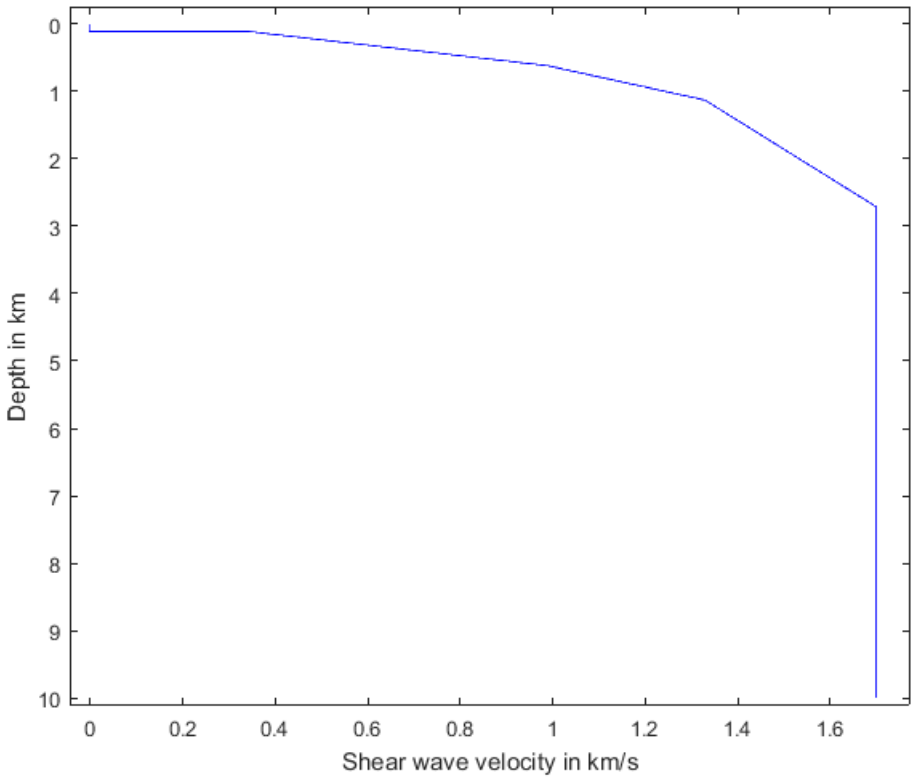

Figure 4.1: *Initial model used for inversion. It is a model of the shear wave velocity with depth built from a priori information. The first part is the water layer, where the shear wave velocity is equal to zero. The velocity increases with depth.*

Figure 4.1 shows the starting point for the inversion. The model has depth in km on the y-axis and shear wave velocity on the x-axis. The first part is the water layer, where the shear wave velocity is equal to zero. After the waterlayer the velocity increases gradually with depth. Below about 3 km we did not have any a priori information, so the last point

we had information was used from this point down to 10 km. The initial model is used to calculate theoretical dispersion curves.

4.4 Inverted models

Data
The inversion was done separately for the two longer lines of the array, and for the shorter lines combined. The vertical and hydrophone component were used to invert the Scholte wave dispersion.

The data that was put into the program included twelve periods with corresponding picked velocities and standard deviations. The standard deviations were found from the dispersion images and was chosen as the largest deviation from the picked slowness where the amplitude was approximately 0.9, shown in Figure 4.2. The standard deviation is larger for lower frequencies.

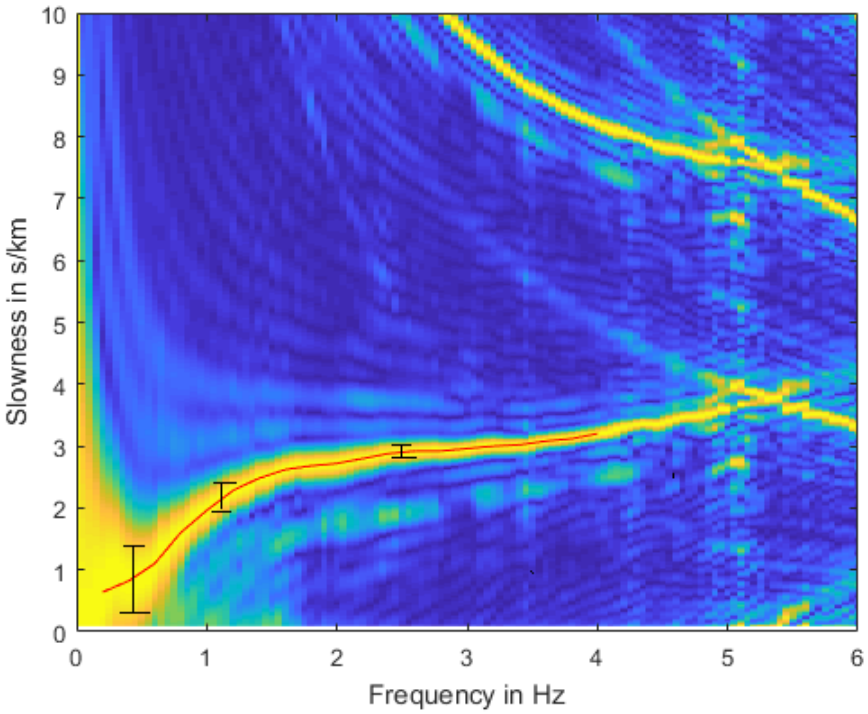

Figure 4.2: *An example of how the standard deviation of the picked dispersion curve was found from slowness-frequency spectra. The standard deviation is smaller for higher frequencies.*

A priori information covariance
The covariance of the a priori model (σ_m) expresses how much we will allow the inverted model to deviate from the a priori model during the inversion. We used a σ_m of 20 percent to allow rather large variation. This value is the same for all depths. This is not the case for the correlation length. The correlation length(l) is a way to express how homogeneous the subsurface is, and was put into the program. The points that are close to each other in depth are likely to have similar velocities. By choosing the correlation length you choose how far the points should be separated before their velocities are not correlated. The correlation length was given as:

$$l = a + bz \tag{4.4.1}$$

where a was the correlation length at surface and b the linear coefficient for depth increase. The correlation length at the surface was chosen as 0.1 km. This value was not changed, but it was tested for different values for the linear coefficient. A small correlation length is used when we want a detailed model, and would typically result in large standard deviations on the model. A large correlation length is used when we want an average, and would typically yield smaller standard deviations. We used 0.2 as b. It was also tested for different correlation lengths, which can be found in the Appendix.

Inverted models
Inverted models of shear wave velocity with depth were created from the Scholte wave. The Scholte wave was found on the vertical and hydrophone component. The two shorter lines of the array were processed together. Both the inverted model for the vertical component line one and the initial model is presented in Figures 4.3, and the corresponding misfit in 4.4.

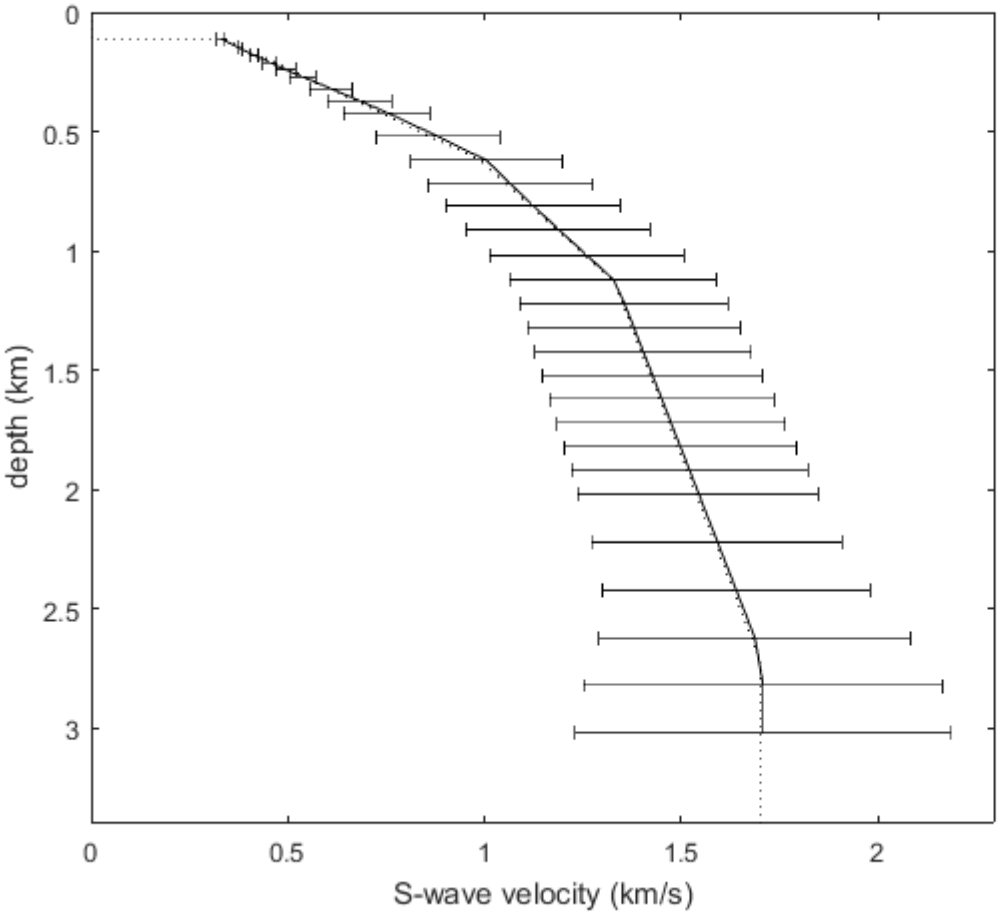

Figure 4.3: *Model of S-wave velocity with depth. The initial model is plotted together with the inverted model from the vertical component line one. The dotted line represents the initial model, while the solid represents the inverted model. The vertical lines are error bars.*

Figure 4.3 shows the shear wave velocity model as a function of depth made from the data from the vertical component line one in a solid line. The initial model is plotted with a dotted line. We have the shear wave velocity on the x-axis and the depth on the y-axis. The shear wave velocity increases gradually with depth. The inverted model is very close to the initial model, which suggests that the assumption made for the relation between shear wave velocity and Rayleigh wave velocity is good. The error increases with depth and gets very large. The corresponding misfit is presented in Figure 4.4.

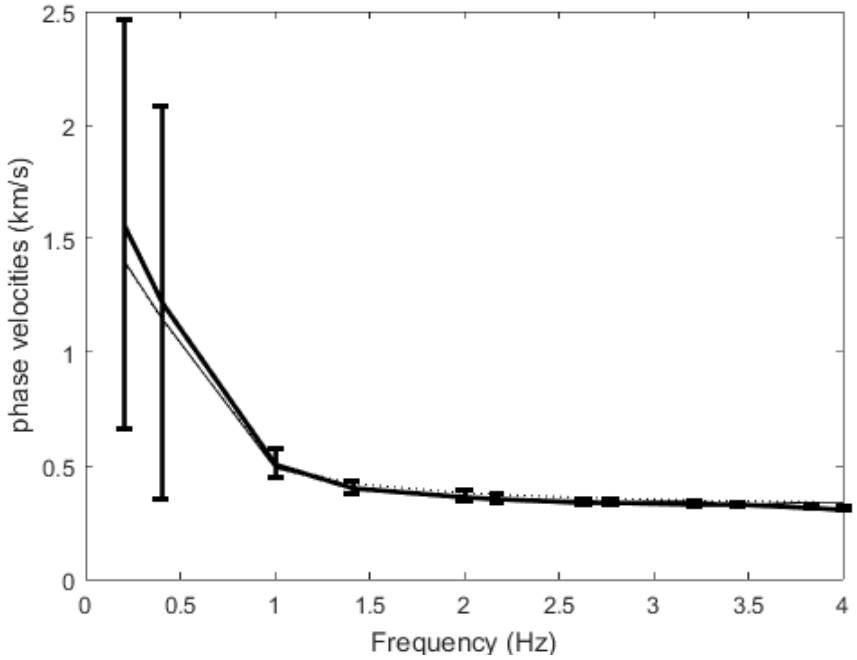

Figure 4.4: *Misfit for the vertical component line one. Shows the initial model with a dotted line, the data in a solid line with standard deviations and the final model with a solid line.*

The misfit from the vertical component line one is presented in Figure 4.4, with the phase velocity on the y-axis as a function of frequency. The initial model is plotted with a dotted line, the actual data in a solid line with error bars, and the final model with another solid line. The misfit shows how much work the inversion did on the data. There is very little difference between the initial model and the final model. The data fits very well for the higher frequencies and not as well for the lower frequencies. The error gets very large for the lower frequencies. We see that when the error on the data is large, the final model follows the initial model instead of the data. For shorter periods, where we have small errors, the final model is closer to the data than the initial model. Since there is very little difference between the initial model and the final model, the inversion has not done a lot changes.

All the inverted models were very similar. Inverted models for the vertical and hydrophone data line one, two and three, and four are shown in Figure 4.5, with the respective misfit in Figure 4.6.

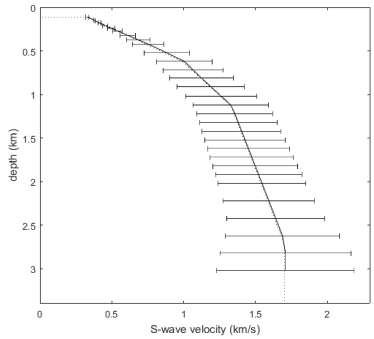

(a) *Vertical component line one*

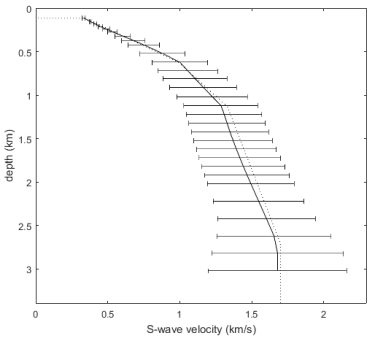

(b) *Hydrophone component line one*

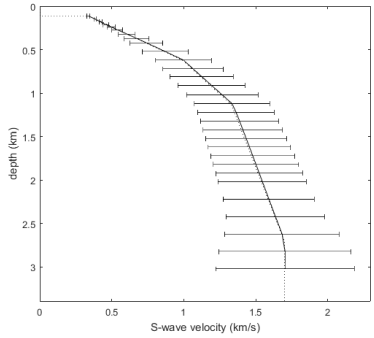

(c) *Vertical component line two and three*

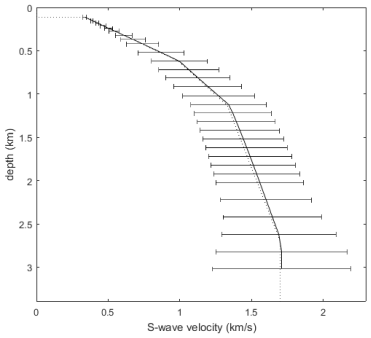

(d) *Hydrophone component line two and three*

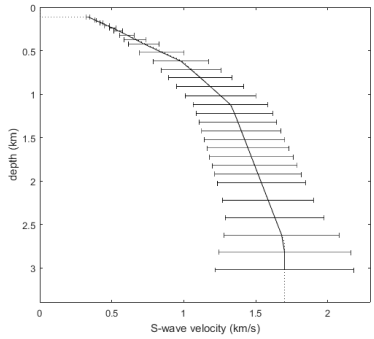

(e) *Vertical component line four*

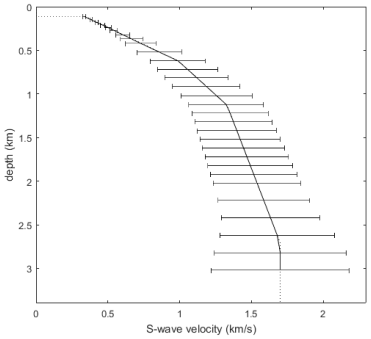

(f) *Hydrophone component line four*

Figure 4.5: *Shear wave model for the vertical and hydrophone component for all lines.*

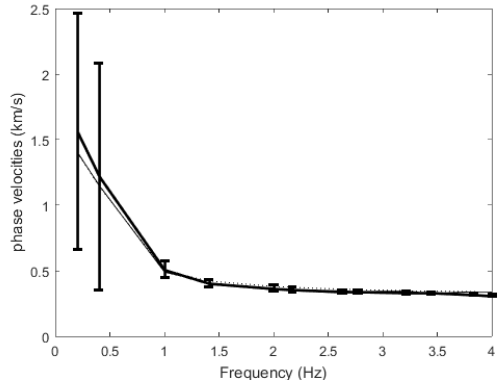

(a) *Vertical component line one*

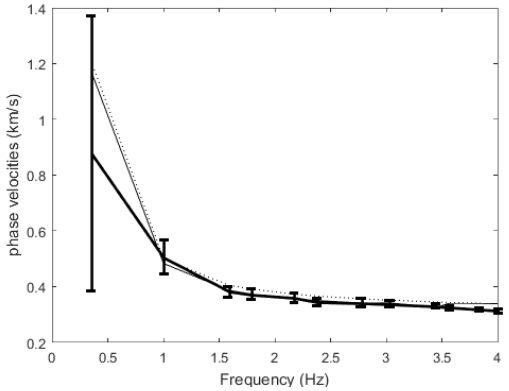

(b) *Hydrophone component line one*

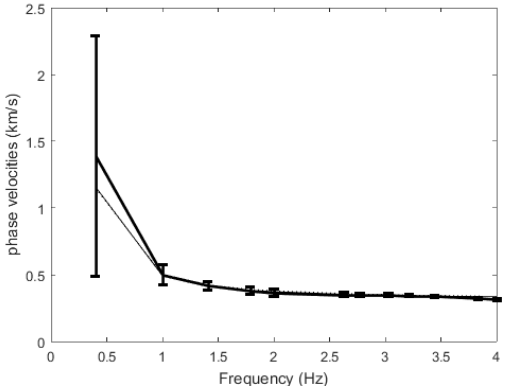

(c) *Vertical component line two and three*

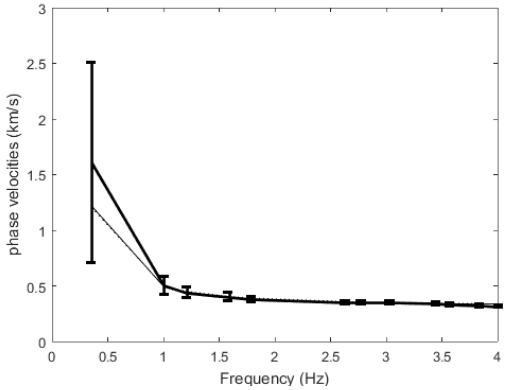

(d) *Hydrophone component line two and three*

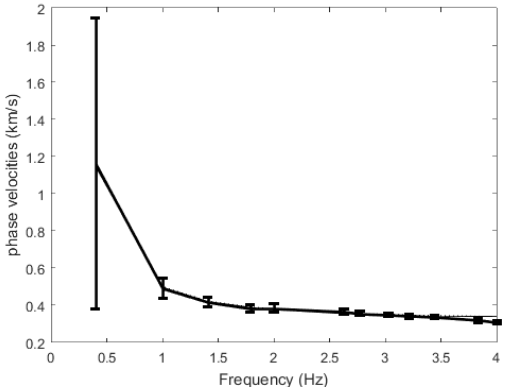

(e) *Vertical component line four*

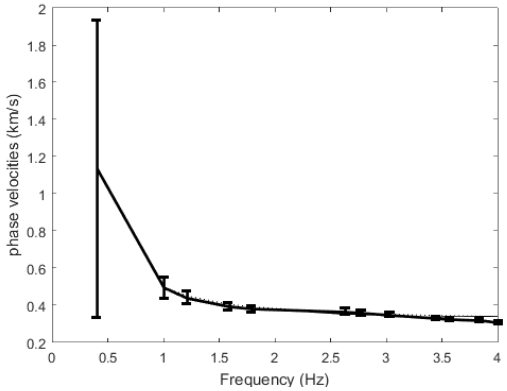

(f) *Hydrophone component line four*

Figure 4.6: *Misfit for the vertical and hydrophone component for the different lines.*

Figure 4.6 shows the misfit for the vertical and hydrophone component for all of the lines. The results show that the inversion yielded very similar results as the shear wave and Rayleigh wave phase velocity relation used in the initial model. Therefore the linear inversion has not improved the initial model very much.

Since we see that the initial model is a good estimate for the shear wave velocity, we can use this to calculate theoretical dispersion curves for the Love wave and the Scholte wave overtone.

4.5 Theoretical dispersion curves

The theoretical dispersion curves were calculated by a numerical integration of the elastic wave equation from the initial model for selected periods. This was done for the Rayleigh wave, the Love wave and what was suspected to be an overtone. The theoretical dispersion curve for the Love wave line one is presented in Figure 4.7

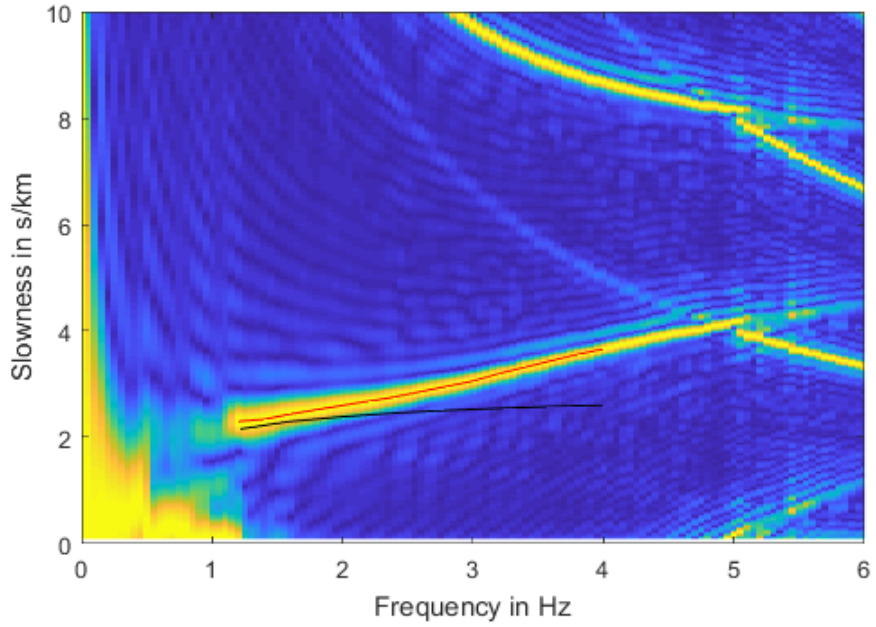

Figure 4.7: *Theoretical(black) and picked(red) Love wave dispersion from the transversal component line one. The curves start at about the same point, but deviate for higher frequencies.*

Figure 4.7 shows the slowness-frequency spectrum for the transversal component with the picked and theoretical dispersion curve in red and black respectively. The curves begin at almost the same position, but the theoretical curve does not increase with frequency as much as the actual data.

In the previous sections a curve was observed below the picked dispersion curve on the vertical and hydrophone data, which could be an overtone. To figure out whether it was an overtone or not, the theoretical curve was compared to the actual data, as shown in Figure 4.8 and 4.9.

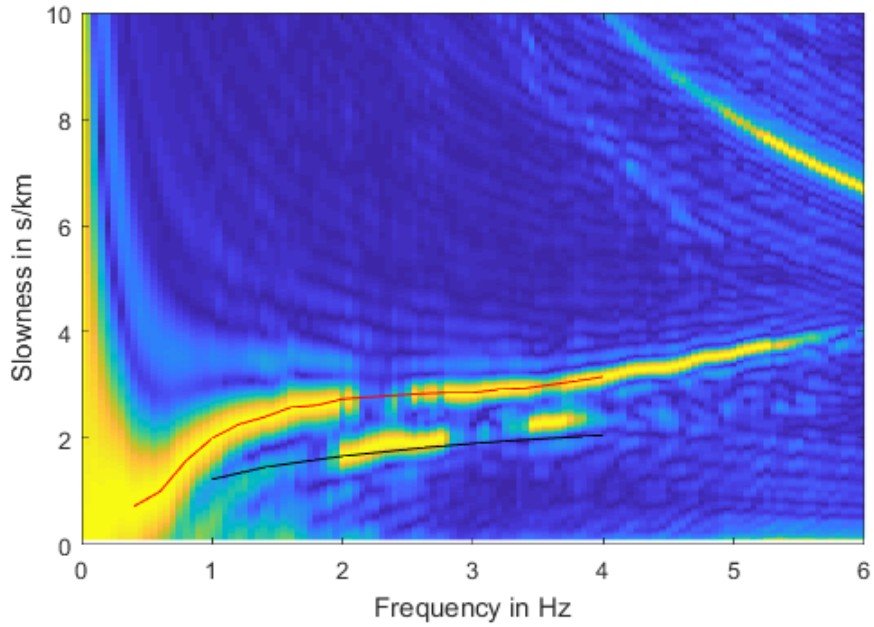

Figure 4.8: *Overtone vertical component line two and three. The picked dispersion curve is plotted in red, while the overtone is in black. The overtone matches particularly well with the lower feature around 2 Hz, and deviates slightly for higher and lower frequencies.*

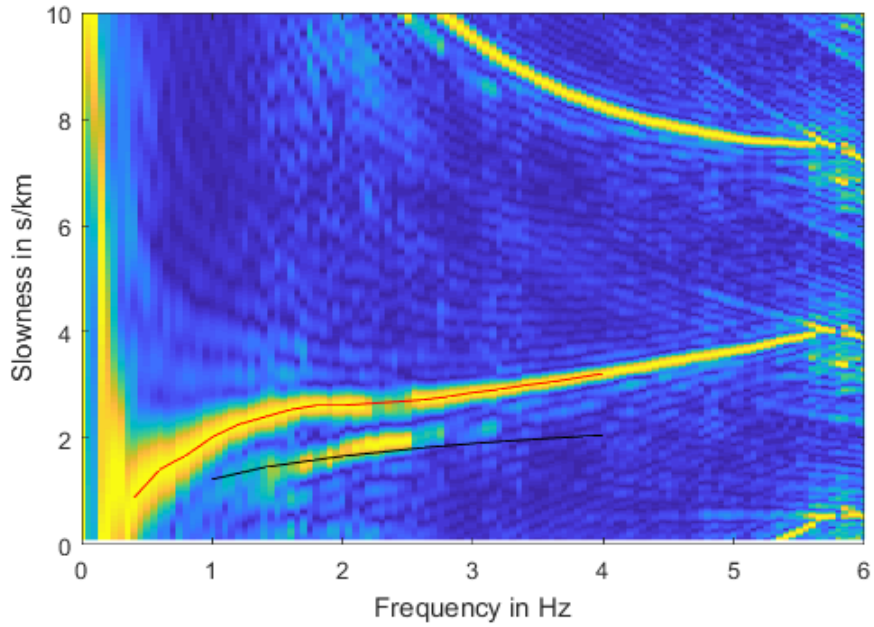

Figure 4.9: *Overtone on the hydrophone component line four. The first overtone is plotted in black while the picked dispersion is plotted in red. The overtone matches well with the feature below the picked dispersion for lower frequencies, and deviate more for higher.*

Figure 4.8 shows the data from the vertical component line two and three with the picked dispersion curve for the fundamental mode in red and the theoretical dispersion curve for the overtone in black. The curve matches fairly well with the data, but is at slightly lower slowness. The theoretical curve for the overtone on the hydropone component line one are presented in Figure 4.9. The theoretical dispersion curve matches fairly well in this case as well, and is slightly lower than the actual data. The dispersion curve is difficult to pick from the hydrophone and the vertical component because it is not coherent, and can also be contaminated by the dispersion curve for the fundamental mode. On the radial component only one dispersion curve was observed, with the same position as the overtone. Therefore, the data from the radial component was also compared to the theoretical overtone in Figure 4.10.

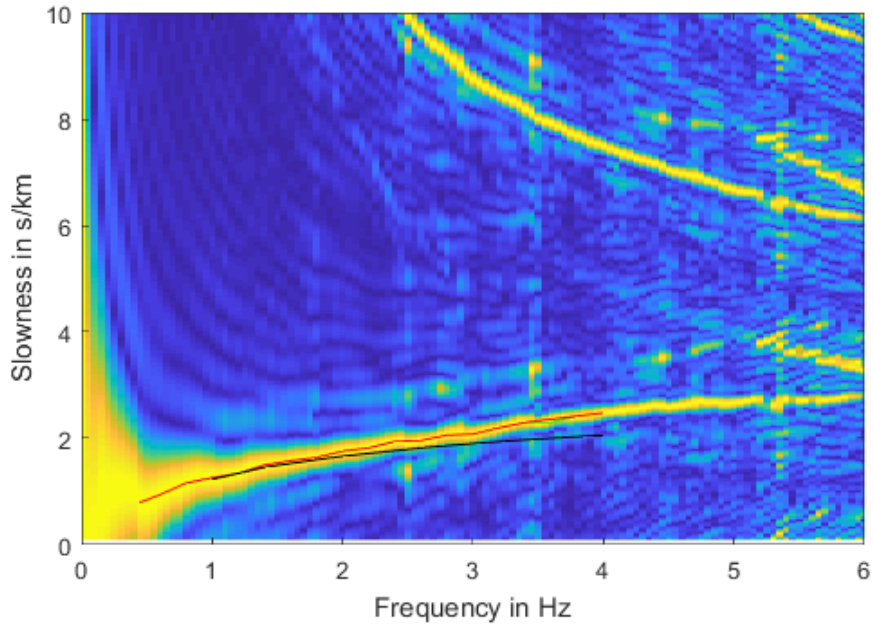

Figure 4.10: *Overtone radial component line one. The first overtone is plotted in black while the picked dispersion is plotted in red. They match well for lower frequencies, and deviate a little for higher.*

Figure 4.10 shows the dispersion image for the radial component line one with the theoretical overtone. The overtone is plotted in black. The curves match well for lower frequencies, but they deviate for higher frequencies, where the theoretical curve is lower.

Since the theoretical curve matches well with the dispersion curve from the data for the vertical, hydrophone and radial component, it suggests that this could be an overtone. Since there is only one coherent curve, it is easier to pick the dispersion from this component. Overtones are important because they can improve depth resolution of surface wave analysis. This is because overtones have higher frequencies for a given penetration depth, and therefore allow resolution of thinner layers. Combining the Love wave, Scholte wave and the overtone, with different sensitivities to the structure, will improve the resolution of depth inversion. (Maupin, 2016)

4.6 Discussion and concluding remarks on depth inversion

We get the shear wave velocity with depth from scratch by only using the dispersion curves we have retrieved from the noise correlations, which makes up our initial model. From the depth inversion we get profiles of shear wave velocity with depth that are almost the same as the initial model. This means that the a priori model is very good, and we can actually skip the last part of the inversion, which is the most time consuming part.

However, if we want to include the Love wave and the overtone to improve the model, the inversion is useful. In this way we get more constraints, and since the overtone has a higher frequency for a given depth than the fundamental mode, we can resolve thinner layers than with the fundamental mode only. If I had more time, I would have included the Love wave and the overtone in the inversion. Including depth interface layers in the velocity inversion might also improve the model.

The shear velocity model from ambient noise tomography was also compared to another model from the same area. This is displayed in Figure 4.11. Figure 4.11 shows the velocity model from ambient noise in red, and the other model from Equinor (Statoil) in blue. For the first 500 m, the models match very well. As we go deeper, the models deviate a lot, but meet again at 3000 m. The uncertainties of the model derived from ambient noise tomography increase with depth.

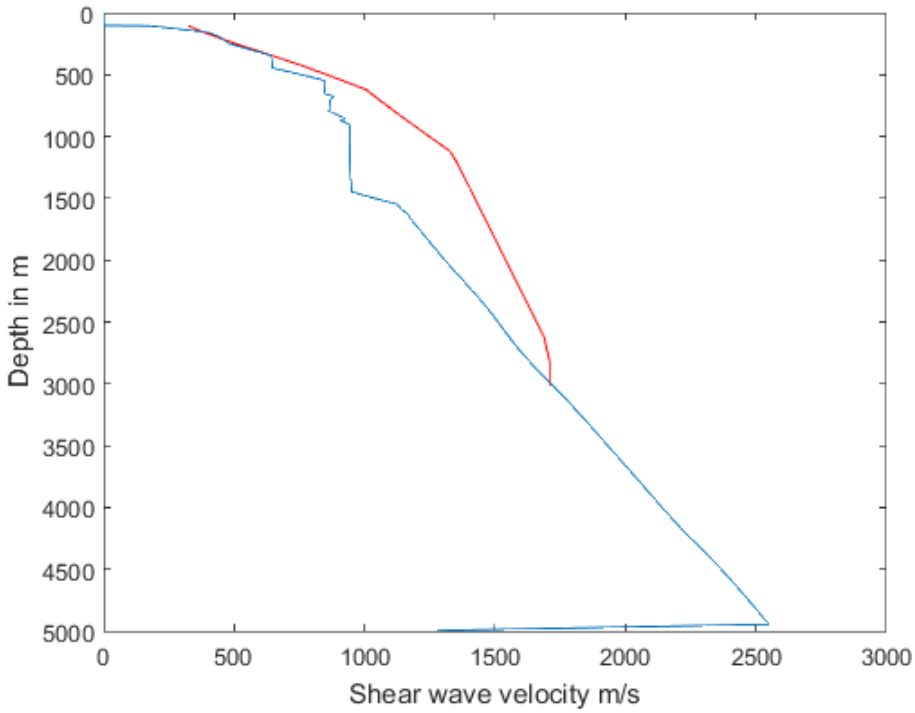

Figure 4.11: *Comparison of shear wave velocity models from Oseberg. The model from ambient noise is in red, while the one from Equinor (Statoil) is in blue.*

Since the receivers are already on the ocean bottom, and noise is free, ambient noise tomography is cost effective compared to other methods. The ambient noise tomography gave similar results to the previous model. It is therefore an option when monitoring the injection of waste. When monitoring, the procedure is repeated over time.

Chapter 5

Conclusion

The platform is a major source of noise in the area. Below 2 Hz, we have noise coming from all directions. Above 2 Hz, the main source is the platform. Both the energy coming from all directions and the noise from the platform can be used for interferometry. The ambient noise with frequencies up to 4 Hz was used for Green's function retrieval, and we see that eight hours of data is sufficient for retrieving the Green's functions. No major change with time was observed, and the Green's functions along the 4 lines are very similar. The Love wave and the Scholte wave fundamental mode and overtone emerged from the cross-correlations of ambient noise. The Scholte wave fundamental mode was used for inversion, and a model of S-wave velocity with depth down to 3000 m was obtained. The velocity increases from 300 m/s at the sea bottom to about1700 m/s at 3 km depth, similar to the results retrieved from other methods. The model can be enhanced by including the Love wave and the overtone in the inversion. The procedure could be used for monitoring by repeating it over time. Since noise is free, it is a cost effective option to monitor injection.

Appendices

Appendix A

Different correlation lengths

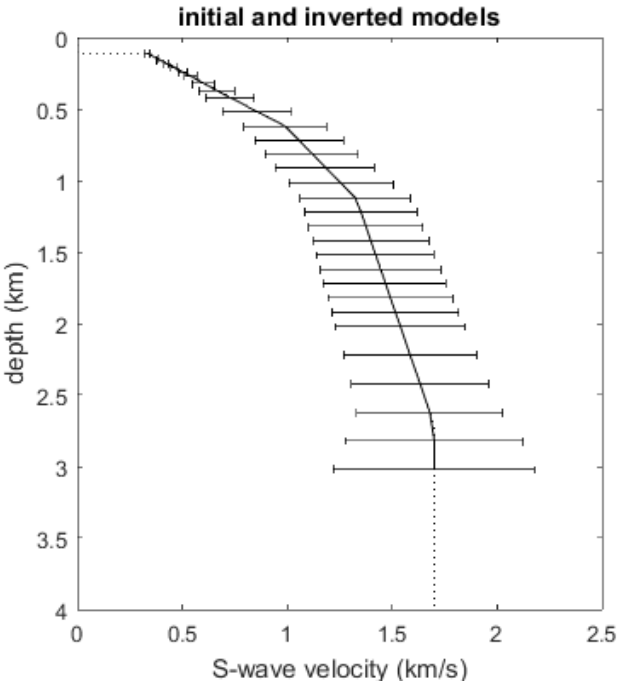

Figure A.1: *Same as Figure 4.5b but with linear coefficient equal to 0.1.*

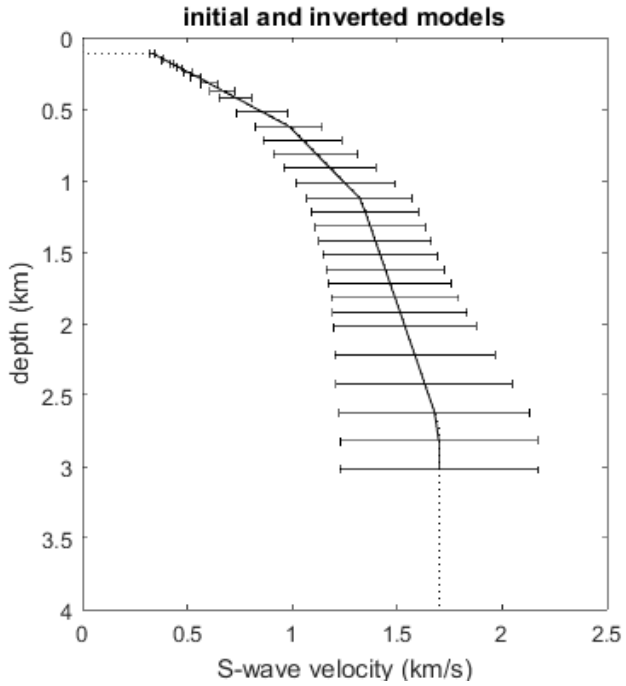

Figure A.2: *Same as Figure 4.5b but with linear coefficient equal to 0.6.*

Bibliography

Aki, K. (1957). Space and time spectra of stationary stochastic waves, with special reference to microtremors. *Bull. Earth. Res. Inst.*, 35:415–456.

Brenguier, F., Shapiro, N. M., Campillo, M., Nercessian, A., and Ferrazzini, V. (2007). 3-d surface wave tomography of the Piton de la Fournaise volcano using seismic noise correlations. *Geophysical research letters*, 34(2).

Brocher, T. M. (2005). Empirical relations between elastic wavespeeds and density in the earth's crust. *Bulletin of the seismological Society of America*, 95(6):2081–2092. Seismological Society of America.

Bussat, S., Bjerrum, L., Dando, B., Bergfjord, E., Iranpour, K., and Oye, V. (2016). Offshore injection and overburden surveillance using real-time passive seismic. *First Break*, 34(7):51–59.

Bussat, S. and Kugler, S. (2011). Offshore ambient-noise surface-wave tomography above 0.1 hz and its applications. *The Leading Edge*, 30(5):514–524.

Castagna, J. P., Batzle, M. L., and Eastwood, R. L. (1985). Relationships between compressional-wave and shear-wave velocities in clastic silicate rocks. *Geophysics*, 50(4):571–581. Society of Exploration Geophysicists.

Duvall Jr, T. L., Jeffferies, S., Harvey, J., and Pomerantz, M. (1993). Time–distance helioseismology. *Nature*, 362(6419):430. Nature Publishing Group.

EAGE Channel (2015). Eage e-lecture: Passive seismic surface-wave interferometry by sjoerd de ridder. `https://youtube.com/watch?v=4HA-HxmCDp4`. [accessed 14.11.2017].

Gouedard, P., Stehly, L., Brenguier, F., Campillo, M., Colin de Verdiere, Y., Larose, E., Margerin, L., Roux, P., Sánchez-Sesma, F. J., Shapiro, N., et al. (2008). Cross-correlation of random fields: Mathematical approach and applications. *Geophysical prospecting*, 56(3):375–393.

Lee, M. W. (1986). Spectral whitening in the frequency domain. Technical Report USGS Numbered Series, US Geological Survey.

Lévěque, J., Cara, M., and Rouland, D. (1991). Waveform inversion of surface wave data: test of a new tool for systematic investigation of upper mantle structures. *Geophysical Journal International*, 104(3):565–581.

Lin, F.-C., Ritzwoller, M. H., Townend, J., Bannister, S., and Savage, M. K. (2007). Ambient noise rayleigh wave tomography of new zealand. *Geophysical Journal International*, 170(2):649–666.

Lobkis, O. I. and Weaver, R. L. (2001). On the emergence of the green's function in the correlations of a diffuse field. *The Journal of the Acoustical Society of America*, 110(6):3011–3017. ASA.

Maupin, V. (2016). Surface wave inversion. *Encyclopedia of Earthquake Engineering*. Michael Beer, Edoardo Patelli, Ioannis Kougioumtzoglou and Ivan Siu-Kui Au (Eds.), Springer-Verlag, Berlin Heidelberg.

Maupin, V. and Cara, M. (1992). Love-rayleigh wave incompatibility and possible deep upper mantle anisotropy in the iberian peninsula. *Pure and applied geophysics*, 138(3):429–444. Birkhäuser Verlag, Basel.

McMechan, G. A. and Yedlin, M. J. (1981). Analysis of dispersive waves by wave field transformation. *Geophysics*, 46(6):869–874. Society of Exploration Geophysicists.

Mordret, A., Landès, M., Shapiro, N., Singh, S., Roux, P., and Barkved, O. (2013). Near-surface study at the valhall oil field from ambient noise surface wave tomography. *Geophysical Journal International*, 193(3):1627–1643.

Moschetti, M., Ritzwoller, M., and Shapiro, N. (2007). Surface wave tomography of the western united states from ambient seismic noise: Rayleigh wave group velocity maps. *Geochemistry, Geophysics, Geosystems*, 8(8).

Sadeghisorkhani, H. (2017). *Analyses and Application of Ambient Seismic Noise in Sweden: Source, Interferometry, Tomography*. PhD thesis, Acta Universitatis Upsaliensis, Uppsala, Sweden.

Saito, M. (1988). *DISPER80: A subroutine package for calculation of seismic normal-mode solution in Seismological Algorithm (ed. Doornbos, D. J.)*. Academic Press.

Schonewille, M. and Duijndam, A. (1997). Parabolic radon transform and x-squared fk-transform-aliasing and efficiency. Citeseer.

Shapiro, N. M. and Campillo, M. (2004). Emergence of broadband rayleigh waves from correlations of the ambient seismic noise. *Geophysical Research Letters*, 31(7).

Stehly, L., Fry, B., Campillo, M., Shapiro, N., Guilbert, J., Boschi, L., and Giardini, D. (2009). Tomography of the alpine region from observations of seismic ambient noise. *Geophysical Journal International*, 178(1):338–350.

Stein, S. and Wysession, M. (2003). *An introduction to seismology, earthquakes, and earth structure*. Blackwell Publishing.

Takeuchi, H. and Saito, M. (1972). Seismic surface waves. *Methods in computational physics*, 11 (ed. B. A Bolt):217–295. Academic Press.

Tarantola, A. and Valette, B. (1982). Generalized nonlinear inverse problems solved using the least squares criterion. *Reviews of Geophysics*, 20(2):219–232.